Micro- and nano-optical components for quantum technologies

By

Zhaoning April Yu

A dissertation submitted in partial fulfillment of

the requirements for the degree of

Doctor of Philosophy

(Physics)

at the

University of Wisconsin-Madison

2022

Date of final oral examination: 9/21/2022

The dissertation is approved by the following members of the Final Oral Committee:

Mikhail A. Kats, Associate Professor, Electrical and Computer Engineering

Mark Saffman, Professor, Physics

Zongfu Yu, Associated Professor, Electrical and Computer Engineering

Deniz Yavuz, Professor, Physics

© Copyright by Zhaoning April Yu 2022

All Rights Reserved

Abstract

The booming of quantum technologies offers exciting opportunities in the field of optics. This thesis includes our effort to address three optical challenges that our collaborators encountered when building a quantum repeater or a quantum chemical sensor, they are:

1. How to engineer diffraction gratings for trapping cold atom clusters? (Chapter 2)
2. How to efficiently generate optical bottle beams using a single surface-patterned chip? (Chapter 3)
3. How to extract fluorescence from color centers in diamond without damaging the diamond surface? (Chapter 4)

To interact with a small (atom-scale) quantum system, miniaturized optical components are often needed with micro- or nanometer structuring. Such compact structuring poses requirements in both simulation and fabrication methods:

a. When designing and evaluating a micro- or nano optical component, unlike conventional bulky optics where light can be approximated as rays, the electromagnetic field must be calculated with nm-scale spatial resolution.
b. When making a micro- or nano optical component, mechanical polishing could not reach sufficient accuracy, thus researchers resort to advanced lithography techniques (such as electron-beam lithography, laser lithography) which has already been used in the semiconductor industry.

The methods are introduced in Chapter 1, and discussed in details for each application scenario in Chapter 2-4. By using finite-difference time-domain (FDTD) simulation method and electron-beam lithography fabrication method, we demonstrate:

1. A grating chip for trapping dual atomic species with the balancing efficiency above 90%

for both species;

2. An optical metasurface design that generates a 32x32 bottle beam array using a single Gaussian beam luminance;
3. A silicon light extractor that enhances the fluorescence collection from shallow nitrogen-vacancy (NV) defects in diamond by 10 folds

Acknowledgment

Getting a PhD in physics is, frankly speaking, a quite challenging journey for me. Not only intellectually but more so mentally. And I would not have reached this point without the support from others.

Albeit I am the solo author of this thesis, it includes work and contribution from many. Especially the following personals:

- my advisor Prof. Mikhail Kats, who is always passionate about science, and who knows how to bring science into reality with practical approaches;
- my other committee members, Prof. Mark Saffman, Prof. Zongfu Yu, and Prof. Deniz Yavuz, who are excellent scientists and mentors;
- my honorary committee member, Prof. Jen Choy, who has helped with multiple projects;
- my lab mates: Dr. Yuzhe Xiao, Dr. Ray Wambold, Hongyan Mei, Jin Zhang, Dr. Chenghao Wan, Dr. Jad Salman, Dr. Zhenyang Xia, Dr. Gabriel Jaffe and Dr. Huilong Zhang, who has either contributed significantly to the research work in this thesis, or has given me generous help with the experiment;
- also my lab mates: Minjeong Kim, Sanket Deshpande, and Chengyu Fang, who will carry on the unfinished projects.

I would also like to thank some of my family members and friends, because of whom life becomes more joyful, even with challenging tasks:

- my parents, who have encouraged and supported my study abroad;
- my friends from college: Yueting Luo and Longjiao Zhao, who are always there to listen and to comfort;
- friends I met in the U.S.: Yihe Ma, Yeqi Shi, Zhuohan Li, Congying Wang, Allie Child,

Jimmy Perreault, and Cassie Kozak, with whom I had tons of fun;

- special thanks to my best friend in Madison: Biqing Wu, whom I feel lucky to have met;
- my two fluffy feline friends Eric and Alex, and my rest-in-peace thorny hedgehog friend Krav Maga, whom I could never get tired playing with.

Contents

Abstract....................i
Acknowledgment....................iii
Introduction....................1
Optics as an enabling field for quantum technologies....................1
Optical components based on multi-refractive-index metamaterials....................2
Engineering gratings for trapping cold atoms....................17
Quantum technologies with cold atoms....................18
Cooling and trapping atoms....................19
Simulating gratings for grating-MOTs....................25
Fabricating gratings for grating-MOTs....................32
Conclusion and future work....................48
Metasurfaces for efficient generation of optical bottle beams....................49
Atom trapping with optical bottle beams....................49
Designing bottle-beam metasurfaces....................56
Fabricating bottle-beam metasurfaces....................65
Summary and future work....................74
Adjoint-optimized structures for extracting fluorescence from color centers in diamond....................75
Quantum sensors based on color centers in diamond....................76
Designing silicon nano light extractors using adjoint optimization....................79
Fabricating silicon nano light extractors on diamond....................89
Appendices....................99
FDTD simulation results of checkboard gratings with gold coating....................99
Measured and simulated diffraction efficiencies for circular grating chips....................100
Derivation of the dipole force and the scattering force....................101
References....................105

Introduction

Optics as an enabling field for quantum technologies

Optics has been an enabling field for quantum technologies, including quantum computing [1], quantum communication [2], and quantum sensing [3]. Light is used not only to encode quantum information, but also to probe and modify the quantum states of individual quantum elements or groups of elements in physical systems such as atomic vapors [4] and solid-state materials [5]. To interact with micro- and nano-scale quantum information carriers, optical components are often times desired to be miniaturized [6] or produce complex wavefronts [7], [8]. The conventional approach of generating such light fields using densely placed cm-scale lenses, waveplates, and other bulk optical components results in large and complex experiments that are difficult to scale.

The concept of "flat optics" has taken off over the last 10 years [9], [10], based in significant part on the manipulation of light using closely packed nano-resonators. Such an approach brings several key advantages, including:

(1) Compactness with reduced size/weight. For example, mm-thick lenses and waveplates can be thinned down to <1 um patterned layers sitting on a substrate [11], [12];

(2) Integration: flat optics can be manufactured using scalable semiconductor processing techniques and can be made easy to integrate with other parts [13];

Inspired by flat optics, Chapters 2-4 of this thesis include our efforts of making compact (with micro- and nanoscale structuring) and integratable (silicon-based) optical components, where we aim to miniaturize optics used in quantum systems. In Chapters 2 and 3, we work with cold atoms. Chapter 2 describes our efforts to make diffraction grating chips for trapping two atomic species, which can potentially reduce system complexity by replacing six pairs of hand-aligned laser beams and mirrors with a self-aligned grating chip and two incident beams, one for each atomic species. Chapter 3 focuses on making a metasurface which transforms an incident Gaussian beam into an optical bottle beam, which can be used as a single-atom trap. In Chapter 4 we work with a different platform of point defects in diamond. We demonstrate nm thick light extractors sitting on top of a diamond substrate that can enhance the collected fluorescence from shallow nitrogen-vacancy centers underneath by up to 35 times.

Optical components based on multi-refractive-index metamaterials

Inspired by the approach of manipulating light on the subwavelength scale, as described in the introduction, we conducted a computational work showing that conventional optical components (such as lenses and prisms made with uniform materials) can be "superimposed" using a structure comprising waveguide arrays. We include this work below, which has been previously published as Z. (April) Yu et al, "Optical components based on multi-refractive-index metamaterials," *Journal of Physics D: Applied Physics*, vol. 53, no. 1, p. 015108, Oct. 2019 [14].

We studied optical components (lenses, prisms, Fabry-Perot-type etalons) comprising a metamaterial-like medium that cannot be described by a single set of refractive-index values, even

for fixed frequency, vacuum wavevector, and polarization. The metastructure that we explored is a periodic stack of dissimilar metal-clad waveguides with subwavelength width and spacing, which guide light at different phase velocities. From the ray-optics perspective, this multi-refractive-index "metamaterial" (MRIM) can be viewed as a spatial superposition of multiple homogeneous materials, each of which can be engineered independently. Using full-wave simulations, we demonstrate several optical components based on MRIMs, including triangular prisms that deflect light to multiple angles, lenses with multiple focal points, and multi-index Fabry-Perot etalons with an enhanced density of resonant modes. We also analytically derive the Fresnel-like reflection, transmission, and "swapping" coefficients at the interfaces between MRIMs and conventional materials, which enable the design of MRIM-based optical structures.

In conventional refractive optics, a complex refractive index can typically be assigned to the various constituent materials to describe light-matter interaction. The refractive index of materials is usually frequency dependent (dispersion), and sometimes polarization dependent (birefringence and dichroism). The study of metamaterials—artificial materials comprising subwavelength components—has resulted in the demonstration of many optical properties that are not found in nature [15]–[17]. Similar to conventional materials, a metamaterial is typically treated as homogeneous, with an effective refractive index (and impedance) following an effective medium theory [18]. In some cases, the effective parameters of metamaterials can also depend on the wave vector [19]–[22].

Here, we investigate optical components based on a structure that comprises an array of elements that are deeply subwavelength, but cannot be ascribed a single refractive-index value even for fixed frequency, vacuum wavevector, and polarization. By packing uncoupled subwavelength optical channels, the metamaterial can be made to have multiple simultaneous effective indices that can be engineered separately. Orlov et al. have previously explored such multi-branch dispersion [19], [23]. The extra degree of freedom of the refractive index (in addition to frequency dispersion, birefringence, and spatial dispersion) can be used to realize new types of refractive and interference optical components, such as prisms that deflect light to multiple angles, lenses with multiple focal points, and multi-index Fabry-Perot etalons with an enhanced density of resonant modes.

Consider light refracted by a prism with incident angle θ_i, as shown in Fig. 1.1. Snell's law relates the refracted angle (θ_t) of light in medium t with the incident angle (θ_i) in medium i: $n_i sin\theta_i = n_t sin\theta_t$, where n_i and n_t are the scalar refractive indices in i and t, respectively. Here, we consider a prism made from a hypothetical multi-refractive-index "metamaterial" (MRIM), such that n_i is replaced by a vector containing multiple scalar effective indices $(n_{eff,1}, n_{eff,2}, \ldots)$ resulting in multiple refracted angles $(\theta_{t,1}, \theta_{t,2}, \ldots)$. Note that here we put "metamaterial" in quotes because the structure cannot be homogenized despite comprising subwavelength components. For such a MRIM, the refraction to/from free space can be written as a slightly generalized form of Snell's law:

$$\begin{bmatrix} n_{eff,1} \\ n_{eff,2} \\ \ldots \end{bmatrix} sin\theta_i = n_t sin \begin{bmatrix} \theta_{t,1} \\ \theta_{t,2} \\ \ldots \end{bmatrix} \qquad \text{Eq. (1.1)}$$

For example, we assume a prism comprising a MRIM with period D and indices of $n_{eff,1} = 1.5$ and $n_{eff,2} = 2.5$ [Fig. 1.1(b)]. When p-polarized long-wavelength ($\lambda \gg D$) light of incident angle $\theta_i = 20°$ is refracted from the prism to free space, the wave is split into two, corresponding to two refracted angles given by Eq. 1.1 (*i.e.*, $\theta_{t,1} = 31°$ and $\theta_{t,2} = 59°$).

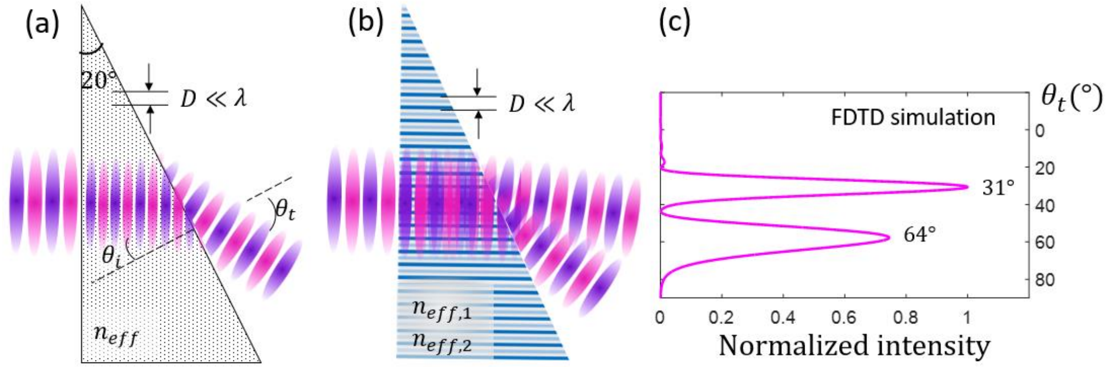

Fig 1.1. Linearly polarized monochromatic light with incident angle θ_i is refracted by a prism/air interface, where the prism comprises (a) a conventional material or metamaterial, resulting in a single refracted angle, θ_t, or (b) a multi-refractive-index metamaterial (MRIM) with period D, generating two distinct refracted beams, corresponding to two peaks in (c) the far-field angular distribution of the refracted light. (c) is simulated using the finite-difference time-domain (FDTD) method where the incident light is a transverse-magnetic (TM) Gaussian beam with free-space wavelength $\lambda_0 = 8\ \mu m$ and a beam waist of 30 μm, launched from just within the prism, and the prism comprises a subwavelength metal-insulator-metal (MIM) waveguide array with parameters described in the text.

To achieve multiple simultaneous refractive indices in a MRIM, light must propagate with multiple phase velocities. We accomplish this using a structure with multiple well-separated subwavelength propagation modes with different propagation constants. Figure 1.2(a) shows our MRIM comprising alternating subwavelength metal-insulator-metal (MIM) waveguides [24], [25] with different mode indices and thus different phase velocities. In each subwavelength waveguide, only one waveguide mode is allowed to propagate, with a single effective index n_{eff}. Because of the

simultaneous presence of multiple subwavelength channels with differing phase velocities, the resulting periodic structure must be described by multiple effective indices at the same time ($n_{eff,1}, n_{eff,2}, ...$), even for incident light with a given frequency, vacuum wavevector, polarization along an axis of symmetry. Each index of our MRIM can be tuned independently by designing the corresponding subwavelength MIM waveguide.

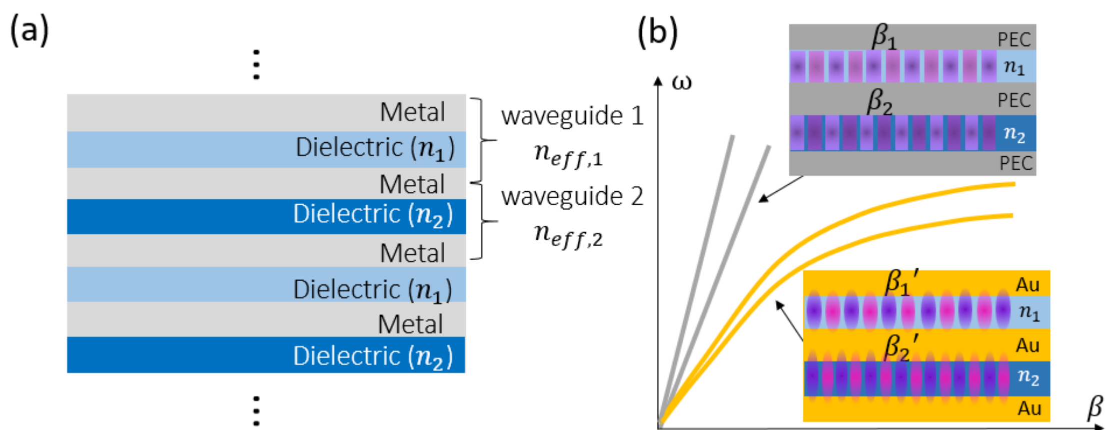

Fig 1.2. (a): A periodic metamaterial comprising multiple deep-subwavelength waveguides with different mode indices, resulting in multiple simultaneous values of effective index (here, two values). The metal-insulator-metal (MIM) waveguides comprise two metal layers and one dielectric layer in between, with refractive index n_1 or n_2. (b): Sketch of the double-branch dispersion curve (with angular frequency ω and propagation constant β) of such a MRIM, with the metal being a perfect electric conductor (PEC) or gold (Au). For PEC walls, the allowed mode in each MIM waveguide is the transverse electromagnetic (TEM) mode, whereas for gold walls, this mode is the antisymmetric surface-plasmon polariton (SPP) mode.

To demonstrate the multiple refraction shown schematically in Fig. 1.1(b), we consider a MRIM prism comprising two types of subwavelength MIM waveguides, with 100-nm walls made from a perfect electric conductor (PEC) and two types of dielectric layers: the first with $n_1 = 1.5$ and a thickness of 100 nm, and the second with $n_2 = 2.5$ and a thickness of 150 nm. The TEM mode of an MIM waveguide with PEC walls has no cutoff frequency and a linear dispersion curve [Fig.

1.2(b)], where the mode index is equal to the refractive index of the dielectric layer ($n_{eff,1} = n_1 = 1.5$, $n_{eff,2} = n_2 = 2.5$). The combination of thickness and index of the dielectric was chosen such that light tended to be coupled equally into the different channels, as described below. We initially selected lossless PEC for the walls so that we could investigate MRIM behavior without attenuation. However, since there is no loss, additional care is needed in any simulation to prevent reflected light from bouncing in the prism and forming secondary refracted beams, complicating the analysis.

We performed finite-difference time-domain (FDTD) simulations (note: we describe the principles of FDTD and practical considerations for such simulations in Chapter 2), launching a transverse-magnetic Gaussian beam using a source just inside of the prism, with an absorbing boundary cutting through one side of the prism (on the left side of the prism in Fig. 1.1(b)) to suppress the aforementioned back reflections. The resulting simulations showed that the far-field distribution of the refracted light has peaks at $\theta'_{t,1} = 31°$ and $\theta'_{t,2} = 64°$ [Fig. 1.1(c)], compared to $31°$ and $59°$ from the ray-optics-like calculation in Eq. 1.1. We understand this discrepancy to be due to diffraction, since the size of the simulated prism is relatively small ($< 10\lambda_0$). The 8% shift in $\theta_{t,2}$ drops to $< 4\%$ if the size of the prism is doubled, reducing the effects of diffraction (the simulated far-field distribution for both sizes is shown in the supplementary material of [14]).

Because the dispersion diagram of the MRIM contains several curves, we can view the MRIM as a spatial superposition of several distinct refractive media, each with a single dispersion curve. In particular, the MRIM in Fig. 1.2 can be regarded as the superposition of two hyperbolic metamaterials [15]. As a demonstration of this superposition effect, we simulated a cylindrical lens comprising a MRIM with $n_{eff,1} = 2.1$ and $n_{eff,2} = 4.5$ [Fig. 1.3(a, b)], and observed the focusing of light to two focal points. The field distribution of light focused by this lens is almost

identical to the coherent sum of the fields of two conventional cylindrical lenses of the same size and shape, comprising uniform dielectrics with these two refractive indices [Fig. 1.3(c)].

The MRIM lens in Fig. 1.3(a, b) was designed with gold walls, using the optical properties for gold from ref. [26]. As a result, the mode indices of the MIM waveguides and hence the effective indices of the MRIM are larger than the indices of the dielectric layers themselves ($n_{eff,1} > n_1 = 1.5$, $n_{eff,2} > n_2 = 4$) [25]. Gold was selected to more-closely mimic experimentally realizable conditions, and also because we found that truncated PEC waveguides resulted in strong Fabry-Perot-like resonances [described in more detail in Fig. 1.5(c)], negatively affecting focusing performance. The combination of index and thickness of the dielectric layers was chosen so that the two foci of the MRIM lens are separable and of comparable field magnitude (design-procedure details in the supplementary material of [14]).

The focal lengths of a MRIM lens can be approximately predicted using the Lensmaker's formula [27], generalized for multi-index materials:

$$\begin{bmatrix} f_1^{cal} \\ f_2^{cal} \\ \cdots \end{bmatrix} = \frac{R}{\begin{bmatrix} n_{eff,1} \\ n_{eff,2} \\ \cdots \end{bmatrix} - 1} \qquad \text{Eq. (1.2)}$$

where R is the radius of curvature. We note that for small lenses (with Fresnel number $N < 10$), like the one in our simulation (Fig. 1.3), the actual focal length will be smaller than the prediction of Eq. 1.2 due to diffraction effects [28]. After correcting for diffraction, we obtained calculated focal lengths of 24 µm and 67 µm (see supplementary of [14]), compared to the simulated focal lengths of $f_1 = 27$ µm and $f_2 = 59$ µm [Fig. 1.3(a)]. The main difference between theory and simulation is that each theoretical focal length is calculated separately, while in the simulation the

MRIM lens generates one overlapping field; this shifts the two foci closer to each other when the fields are added coherently. After summing the fields of focused light from two conventional dielectric lenses with the same size, shape, and refractive indices as the MRIM lens in Fig. 1.3(a), the focal lengths of the "superimposed lens" are found to be $f_1' = 29$ μm and $f_2' = 60$ μm [Fig. 1.3(c)], which gives a better prediction of the foci of the MRIM lens.

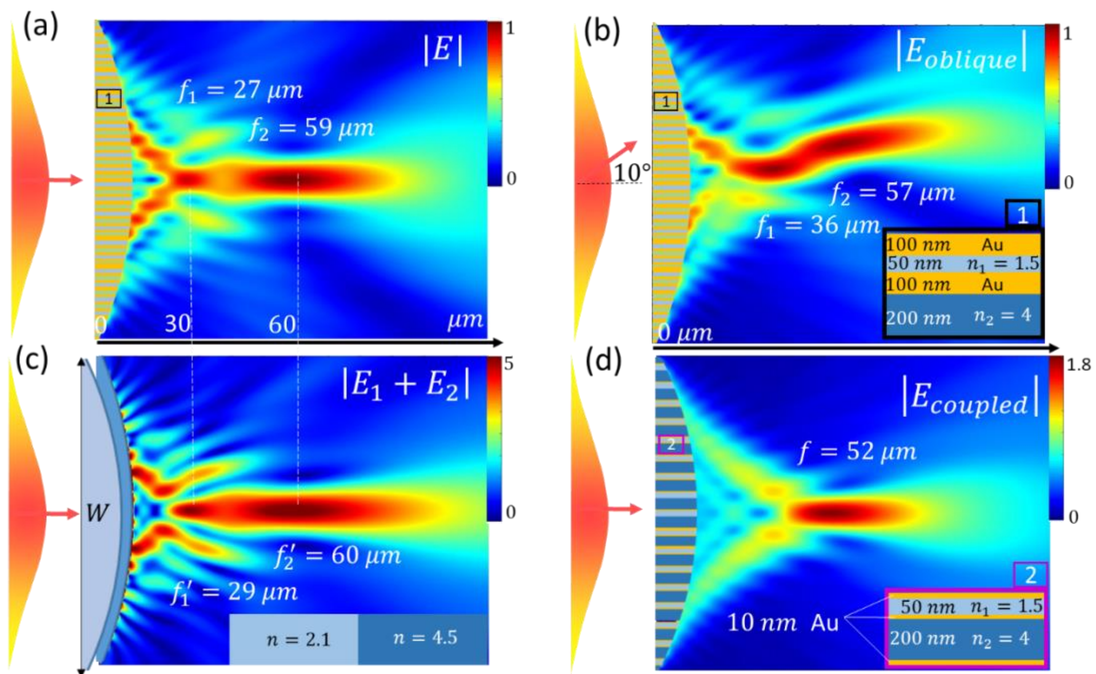

Fig 1.3. FDTD simulations of light focused by cylindrical lenses. (a) & (b): Two foci are generated by our lens comprising a MRIM with optically thick gold walls, shown in the inset of (b), for (a) normal and (b) oblique incidence at an angle of 10° from free space. (c): A field distribution similar to that in (a) is found by coherently adding the fields from two lenses of the same size and shape as in (a, b), comprising two different homogeneous transparent dielectrics with refractive indices corresponding to the two effective indices of the MRIM. (d): After reducing the gold-layer thickness, only one focus can be observed. All lenses are of the same plano-convex shape, with radius of curvature $R = 85\ \mu m$, width $W = 80\ \mu m$, and minimum thickness $t_e = 1\ \mu m$ at the edge. The incident light is a p-polarized Gaussian beam at $\lambda_0 = 8\ \mu m$, with beam waist $w_0 = 35\ \mu m$. The refractive index of gold is taken to be $n_{Au} = 8.5 + 46.4i$ [26].

To test the MRIM lens for imaging purposes, we also simulated the MRIM lens with light incident at an angle of 10° [Fig. 1.3(b)], where two off-axis foci are generated at $f_1 = 36$ μm and $f_2 = 57$ μm, compared to the coherently summed fields of the two superimposed dielectric lenses which result in $f_1' = 39$ μm and $f_2' = 63$ μm (the latter shown in the supplementary material of [14]). The 10% difference between the focal length of the MRIM lens and that of the "superimposed lens" may be a result of the different transmission of the two channels in the MRIM, which do not correspond to the relative transmission of the two dielectric lenses.

To analyze the efficiency of MRIM-based optical components, such as the lens in Fig. 1.3, we need to calculate the transmission coefficient at the interface between free space and a MRIM, where standard Fresnel equations do not apply due to the presence of multiple effective indices and the nontrivial wave impedance of the MRIM. Thus, we derived modified Fresnel equations at interfaces involving a MRIM by considering the boundary conditions and conservation of power. When light (with original electric field E_0) is incident from free space onto a MRIM, it can be reflected (with field E_r) or enter the optical channels of the MRIM (with E_j representing the field inside the jth channel), as drawn in Fig. 1.4(a). For s-polarized light, E_j is equal to the electric field in the metal walls at the dielectric-metal boundary inside the MRIM, and thus is negligible, meaning s-polarized light can barely enter the MRIM (*i.e.*, the reflectance $R_s \approx 1$). For p-polarized light, the magnetic field H is continuous from free space to each optical channel. For simplicity, here we only consider a MRIM comprising PEC walls, where the magnetic field is uniform across each waveguide (*i.e.*, only the TEM mode can propagate) and linearly related to the product of the electric field and the refractive index of the dielectric ($H_j = E_j n_j / Z_0$, Z_0 is free-space wave impedance). The magnetic field in free space, which includes the incident field and the reflected

field (with a π phase shift), is also linearly related to the product of the electric field and the refractive index ($n_{free\ space} = 1$) by the same factor, *i.e.*, $H_0 - H_r = (E_0 - E_r)/Z_0$. Subsequently, the continuity of the magnetic field ($H_0 - H_r = H_1 = H_2 = \cdots = H_j$) can be written as:

$$E_0 - E_r = E_1 n_1 = \cdots = E_j n_j = \cdots \qquad \text{Eq. (1.3)}$$

Note that for a MRIM using real metals, Eq. 1.3 must be generalized for non-uniform mode profiles. In addition to Eq. 1.3, power must be conserved at the interface, such that the incident power is equal to the sum of the reflected power plus the transmitted power into all of the channels ($P_{inc} = P_r + \sum_j P_j$). Replacing the magnetic field (H) with the electric field ($H \propto En$), we can write the power flow as $P = EH(\text{Area}) \propto nE^2(dcos\theta)$. Therefore, we obtain:

$$cos\theta_i D E_0^2 = cos\theta_i D E_r^2 + \sum_j n_j d_j E_j^2 \qquad \text{Eq. (1.4)}$$

where θ_i is the angle of incidence in free space and d_j the width of the jth type of waveguide [Fig. 1.4(a)]. Combining Eqs. 1.3 and 1.4, we obtain the Fresnel-like transmission and reflection coefficients for p-polarized light incident from free space (denoted in subscript as "f") onto a PEC-based MRIM:

$$t_{fj} \triangleq \frac{E_j}{E_0} = \frac{2cos\theta_i D/n_j}{cos\theta_i D + \sum_k d_k/n_k}$$

$$r_{ff} \triangleq \frac{E_r}{E_0} = -\frac{cos\theta_i D - \sum_k d_k/n_k}{cos\theta_i D + \sum_k d_k/n_k} \qquad \text{Eq. (1.5)}$$

where t_{fj} is the field transmission coefficient into the jth channel. We have verified Eq. 1.5 by FDTD simulations with different angles of incidence θ_i [Fig. 1.4(c)], thicknesses (d_j), and indices (n_j) of optical channels (see Fig. S3 of the supplementary material in ref. [14]).

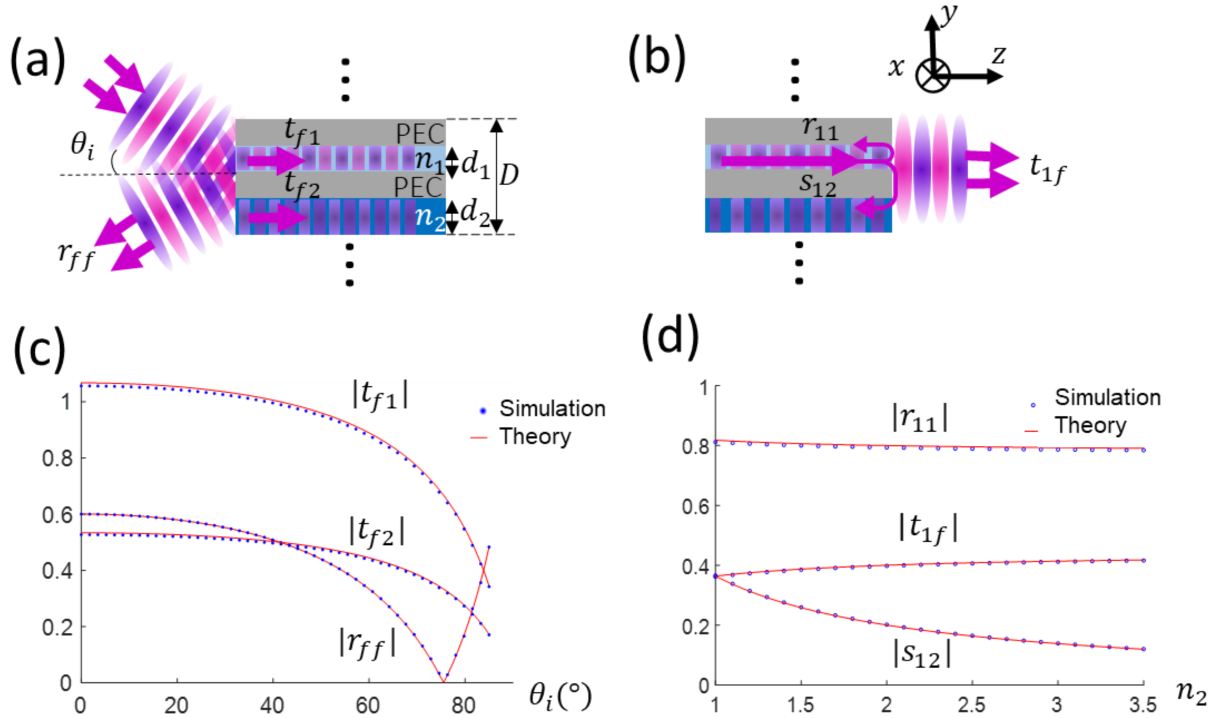

Fig. 1.4 Light behavior at the interface between free space and a MRIM. (a): light from free space with incident angle θ_i is reflected and transmitted at an interface with a MRIM. (b): TEM-mode light in one optical channel of a two-channel MRIM is reflected to the same channel, swapped over the other channel, and/or transmitted to free space. (c): Reflection and transmission coefficients (r_{ff} and t_{f1}, t_{f2}) of (a) as a function of θ_i. (d): Reflection, swapping, and transmission coefficients (r_{11}, s_{12}, and t_{1f}) of (b) as a function of the index of the second dielectric (n_2) of the MRIM. All MRIMs have the same period $D = 400\ nm$, with equal thickness of the layers ($d_1 = d_2 = d_{PEC} = 100\ nm$). The index of the first dielectric (n_1) is 1.5. In (c, d), theoretical results are shown as red lines, and were calculated using Eq. 1.5 and 1.8, respectively; simulation results are shown as blue symbols, and were obtained using FDTD method with periodic boundary conditions along the y axis and a source with free-space wavelength $\lambda_0 = 8\ \mu m$.

Though Eq. 1.5 is only directly applicable for PEC walls, we can still use it to estimate the reflectance at the left boundary of the MRIM lens with gold walls in Fig. 1.3(a): approximately

~40%. Due to the propagation losses (absorption in the gold), only ~5% of the total incident power is ultimately transmitted and focused. One feasible way to increase the overall efficiency is to decrease the thickness of the gold walls so that the MRIM has impedance closer to that of free space, which lowers the reflection. However, the gold walls cannot be too thin, otherwise the modes will couple and a single effective index can then be assigned to the metamaterial [29]. This is shown in Fig. 1.3(d), where the gold layer thickness is reduced significantly to 10 nm; the structure can then be assigned a single effective index $n_{eff} = 2.3$, and only one focus is observed, which lies in between the two foci from Fig. 1.3(a). We also note that there are many possible routes to decreasing the absorption losses in such a structure (e.g., ref. [30]), though we do not explore them here.

We also calculated the transmission and reflection coefficients for the inverse situation, when light is incident from within a MRIM onto an interface with free space. This problem is more complex than the case of incidence from free space, because in addition to reflection or transmission, "swapping" can occur, *i.e.*, light can jump from one optical channel (j) to another ($l \neq j$), as shown in Fig. 1.4(b). This can be seen from the continuity of magnetic fields at the interface between the MRIM and free space. Similar to Eq. 1.3, we replace the magnetic field with the product of the refractive index and the electric field:

$$E_0 n_j = E_t = E_1 n_1 \ldots = E_l n_l = \cdots \qquad \text{Eq. (1.6)}$$

The TEM mode in channel j is transmitted to free space (with electric field E_t), which also induces a nonzero electric field at the lth channel ($E_l = E_t / n_l \neq 0$). As a result, part of the incident power is swapped:

$$d_j n_j E_0^2 = d_j n_j E_r^2 + D E_t^2 + \sum_{l \neq j} n_l d_l E_l^2 \qquad \text{Eq. (1.7)}$$

Combining Eqs. 1.6 and 1.7, we obtain the Fresnel-like transmission, reflection, and swapping coefficients for light propagating from the jth optical channel of a MRIM to free space or into the lth optical channel:

$$t_{jf} \triangleq \frac{E_t}{E_0} = \frac{2d_j}{\sum_k d_k/n_{eff,k} + D}$$

$$r_{jj} \triangleq \frac{E_r}{E_0} = \frac{\sum_{k \neq j} d_k/n_{eff,k} + D - d_j/n_{eff,j}}{\sum_k d_k/n_{eff,k} + D} \qquad \text{Eq. (1.8)}$$

$$s_{jl} \triangleq \frac{E_l}{E_0} = \frac{-2d_j/n_{eff,l}}{\sum_k d_k/n_{eff,k} + D}$$

A comparison between Eq. 1.8 and full-wave simulations can be found in Fig. 1.4(d) as well as in the supplementary material Fig. S4 of [14].

Using Eq. 1.8, we analyzed a Fabry-Perot-like etalon comprising a lossless MRIM with two types of optical channels [Fig. 1.5(a, b)]. Taking the results from Eqs. 1.5 and 1.8, we can calculate the total transmission coefficient through the two-channel etalon (derivation in the supplementary material of [14]):

$$\frac{E_t}{E_0} = \begin{bmatrix} t_{f1} e^{i\phi_1} & t_{f2} e^{i\phi_2} \end{bmatrix} \begin{bmatrix} 1 - C_{11} & -C_{12} \\ -C_{21} & 1 - C_{22} \end{bmatrix}^{-1} \begin{bmatrix} t_{1f} \\ t_{2f} \end{bmatrix}$$

$$C_{jk} = \sum_{l=1,2} a_{jl} a_{lk} e^{i(\phi_l + \phi_k)} \qquad \text{Eq. (1.9)}$$

where a_{mn} represents all transmission/reflection/swapping coefficients, and $\phi_j = (2\pi L/\lambda_0)n_{eff,j}$ is the phase accumulated during one-way propagation through a MRIM slab with length L in the jth channel. For the special case where the two optical channels are identical, Eq. 1.9 is equivalent to the well-known transmission of a conventional Fabry-Perot etalon: $E_t/E_0 = (t_{fx}\, t_{xf}\, e^{i\phi_x})/(1 - r_{xx}^2\, e^{2i\phi_x})$, where t_{xf}, t_{fx} and r_{xx} are the standard Fresnel transmission and reflection coefficients at the interface between free space and material x. The generalization of Eq. 1.9 for more than two channels can be found in the supplementary information of [14].

Using Eq. 1.9, in Fig. 1.5(c) we plot the transmittance of our two-channel MRIM Fabry-Perot etalon as a function of the cavity length L. Compared to a transparent dielectric etalon with the refractive index matching one of the effective indices of the MRIM, the MRIM etalon yields an enhanced density of resonant modes, which are located close to the transmission resonances of the dielectric etalons [Fig. 1.5(c) vs. two blue curves in Fig. 1.5(e)]. At the same time, due to the coupling of the two propagation modes via swapping, the MRIM etalon cannot be treated as a "superimposed etalon" by summing the fields of two dielectric etalons; this can be seen from the difference in their transmittance [Fig. 1.5(c) vs. red curve in Fig. 1.5(e)]. Note that we did not discuss the effect of swapping on the performance of the MRIM lens made with gold layers in Fig 1.3(c), since approximately 90% of the swapped light is absorbed by the metal after a complete round trip in the MIM waveguides (see Supplementary 7 in ref. [14] for a brief calculation).

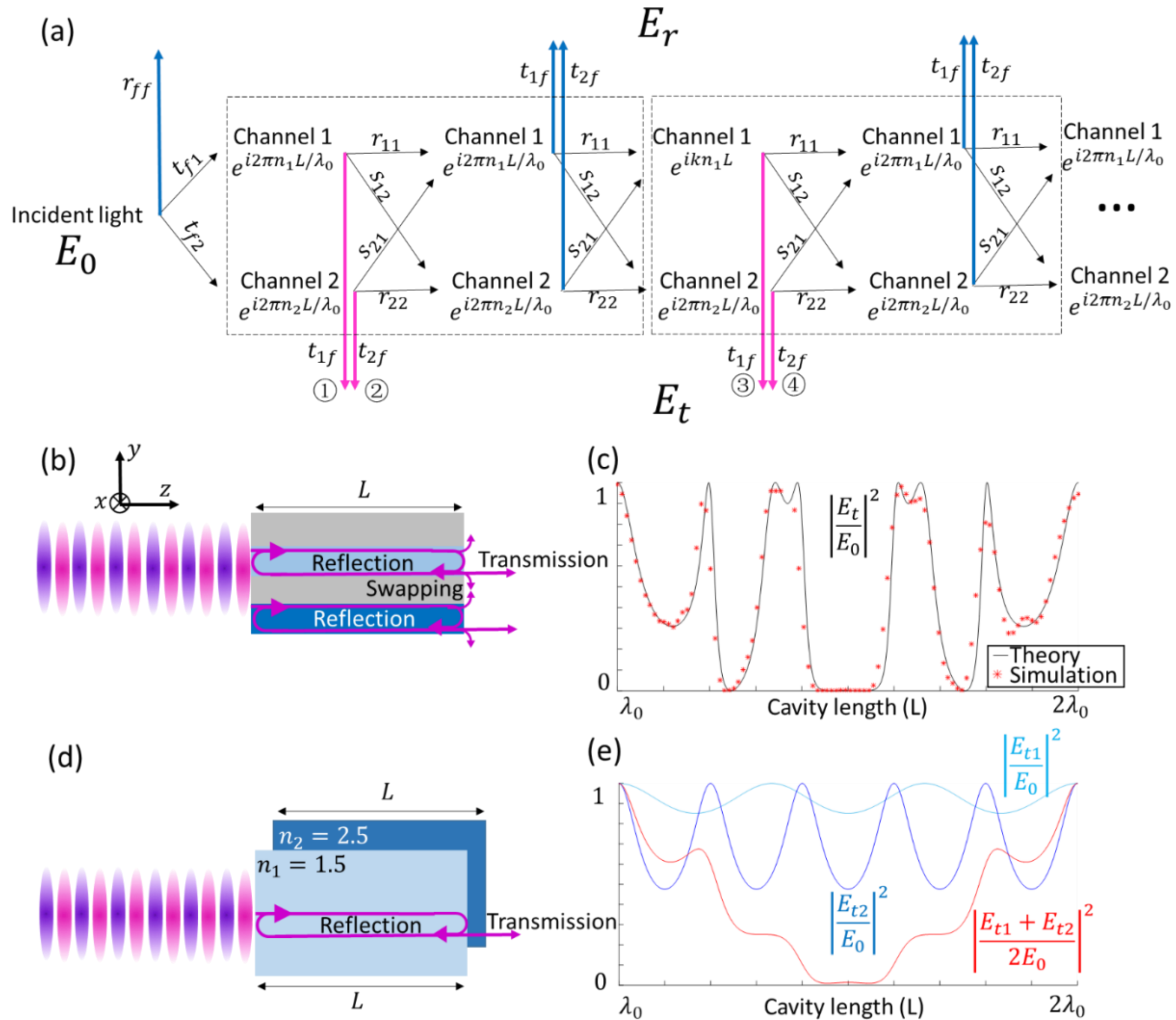

Fig 1.5. Light from free space incident on a Fabry-Perot etalon with cavity length L. (a) Schematic of the optical paths when the Fabry-Perot etalon has two optical channels with effective indices $n_{eff,1}$, $n_{eff,2}$. Fields contributing to the total reflection are represented as going up in the schematic, while those contributing to the total transmission as going down. Each dashed box groups two sequential optical channels and represents a round-trip in the etalon. (b, c): Light normally incident on a Fabry-Perot-like etalon comprising a MRIM that has period of $D = 450\ nm$, composed of two dielectrics of index $n_1 = 1.5$ with $100\ nm$ thickness, $n_2 = 2.5$ with $150\ nm$ thickness, and PEC with $100\ nm$ thickness. The light is p-polarized (with electric field E_0 along the y axis) and has free-space wavelength $\lambda_0 = 8\ \mu m$. (c) Transmittance of (b), where theoretical results (black curve) were calculated using Eq. 1.9, and simulation results (red symbols) were obtained using FDTD simulations with periodic boundary conditions along the y axis. (d, e): Light incident on two different Fabry-Perot etalons made with homogeneous transparent dielectrics with refractive indices corresponding to the two effective indices of the MRIM in (b). (e) Transmittance of the two etalons in (c), and the coherently averaged transmission (red line).

In conclusion, we studied optical components (lenses, prisms, Fabry-Perot etalons) comprising a metamaterial-like medium that has an extra degree of freedom in the refractive index, in addition to frequency dispersion, birefringence, and spatial dispersion. Refractive components made of this kind of multi-refractive-index "metamaterial" (MRIM) can behave similarly to multiple superimposed conventional refractive components of the same geometry. We simulated several common optical components, substituting a MRIM based on subwavelength waveguide arrays for conventional transparent dielectrics, including a triangular prism, a cylindrical lens, and a Fabry-Perot etalon. Given a linearly polarized incident beam, the prism yields multiple distinct refracted beams, the lens multiple focal points, and the Fabry-Perot etalon an enhanced density of resonant modes. Our result can be generalized to metamaterials comprising a variety of deep-subwavelength waveguides with either one- or two-dimensional confinement, as long as the modes have no cutoff frequency (e.g., coaxial waveguides [31][32]). The ability to design optical components out of materials with multiple simultaneous refractive index values may enable new functionalities, such as synchronous imaging of multiple focal planes.

Engineering gratings for trapping cold atoms

This project is a collaboration between two research groups within UW-Madison: Prof. Mark Saffman's group in the Physics Department and Prof. Mikhail Kats's group in Electrical & Computer Engineering Department. The Saffman group contributed to atomic physics experiments,

including the building of magneto-optical traps, measuring fluorescence from atoms, etc. The Kats group contributed to designing, fabricating, and optically characterizing the grating chips. The work has been previously published in forms of conference talks and posters including: [33]–[37].

Quantum technologies with cold atoms

Cold atoms are used in a number of quantum applications. For example, the current world's most accurate clock is built using strontium atoms (an alkaline earth metal), which measures time to a precision equivalent to losing < 1 milliseconds in the entire lifespan of the universe, and can detect the gravitational redshift within 1 millimeter (Fig. 2.1, [38]). Moreover, the world's first Bose-Einstein condensates were produced in a vapor of evaporatively cooled rubidium-87 atoms in 1995 [39], since then cold atoms have become a vital platform to study quantum many-body physics [40]. Cold atoms are also used for quantum computing [41]–[43], quantum simulation [44], [45], sensing [46], as quantum communication nodes [47], and for observing quantum phenomena such as the quantum random walk [48].

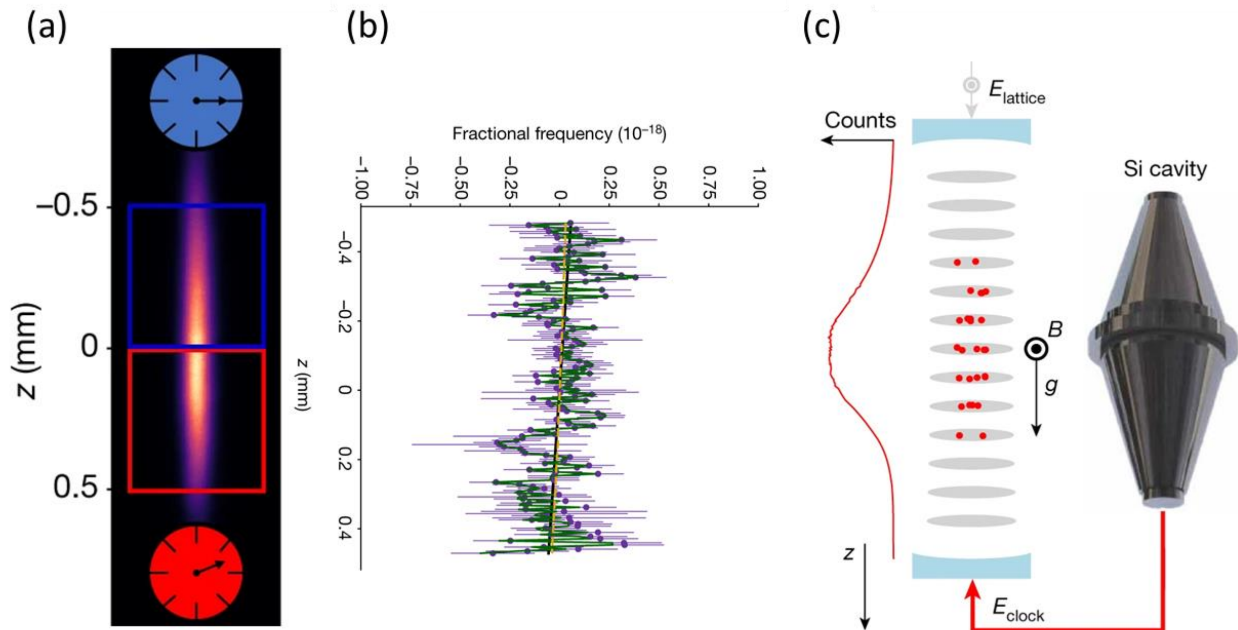

Figure 2.1 Using cold ($800\ nK$) ^{87}Sr atoms to measure time and detect the gravitational redshift within a mm scale. (a) The ^{87}Sr atomic cloud is confined in a vertical cavity [the cavity wall shown in light blue in (c)]. The gravitational redshift leads to the higher clock (blue box) ticking faster than the lower one (red box). (b) The frequency map as a function of height (z), with raw frequencies shown in green, and the linear fit shown in black. Higher atoms have higher resonant frequency than lower atoms due to slightly smaller gravitational acceleration g and less redshift. (c) 1D optical lattice for trapping atoms. The longitudinal axis of the cavity, z, is oriented along gravity. E_{clock}: a laser locked to the ultra-stable oscillation of a single-crystalline silicon cavity. Source: (a) Fig. 4(a), (b) Fig. 3(a), (c) Fig. 1(a) of ref [38].

Cooling and trapping atoms

Atoms can be cooled using laser light, as illustrated in Fig. 2.2 for the 1D case. If a laser beam that illuminates atoms is tuned near the resonant frequency of the atoms, the atoms can absorb photons propagating along the direction of the laser beam and then re-emit them isotropically. This absorption and re-emission process results in net momentum transfer (a momentum “kick”) to the atoms, and the force is referred to as the scattering force. In 1D, a standard cooling configuration consists of illuminating atoms with two counter-propagating beams that are both red-detuned from

the atomic resonance (Fig. 2.2). In this configuration, atoms moving to the left experience a Doppler shift with respect to both beams, "seeing" light from the left that is closer to resonance and light from the right that is more off resonance. As a result, atoms moving to the left absorb and re-emit more light from the left, and atoms moving to the right absorb and re-emit more light from the right, and therefore slow down (cool).

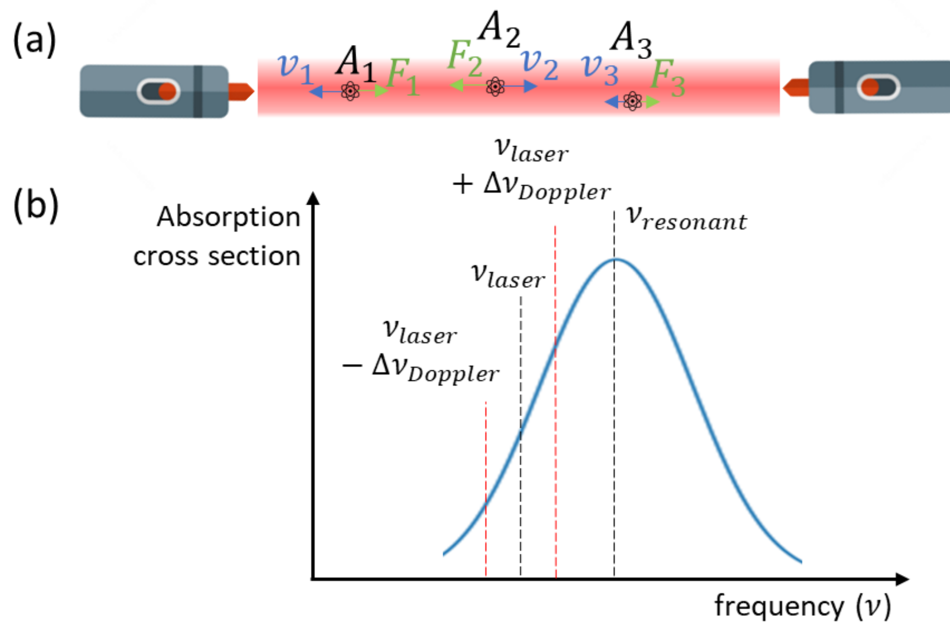

Figure 2.2 Laser cooling in 1D illustrated with a (a) schematic and (b) cartoon absorption spectrum (b). A pair of counterpropagating lasers (one can be replaced by a mirror) are red detuned with frequency ν_{laser} lower than the resonant frequency $\nu_{resonant}$ of atoms (A_i). Due to Doppler effect, an atom A_1 moving to the left observes a higher frequency from the left laser $\nu_{left} = \nu_{laser} + \Delta\nu_{Doppler}$, and a lower frequency from the right laser $\nu_{right} = \nu_{laser} - \Delta\nu_{Doppler}$. Since ν_{left} is closer to the resonance peak, A_1 absorbs more photons from the left laser and are pushed to the right. Based on a similar logic, atom A_2 moving to the right are pushing to the left. Since F_i always points to the opposite direction with v_i, all atoms, regardless of their velocity, are slowed down. v_i, F_i: the velocity and the scattering force of the atom A_i.

Besides cooling, atoms also need to be confined or "trapped" inside a vacuum chamber from diffusion and collision with air molecules. Atoms can be trapped with a similar setup as cooling

using counterpropagating red-detuned lasers, but in this common scheme the laser beams are circularly polarized and a particular gradient magnetic is applied. This apparatus is called a magneto-optical trap (MOT) was first invented at Bell Labs 35 years ago [49] and is now a mainstay of atomic physics labs worldwide, such as the one shown in Fig. 2.3(b) from ref [50].

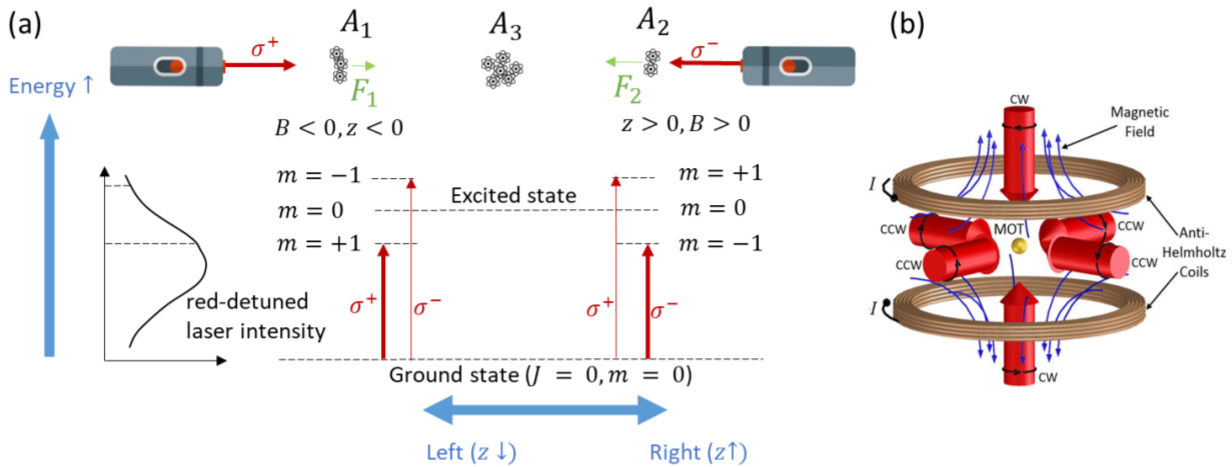

Figure 2.3 Magneto-optical traps (MOTs) (a) Cartoon illustrating a 1D MOT with two counterpropagating laser beams, and a gradient magnetic field (B). (b) A 3D MOT with six laser beams (or 3 counterpropagating pairs, shown as red arrows) and two anti-Helmholtz coils (shown as gold rings) for generating a quadrupolar magnetic field. Source: (b) [50]

A 1D MOT is illustrated in Fig. 2.3(a). A gradient magnetic field (B) is positive at $z > 0$, negative at $z < 0$, and zero at $z = 0$. Two red-detuned counterpropagating beams have opposite handedness (circular polarization): with the beam from left being σ^+ and the beam from right being σ^-. With the presence of the magnetic field, the atomic energy level will shift based on the total electronic angular momentum (m) (Zeeman effect). For the atom cluster A_1 at $z < 0$, the transition to $m = +1$ will shift closer to the laser frequency, and the transition to $m = -1$ will shift further away. As a result, the atoms in the ground state ($m = 0$) will absorb more σ^+ photons which will excite atoms to the $m = +1$ state (conservation of angular momentum). And the σ^+

light from the left will push A_1 to the right. Based on similar logic, the atom cluster A_2 at $z > 0$ will absorb more σ^- light and get pushed to the left. Therefore, regardless of their original position, all atoms are pushed to $z = 0$, where they experience an equal amount of scattering of σ^+ and σ^- light.

A 3D MOT is illustrated in Fig. 2.3(b), with six laser beams (or 3 counterpropagating pairs, shown as red arrows) and two anti-Helmholtz coils (shown as gold rings) for generating a quadrupolar magnetic field. Although the schematics are straightforward, building a MOT in practice can be time consuming to align, collimate, and adjust polarization for six beams. The bulky lenses, waveplates, and mirrors for preparing these six beams can result in a large physical footprint, which limits portability and scaling of atom-based devices [Fig. 2.4(a)].

There has been a continuous effort in simplifying MOTs, including the approach of replacing some laser beams with multiple mirrors oriented as an inverse pyramid [51]–[54]. In the last decade, several works have shown that a MOT can be simplified by using only one incident beam and a diffraction-grating chip [55]–[60], two of which are shown in Fig. 2.4 (c-f). The atoms in these grating MOTs (or GMOTs) are trapped by radiation pressure from the incident beam and multiple diffracted beams. Among the demonstrated GMOTs, some used a chip that stitches multiple linear (1D) gratings together [55]–[58], [60]. Take the 1D-grating chip in Fig. 2.4 (c-d), for example, the incident beam is balanced by three first-order diffraction beams from three linear gratings.

These 1D-grating chips have a center that need to be aligned with the $B = 0$ point of the gradient magnetic field. On the other hand, the 2D-grating chips, such as the one in Fig. 2.4 (f) from [56]

and in [57] are centerless, thus does not need to be aligned in the horizonal plane (normal to the incident beam). These self-aligned 2D-grating chips can potentially be further integrated into a cm-scale chamber as shown in Fig. 2.4 (e).

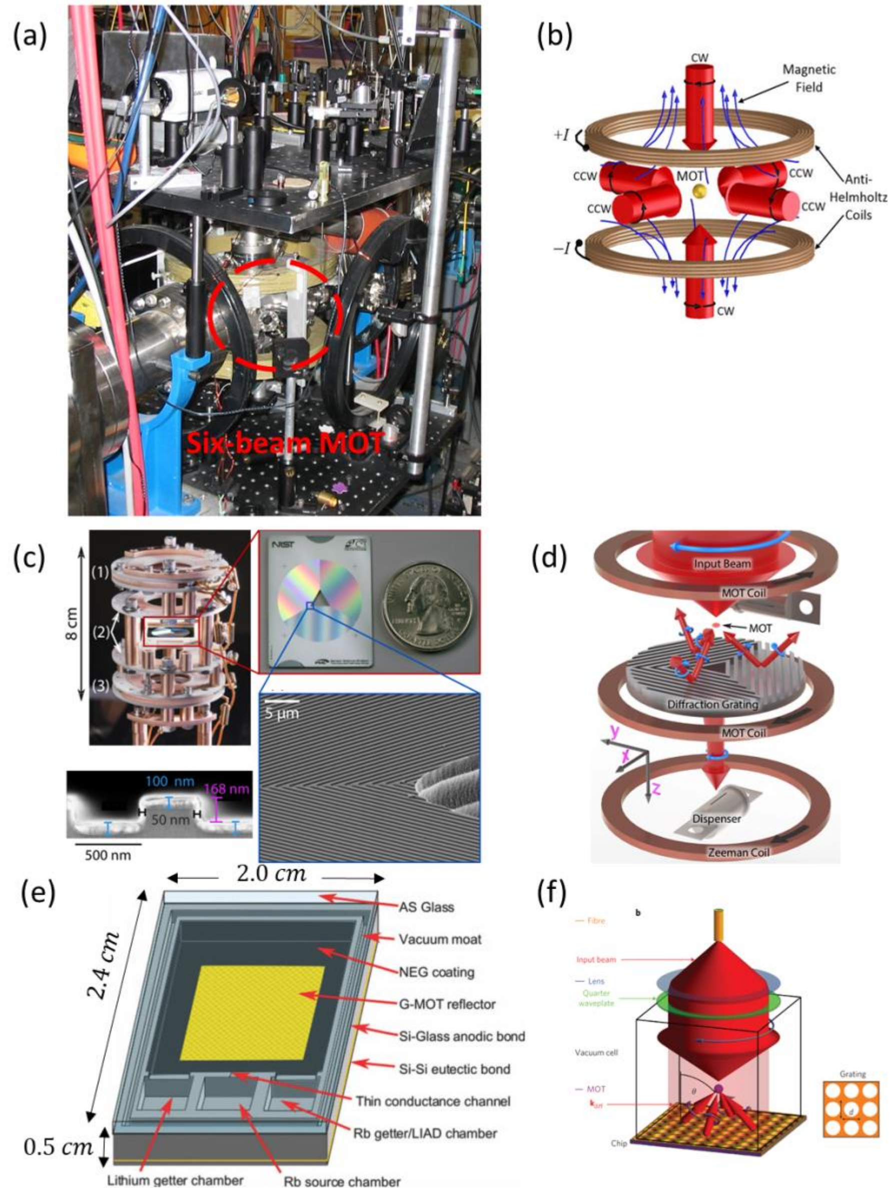

Figure 2.4 A six-beam MOT (a-b) and grating MOTs with a 1D-grating chip (c-d) or a 2D-grating chip (e-f). (a) A picture of a six-beam MOT. The atoms are trapped inside the red circle surrounded by optics and coils. (b) Schematics of the six-beam MOT, same picture as Fig. 2.3(b). (c-f) MOTs with a diffraction grating chip. Instead of using six independent beams, atoms are trapped by radiation pressure from one incident beam and multiple diffracted beams. (c-d) show a 1D-linear-

grating chip which has a center (a triangular hole) that needs to be aligned with the magnetic field zero. Three diffraction beams counterbalance the incident beam. (e-f) shows a centerless 2D-grating chip that is translational invariant. (e) proposes a miniaturized GMOT on the cm scale. (a) is from the Macdonald lab at Kansas State University; (b) is from reference [50] ; (c-d) are from reference [59]; (e) is adapted from reference [6] ; (f) is from reference [56].

So far, most GMOTs operate at a single wavelength ($780\ nm$ for trapping ^{87}Rb [55]–[57], or $671\ nm$ for trapping ^{7}Li [59]), and a recent work has demonstrating a MOT at two wavelengths subsequently for cooling ^{88}Sr in two steps [60]. We are interested in simultaneously trapping more than one atomic species, which is complex to implement with multiple sets of six beams, but may be achieved with a GMOT using more than one incident beam and a shared diffraction-grating chip which operates at multiple wavelengths [Fig. 2.5 (a-b)]. The simultaneous trapping of multiple atomic species has been used for sympathetic cooling [61], generating superfluids [62] and Fermi-Bose degenerate gases [63], [64], and testing the equivalence principle [65], [66]. It may also be used for quantum nondemolition state measurement [Fig. 2.5(c)] [67].

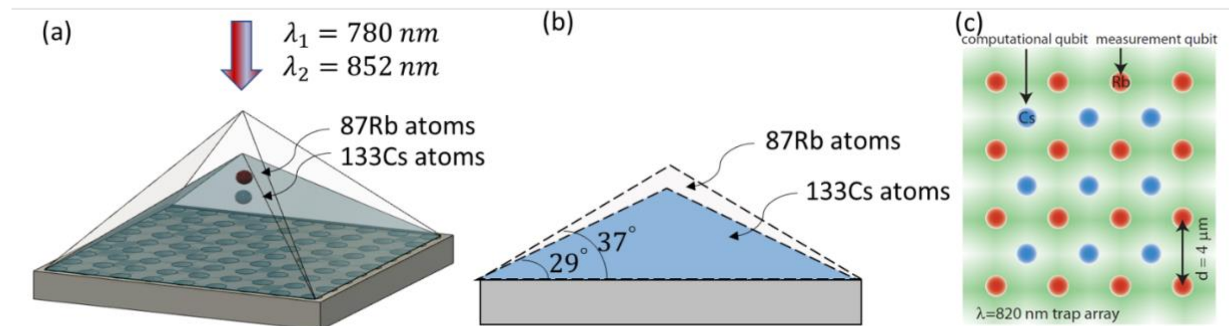

Figure 2.5 (a-b) A 2D grating chip for trapping dual atomic species. Two laser beams (with wavelength 780 nm and 852 nm) are diffracted to different angles, forming two pyramid trapping regions with different heights. The higher trapping pyramid of 780 nm beam is the Rb trapping region, the lower one of 852 nm beam is the Cs trapping region. (c) The proposed multiquibit quantum register in [67].

In this Chapter, we designed 2D-grating chips operating at two wavelengths ($780\ nm$ for trapping ^{87}Rb atoms and $852\ nm$ for trapping ^{133}Cs atoms, with the energy level diagram of two atomic species shown in Fig. 2.6). We performed full-wave simulations on different grating designs and showed that an optimized design can simultaneously have high force-balancing efficiency for trapping both atomic species. We fabricated mm-scale grating chips using electron-beam lithography and performed optical characterization. The atom-trapping experiment is ongoing.

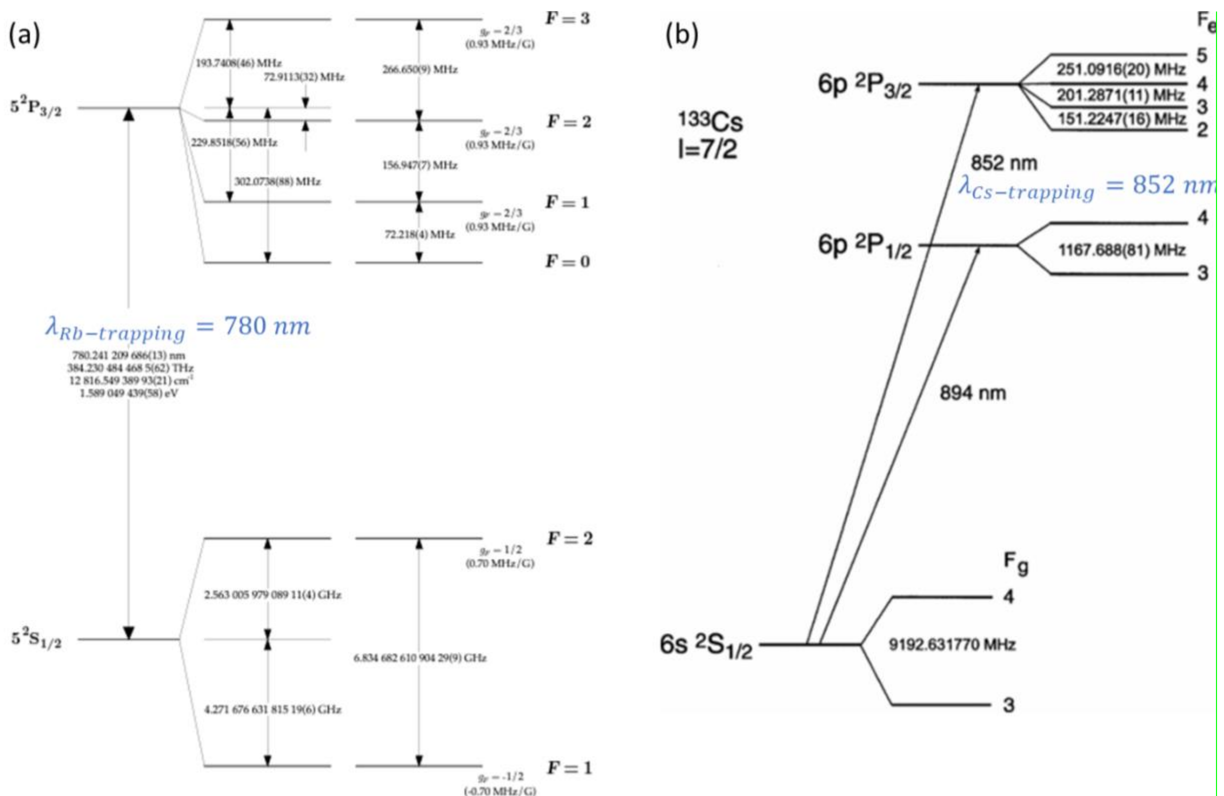

Figure 2.6(a) ^{87}Rb D2 transition hyperfine structure [68], with the trapping wavelength for ^{87}Rb at 780 nm noted in blue. (b) ^{133}Cs energy level diagram [69], with the trapping wavelength for ^{133}Cs at 852 nm noted in blue.

Simulating gratings for grating-MOTs

In a standard 6-beam MOT, it is straightforward to understand the necessary power balance and polarization of the 6 beams: the beams should be equal in power and circularly polarized as shown in Fig. 2.4(b). This becomes more complicated in a grating MOT, where the beams are no longer all along three axes, and furthermore the diffracted beams are unlikely to be circularly polarized even for circularly polarized incident light.

Previously, work has been done to analyze and characterize the balancing condition of one-dimensional (1D) gratings using scalar diffraction theory [56], [57]. However, this method can be imprecise; for example, it cannot account for Rayleigh-Wood anomalies and surface-plasmon polaritons (SPP) [70], and thus may not correctly identify the designs that result in maximum trapping efficiencies. Furthermore, precise design guidelines are not yet available for 2D grating chips.

In this section, we use full-wave simulations based on the finite-difference time-domain (FDTD) methods to simulate the light diffracted from the grating chips. The FDTD method is a numerical method that solves Maxwell equations chronically (i.e., in the time domain). It uses finite differences to approximate the electromagnetic field derivatives over time or over a space coordinate, and discretizes the continuous 3D space into a cuboid mesh [Fig. 2.7 (a)]. In this thesis, we used the commercial FDTD package provided by Ansys Lumerical.

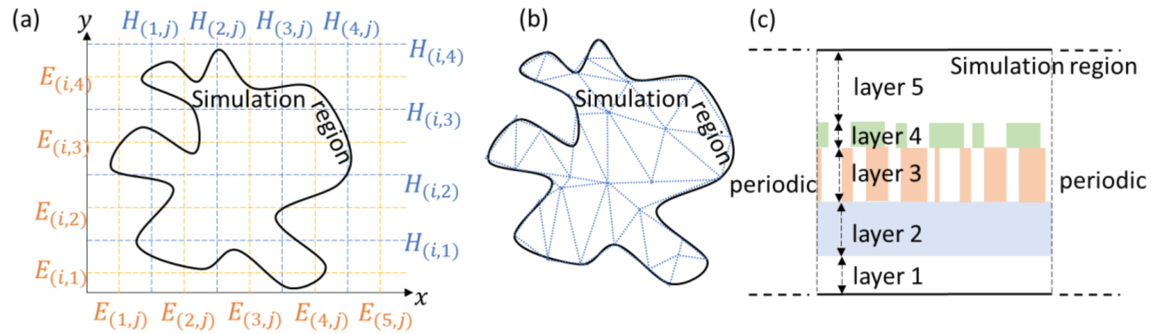

Figure 2.7 Common 2D Meshing of different simulation techniques including: FDTD (a), FEM (b), and RCWA (c).

Besides FDTD, grating structures can also be analyzed used the finite-element method (FEM) or rigorous coupled-mode analysis (RCWA). As illustrated in Fig. 2.7(b), FEM calculates approximate value of physical properties (such as electric field, magnetic field strength) on what is typically an irregular spatial lattice. It was first used for analyzing structure mechanics but now has been adopted by optics community with commercial software available (e.g., COMSOL). RCWA is a semi-analytical method for simulating periodic structures. It solves Maxwell equations in Fourier (wave vector) space. First the incident field is decomposed into plane waves with different wave vectors. Then the simulation region is sliced into layers so that each layer is invariant along the propagation direction [Fig. 2.7(c)]. After calculating propagation modes (field profile over x, y) for each layer, light is decomposed into propagation modes and passed from layer to layer by matching boundary conditions at the interface, until the last layer (the semi-infinite transmission field in the final optical media). RCWA does not work well for aperiodic structures or curved structures where a sloped edge needs to be divided into many segments and is memory expensive.

We will address the polarization of the diffraction order later, but initially we wanted to explore

the trapping performance of a grating chip using a power metric proposed in [57], called the balancing efficiency (η_B), which calculates the balance between the radiation force from the incident beam and the diffraction beams [Fig. 2.8 (a, c)]:

$$\eta_B = \frac{\sum \eta_1}{1-\eta_0}, \qquad \text{Eq. (2.1)}$$

where $\eta_{0,1}$ is the diffraction efficiency of the 0th/1st order. Since the radiation pressure $p \propto$ intensity $I \propto$ (Power P / beam width w). For a 1st order diffraction beam, the vertical projection of the radiation pressure is $p_1 \cos\theta \propto (P_1/w_1)\cos\theta = (\eta_1 P_{inc}/w \cos\theta) \cdot \cos\theta = \eta_1 \cdot \; P_{inc}/w$. Therefore, $\eta_B = \sum \frac{\eta_1}{1-\eta_0} = \frac{\sum P_1}{P_{inc}-P_0}$. A unity balancy efficiency ($\eta_B = 1$) means radiation power is perfectly balanced ($\sum P_{0,1} = P_{inc}$). η_B is ideally 100%, which is automatically satisfied for a lossless symmetric grating with $\eta_0 + \sum \eta_1 = 1$. For a practical grating that has some loss due to scattering, absorption, or excitation of higher diffraction orders, $\eta_0 + \sum \eta_1 = 1 - loss$, and thus Eq. (2.1) becomes:

$$\eta_B = 1 - \frac{loss}{1-\eta_0} < 100\% \qquad \text{Eq. (2.2)}$$

A 2D grating with $loss > 0$ will have a $\eta_B < 1$, causing atoms to be pushed downwards. Larger loss and a stronger 0th order diffraction lead to a smaller η_B and a grating that is further away from the ideal balancing condition.

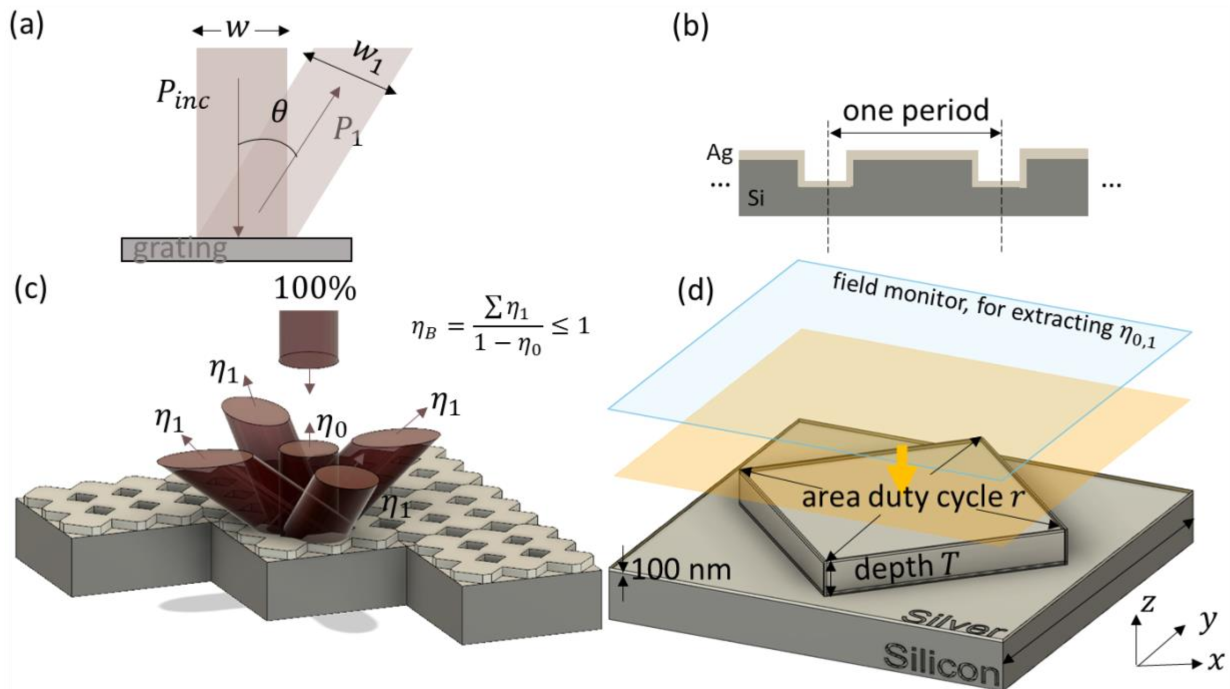

Figure 2.8 (a, c) the balancing efficiency (η_B) evaluates the radiation force balance between the incident beam and diffraction beams. A 2D grating with loss will have $\eta_B < 1$, causing atoms to be pushed downwards. (b) Cartoon illustrating the cross section of the grating structure. (d) Schematic of our FDTD simulation of the checkboard grating. One grating period is simulated with periodic boundary conditions in both x, y (z uses absorbing boundary conditions). The normal incident beam is a plane wave with a wavelength range $780 \sim 852\ nm$. The fields are recorded on a field monitor in the near field (blue box), which are then used to calculate the diffraction power and polarization using a far-field transform.

We then decided on the physical structure of the gratings. We picked silicon as the supporting structure as it is easy to pattern with common lithography techniques. We then picked silver as the coating because it has high reflectivity at both trapping wavelengths. Although gold is as reflective and has been used in the literature, we noticed that gold can react with alkali atoms which we want to trap [71], and our initial plan was to put the grating inside the cell with the atoms. The cross section of the grating structure is illustrated in Fig. 2.8(b).

Because we want to trap two atomic species with the same grating, the grating period p has to lie in the range such that there are no diffraction orders beyond the 1st order for both trapping wavelengths:

$$852\, nm < p < 780 \cdot \sqrt{2} = 1103\, nm \qquad \text{Eq. (2.3)}$$

By increasing the period, the diffracted beams become less oblique, so the trapping volume in Fig. 2.5(a) becomes larger, but the trap will be weaker in the horizontal direction: as illustrated in Fig. 2.8(a), the horizontal projection of the radiation pressure is $p_1 \sin\theta \propto (P_1/w_1)\sin\theta = (\eta_1 P_{inc}/w\cos\theta)\cdot\sin\theta = \eta_1 \cdot\ P_{inc}/w \cdot \tan\ \theta$. A smaller diffraction angle θ leads to less radiation pressure in the horizontal direction. Therefore, we selected the midpoint of the range with $p = 978\, nm$.

In principle, the exact geometry of the grating unit cell does not matter too much and, indeed, similar results have been obtained for GMOTs with a checkerboard grating and a grating with circular pillars [56]. For our work, we started with a checkboard pattern.

The FDTD simulation is setup as illustrated in Fig 2.9 (d): we simulated one period of the grating chip and used periodic boundary conditions in both x and y. The grating is illuminated with a broadband plane wave (yellow square), spanning both of our wavelengths of interest. A field monitor (blue square) is placed on top of the light source to capture the near-field profile right next to the grating. From the near-field profile, we calculated the far-field diffraction efficiency of the 0th and 1st diffraction orders ($\eta_{0,1}$), as well as their polarization states, using a far-field transform.

The far-field transform decomposes the near field into a set of plane waves propagating at different angles, then we calculates the fraction of power propagates in each grating order direction [72].

We performed a parameter sweep over the patterning depth (T) and the area duty cycle of the square post (r). The balancing efficiency (η_B) for each grating design is calculated using Eq. 2.2 and plotted in Fig. 2.9 (a-b). Our calculations show that a 2D grating chip can simultaneously have $\eta_B > 90\%$ for both wavelengths [780 nm and 852 nm, structure indicated as the red star in Fig. 2.9(a, b)]. The diffractive chip has a patterned silicon substrate [pitch (d) of 978 nm, area duty cycle of higher squares (r) of 55%, and patterning depth (T) of 230 nm], and silver coating with thickness of $100\ nm$. We note that for some geometries we observed a surface-plasmon polariton (SPP) resonances in some gratings [e.g., black crosses in Fig. 2.9(b, c)] that can hamper the balancing due to an increase in light absorption. Similar phenomena have been observed for gratings with gold coating, and we found it can be prevented using a thicker metal coating (Appendix). Furthermore, to test the robustness of our design, we studied a variety of 1D grating chips with gold coatings, where the duty cycle was varied from unit cell to unit cell, simulating fabrication defects. We found that an 8% random variation from a 50% duty cycle (r) can result in approximately 5-15% of the incident light to be lost to scattering and absorption.

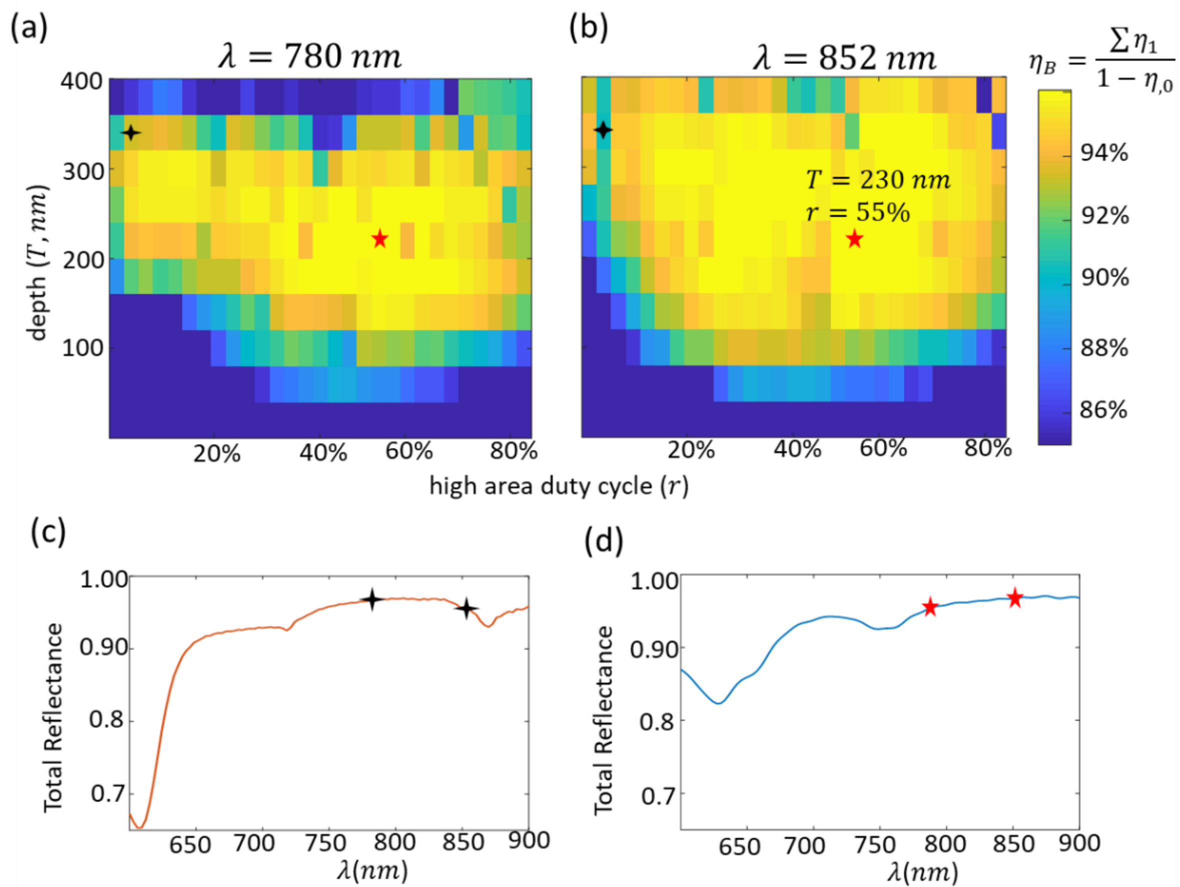

Figure 2.9 (a-b) Simulated balancing efficiency (η_B) for different checkboard gratings at 780 nm (a) and 852 nm (b). At the design indicated by the black cross, η_B drops drastically at 852 nm comparing to neighboring pixels which have similar designs. We plotted the broadband reflection spectrum with the black-cross grating in (c), and found a reflection dip near 870 nm indicating a plasmon resonance happening there [70]. We picked an optimal design (indicated by the red star, with $T = 230\ nm$ and $r = 55\%$) which is robust to fabrication errors in both T and r. The grating with the red-star design has $\eta_B \approx 95\%$ for both trapping wavelengths, and a reflection spectrum shown in (d).

Fabricating gratings for grating-MOTs

We used conventional lithography techniques to fabricate our grating chips, with the basic process flow shown in Fig. 2.10. Depending on the resolution of the target pattern, either photolithography or electron-beam lithography can be used. Photolithography has a lower resolution but a much higher throughput than e-beam lithography. The resolution of a photolithography machine is limited by the diffraction of its UV source, the numerical aperture of the optical system, and the thickness & contrast of the photoresist. Since the smallest feature of our grating chip (~0.5 μm) lies at the boundary of photolithography (using UV light, such as the i line, and conventional instruments found in academic cleanrooms) and e-beam lithography, we tried both.

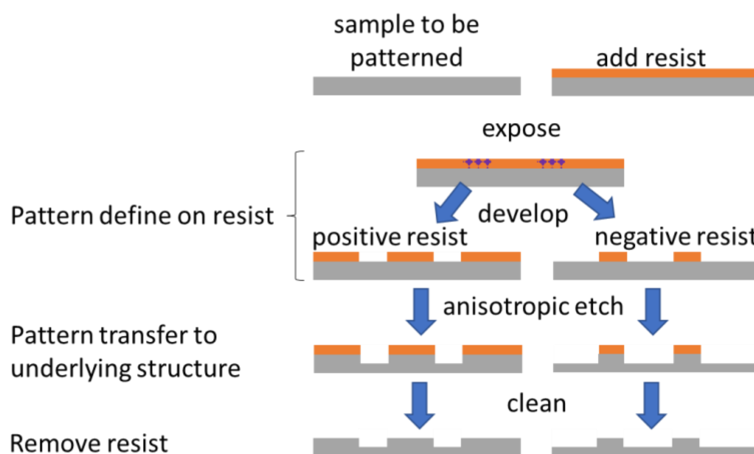

Figure 2.10: The lithography process flow. An UV/e- sensitive resist is first spin coated on top of the sample. Then the pattern is defined on the resist by exposing to a UV light or electron beam. Depending on whether the tone of the resist is positive (or negative), the exposed (or unexposed) region will be later removed by reacting with developer chemicals. The pattern is transferred from the resist mask to the underneath sample through anisotropic etching. Finally, the resist mask can be stripped off with solvent such as acetone or 1165 remover.

We first tried photolithography. Roughly speaking, there are three types of photolithography tools: contact aligners, steppers, and maskless laser scanners (Fig. 2.11). At the time when we fabricated

the checkboard gratings, both contact aligners and a stepper were available Wisconsin Centers for Nanoscale Technology (WCNT), a maskless laser scanner has been added recently.

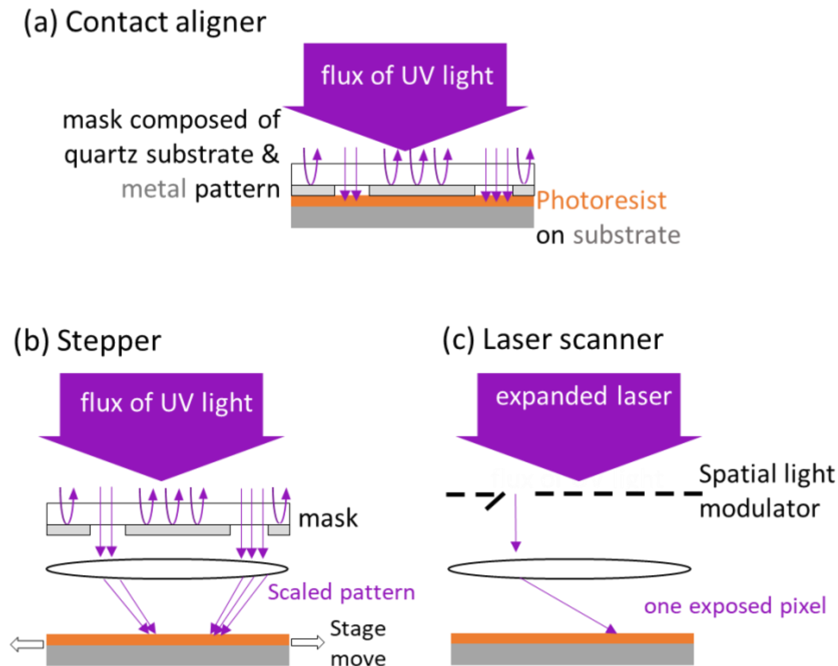

Figure 2.11: The schematic of different types of photolithography machines including (a) a contact aligner, (b) a stepper, and (c) a maskless laser direct writer (scanner).

Contact aligners shine a flux of UV light through a mask that is in direct contact with the resist. The desired pattern (or its complementary pattern) is first made on the mask using a UV-reflecting metal (e.g., Cr) on a UV-transparent substrate (e.g., quartz). When the mask is illuminated by the UV, only the region without metal can transmit UV to expose the resist. Depending on whether the resist is positive (or negative), the exposed (or un-exposed) part will be washed off later in a developing chemical. Thus, the pattern is transferred from the mask to the photoresist. Since the mask is in direct contact with the resist, the pattern is transferred with the same size (1:1). The

aligner exposes one entire pattern simultaneously within one shot of UV flux (which usually lasts for a couple seconds). It can also expose many patterns at once if they are integrated into one mask. To our experience, contact aligners (Suss MA6 and MJB3 with UV wavelength $\lambda = 0.3{\sim}0.5\ \mu m$) at the WCNT have a resolution down to $1{\sim}2\ \mu m$.

Steppers also shine a flux of UV light through a mask, but the transmitted pattern is rescaled by an imaging lens before exposing the resist. Therefore, by using a stepper a smaller pattern can be made on the resist than that on the mask, which can potentially improve the resolution compared to the contact aligners. A stepper can also be used to repeat a single pattern on the mask and populating it through a whole wafer, like a step-and-repeat camera. The Nikon NSR-2005i8A stepper in WCNT has a scale ratio of 5:1 (i.e., the resist pattern is 5X smaller than the mask) and a resolution a little less than $1\ \mu m$.

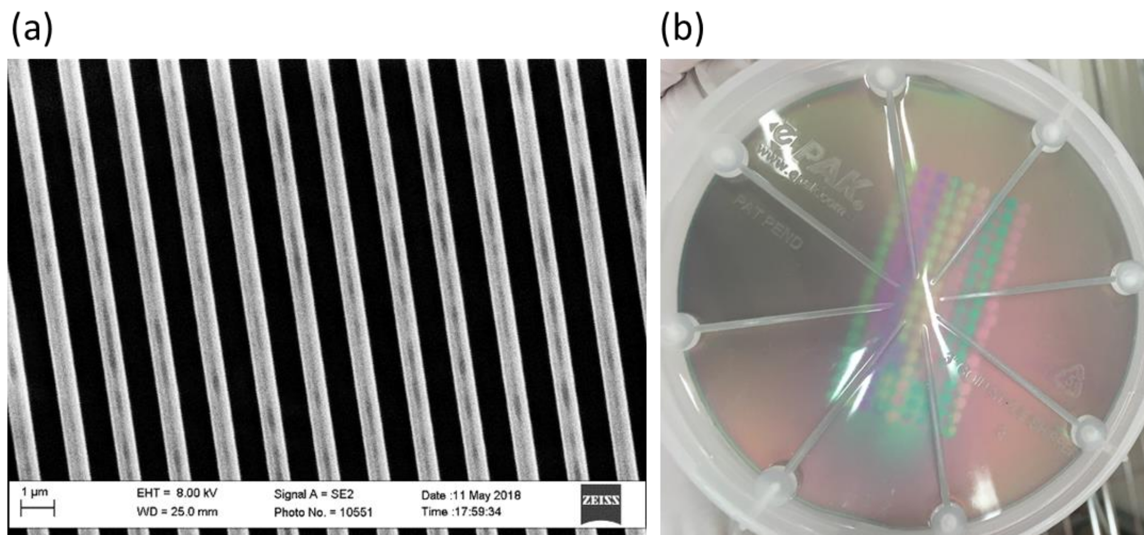

Figure 2.12 Our resolution test of contact aligners and the stepper in WCNT (a) $1\ \mu m$ resist strips made with the Karl Suss MA6 contact aligner in WCNT using Shipley 1813 resist. (b) A photo of the 3’’ test sample exposed with the Nikon NSR-2005i8A stepper in WCNT. The matrix

is of a single test pattern exposed under different conditions (with different focus and different dose). The smallest feature resolved is a square with $0.6\ \mu m$ side.

Since the photolithography tools at WCNT could not reach the resolution needed by our grating chip, we fabricated it using electron-beam lithography (Fig. 2.10). First, polymethyl methacrylate (PMMA) 495K A4 resist was spin coated on a 3-inch silicon wafer with speed of 1500 rpm for 90 s, then baked under 180 ℃ for 1 min. The resist thickness was measured using a thin-film reflectometer to be about 250 nm. Then the resist was exposed using an Elionix G100 electron-beam lithography system, with $120\ \mu m$ objective aperture, 10 nA current, and stitching thousands of square fields, each 0.1 mm on a side. The periodicity is oriented along two diagonal lines of the grating to maximize the trapping region (Fig. 2.13).

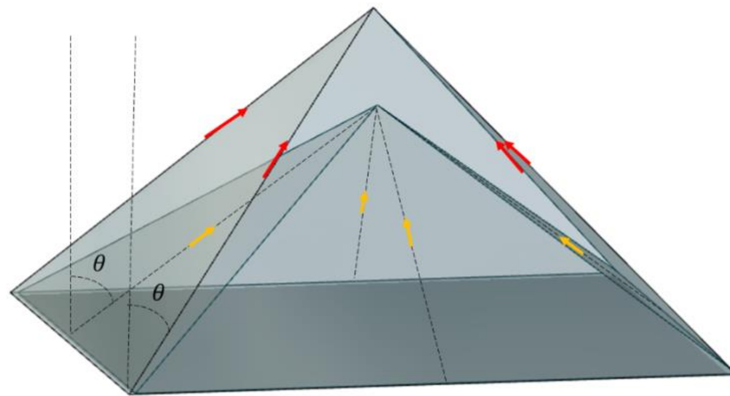

Figure 2.13 The trapping region of a square grating chip whose periodicity is either along the chip diagonal (the higher pyramid) or along the chip edge (the lower pyramid). θ is the diffraction angle. The diffracted beams are either bending towards the diagonal direction (red) or bending towards the chip edge (yellow).

A reference $1mm \times 1mm$ grating was exposed right next to the $8mm \times 8mm$ grating for future characterization. It took 51 hours to expose the whole 65-mm^2 region. We note that this is much longer than a typical e-beam writing session in our cleanroom or any academic facility, and can be

problematic due to potential interruption, stage vibration, current drifting etc. In fact, to our knowledge, this exposure session is by far the longest e-beam session conducted at WCNT, with an expense of ~$2,500 for this single process step. There are a couple ways to reduce the exposing time which we are exploring now, including using a more sensitive e-beam resist (ZEP), and use deep UV photolithography tools that has higher resolution. In principle, the exposure time could also be reduced by writing with at a higher current, but we found that a larger current could also cause shape distortion and stitching lines between writing fields (Fig.2.14).

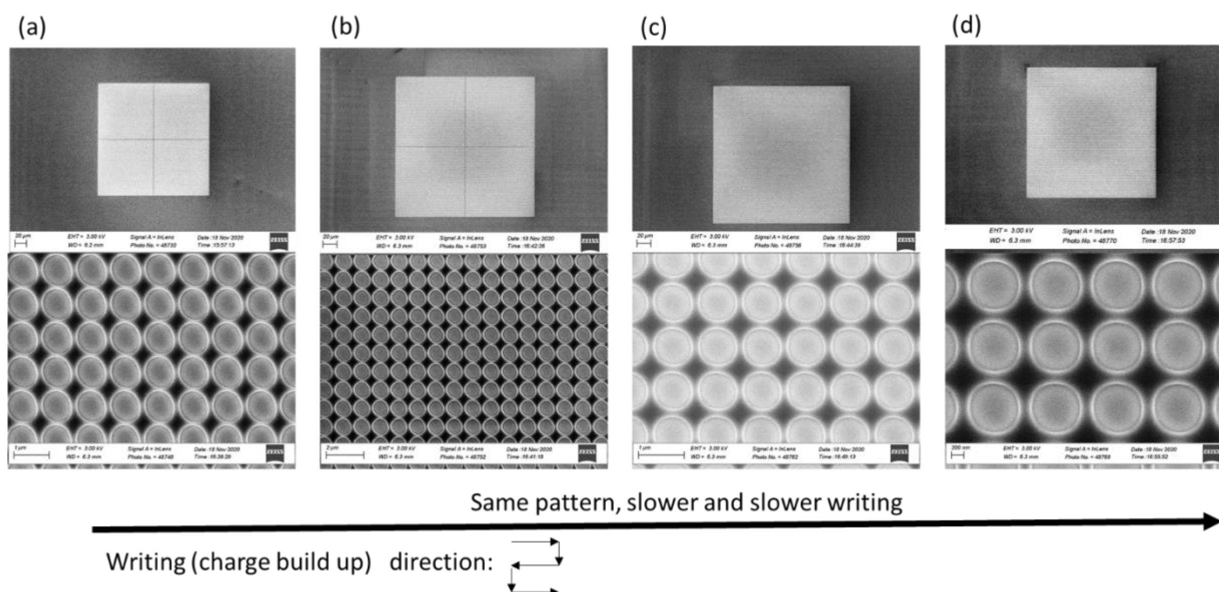

Figure 2.14 Circular-array patterns exposed on PMMA resist at different settings. (a-b) were both exposed with a 10nA current and a 240 um aperture, (a) had scan/feed pitch = 10nm. (b) had a scan/feed pitch = 6nm. (c) was exposed with 10nA current and a 120um objective, a 6nm pitch. (d) was exposed at 5nA, with a 120um objective and a 4nm pitch. All samples were exposed in the same “snake” direction, starting from top left scanning to the right then down. The writing of each test pattern (200um on a side) was divided into 2x2 100um-side fields. As far as we can tell, during the exposure, charge was slowly building up because of the high current we used. As a result, the bottom right corner of a single circle is more distorted than the top left corner; and the charge near the field boundaries deflected incoming electrons, forming a “stitching line” between fields. By slowing down the exposure, charges have more time to dissipate, thus the pattern becomes less distorted, and the “stitching lines” disappear.

We developed the resist at room temperature using a mixture of 1 volume of Methyl isobutyl ketone (MIBK) and 3 volumes of isopropyl alcohol (IPA) for 35 s [Fig. 2.16(b)]. This particular recipe was adapted from Zongfu Yu's group at UW-Madison. We included a post-developing baking under 100 ℃ for 1 min. Previously, we have found that an isotropic etch with O_2 plasma (also called "descum") can clean up potential resist residue (Fig. 2.15), so we included a 1 min descum with 250W power and 5 Torr pressure, which causes the resist to thin down by 20 nm, measured by a thin film interferometer.

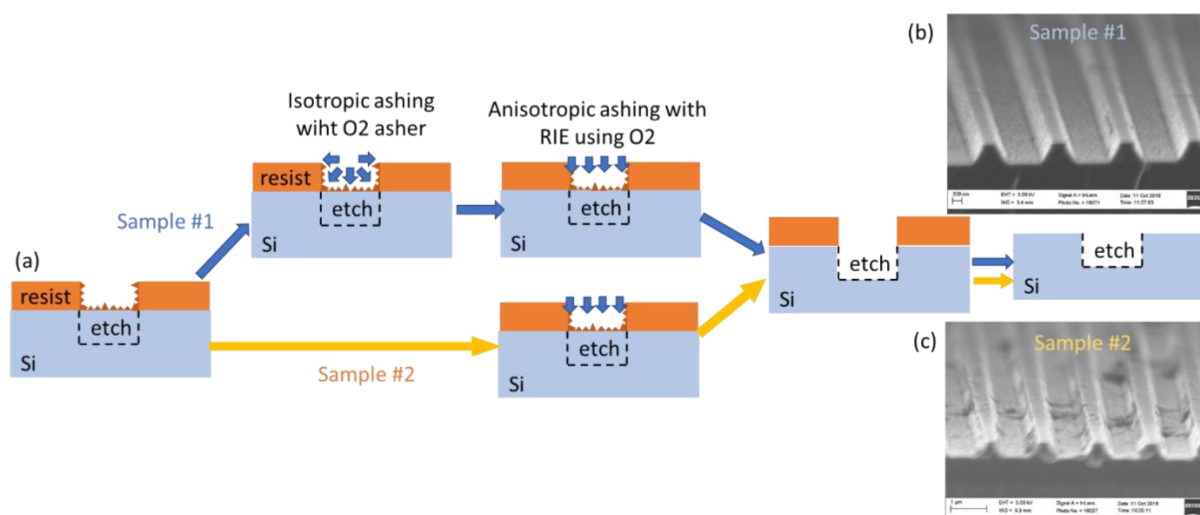

Figure 2.15 Cleaning resist residue with descum. (a) The fabrication flow. Two samples went through the same photolithography process. Then sample #1 went through a descum process before RIE (following blue arrows), while sample #2 did not (following gold arrows). After etching, sample #1 with an extra descum step has a much cleaner surface (b) than sample #2 (c).

After the descum, the pattern was transferred from resist mask to silicon by reactive ion etching. The etchant is mainly SF_6 (42 sccm) with the help of O_2 (5 sccm) under 14 W and 8 mTorr pressure for 3 min. The power is low relative to other Si-etching recipes, and we later discovered that this power resulted in unstable etching and surface roughness [Fig. 2.16(e)]. Luckily the roughness for this sample is later smoothened out after adding the thick metal coating [Fig. 2.16(c)], and did not cause too much scattering [<10% as shown in Fig. 2.17(c)]. The etching depth is around

$230\ nm$ from previous calibration. In the calibration using a test silicon piece, we first covered half of the silicon surface with mylar tape, then spin coated PMMA resist. After coating, we removed the tape, leaving a no-resist region with a sharp boundary. Then we etched the test sample, removed the resist mask, and measured the step height using a contact profiler (KLA-Tencor P7). The PMMA mask became $45\ nm$ thinner during the etching due to finite etch selectivity between the resist and the silicon.

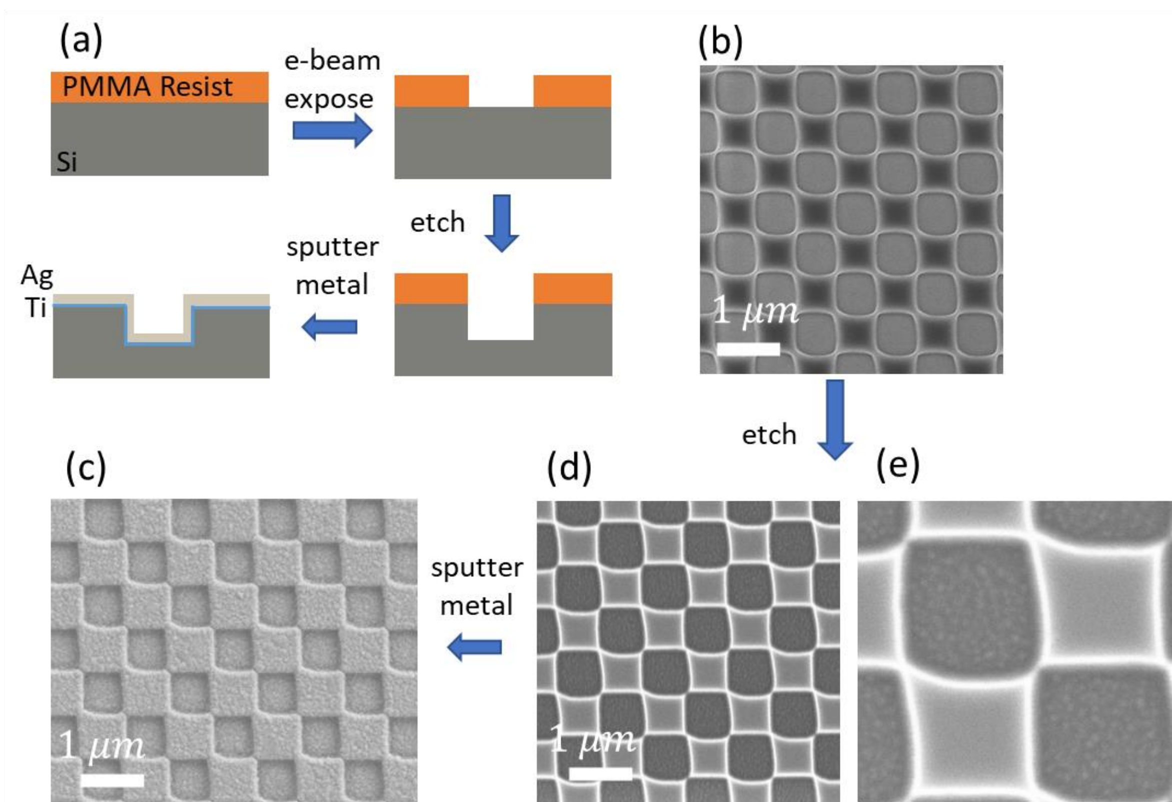

Figure 2.16 The fabrication of the checkboard 2D grating chip. (a) The flow of the fabrication. We started with spin coating the e-beam resist (495K A4 PMMA) on a single-crystalline Si substrate; then we defined the pattern on the resist by e-beam lithography [with an SEM of the resist pattern in (b)]; after that the pattern was transferred to Si by reactive ion etching [with SEMs of the etched Si with the resist mask shown in (d), and (e). (e) shows the surface roughness at the etched region as bright dots in darker area]; finally, we stripped off the resist and sputtered metal coating (a thin titanium layer is added to enhance the adhesion between the 130nm Ag film and the Si substrate) with an SEM in (c). Brighter region in (c) represents the higher square posts. The pattern is distorted since e-beam (b). We suspect the distortion is caused by the accumulated

charges during the exposure which deflect incoming electrons, since we are writing at a large current ($10\ nA$).

After the pattern has been transferred, we stripped off PMMA resist by soaking in heated ($90°C$) 1165 remover for a couple minutes then rinsed with acetone, IPA, and DI water. Then $130\ nm$ thick reflective silver film was sputtered on top. A thin Ti adhesive layer was sputtered before silver to enhance the adhesion between silver and silicon [SEM in Fig. 2.16(d)].

We measured the diffraction beams from the checkboard grating using a setup in Fig. 2.17(a-b), set up in the lab of Mark Saffman. A Gaussian beam is passing from a single-mode fiber to shine from top down. The half waveplate ($\lambda/2$) in (a) is for adjusting the incident power. Misaligning the waveplate with the polarization from the fiber will decrease transmitted power. The polarized beam splitter (PBS) and the quarter waveplate ($\lambda/4$) produce circular-polarized light that is incident on the grating. The power of the four 1st order diffraction beams are measured directly using a power meter. The power of the 0th order (direct reflection) is measured on the right of the PBS. This assumes most of the direct reflection have an opposite handedness with the incident beam, and is reflected by the PBS to the right. Since not all of the direct reflection flips handedness, the measured power of the 0th order diffraction is lower than of the actual power. Regardless, the measured total reflection is above 90% for both wavelengths [Fig. 2.17(c)], compared to 80% of $780\ nm$ in reference [56]. The balancing efficiency is also $\eta_B \approx 90\%$ for both wavelengths, which agrees well with our simulation. The fabricated grating chip has a loss ~5% higher than the simulation, which could come from bad silver film quality. Based on this configuration, a rotational polarizer can be added before the power meter to measure the polarization of the diffraction beams (which will be discussed later for circular gratings).

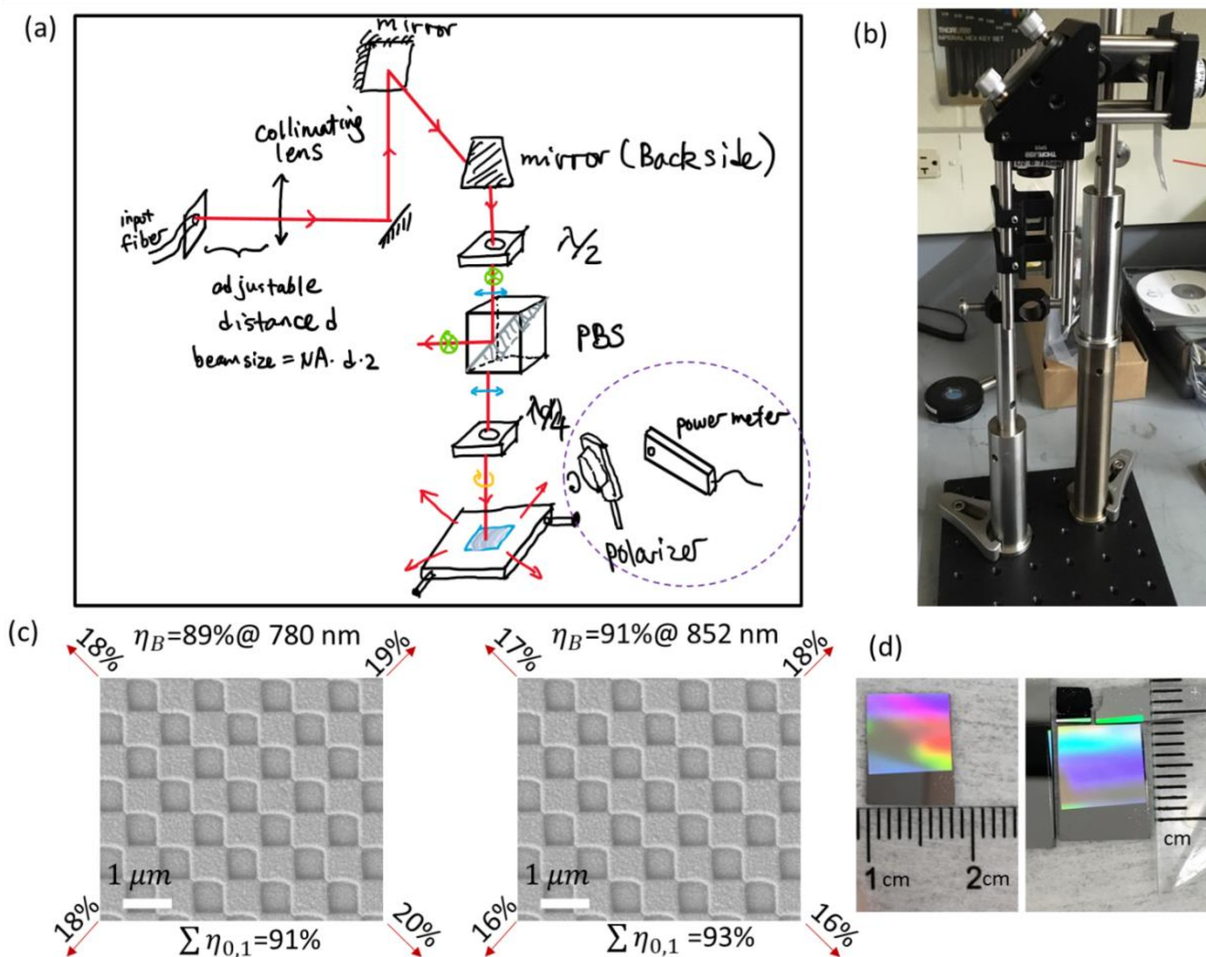

Figure 2.17 (a-c) measuring the diffraction beams of the checkboard grating. (a-b) optical setup of the measurement. (c) Diffraction efficiencies under two trapping wavelengths, which provide a 90% radiation balance for both wavelengths. (d) Pictures of the hand-diced grating. The patterning region is $8mm \times 8mm$, with a $2\ mm$ handling bar at the bottom. The grating is slightly cut off on two edges.

After we verified the fabricated checkboard grating can provide ~90% balancing efficiency for both trapping wavelengths, we cut it out from the 3-inch wafer to load into the vacuum chamber. At the time when we fabricated the checkboard grating, a high-precision dicing saw was not available in WCNT. Thus, I hand cleaved it as shown in Fig. 2.17(d), where the grating is slightly

cut off on two of the edges. We do have some concerns that cleaving may have damaged the films.

After we loaded the grating into the chamber, loaded in rubidium atoms, we did not find a MOT despite significant efforts by our collaborators in the Saffman group, especially Jin Zhang and Eunji Oh. We took out the grating chip from the vacuum chamber, and retook the SEM, where we found a damaged film [Fig. 2.18(b)]. It is also possible that the film was damaged by rubidium atoms, so in future steps we added a protective oxide layer.

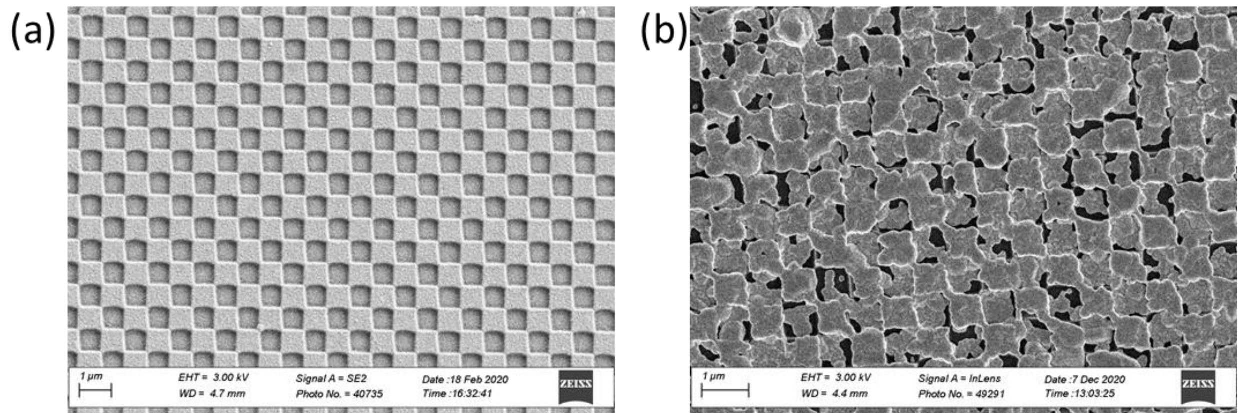

Figure 2.18 Damaged metal coating on the checkboard grating chip after cleaving, loaded into the vacuum chamber, in contact with rubidium atoms for multiple times in 8 months. (a) A reference SEM taken after fabrication [same as Fig. 2.16(c)]. (b) SEM of the damaged coating.

There are a couple of lessons we had learned from this damaged checkboard grating, which we incorporate in fabricating future gratings (Fig. 2.19). First, we found that, due to the existence of shape distortion, which is likely from charging during e-beam writing at high current, checkboard gratings can form narrow metal gaps [e.g., the red circled gap in Fig. 2.19(a)], which may lead to light loss and also poor balancing of the diffraction orders. Therefore, we changed to a more distortion-tolerant circular gratings, as shown in Fig. 2.19(b). Second, to avoid film lamination, the chip should be diced prior to adding metal coating. At the time when we were fabricating the circular grating, a new Disco dicing saw was installed in the WCNT, which is programmable and

can place dicing blade with a positioning accuracy better than 50 μm. We chose to use this automated machine instead of cleaving by hand to avoid cutting off the grating edge like in Fig. 2.19(d). Since the vacuum chamber has a 1cm-wide narrow neck [marked red in Fig. 2.19(c)], we only have 1mm tolerance of dicing on each side, which is hard to achieve by hand. Using the saw, we were able to dice a 8.3 mm wide (both edges have a 0.15 mm spacing) and 11.1 mm long (0.1 mm on one side, 3 mm on the other side as a handling bar) piece. Third, to protect silver film from degrading and damaged by atoms in the chamber, we added a protective oxide layer, as illustrated by the layer structure of the circular grating in Fig. 2.19(f).

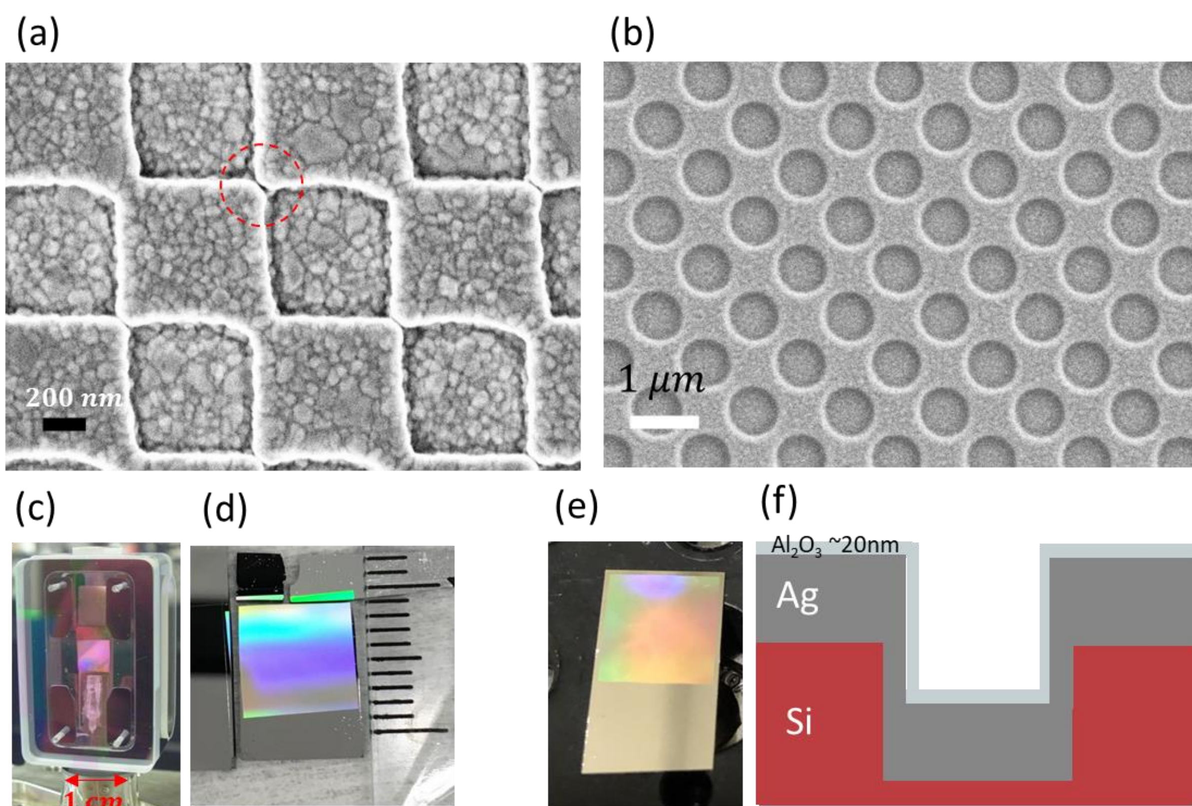

Figure 2.19 Differences between the checkboard grating and the circular grating. (a-b) The circular pattern is more tolerant to distortion during e-beam and does not form narrow gaps like the one circled red in (a). The hole array is measured an average radius of 340 nm. (c) The vacuum chamber with a narrow 1 cm neck requires an accurate dicing of the 8 mm grating chip. (d-e) The

circular grating was accurately diced prior to adding the metal coating. (f) The circular grating has an oxide protective layer.

After fabricated the circular grating chip, we measured the diffraction power [Fig. 2.20]. A higher total reflection and balancing efficiency were measured of the circular grating than those of the checkboard grating, which we attribute to narrow gaps existing in the checkboard grating causing light loss. We also characterized the patterning depth of 190 nm using AFM. Using the measured patterning depth (T) and the measured hole radius (r) in Fig. 2.19(b), we checked our FDTD simulation with this grating structure, and compared the simulated diffraction power with the measured power. We found that they agree well (Appendix).

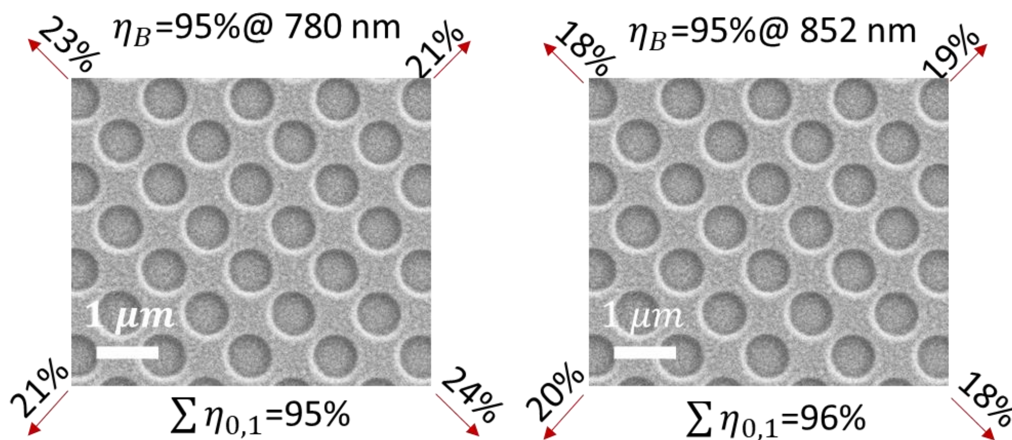

Figure 2.20 The diffraction efficiency and the balancing efficiency of the circular grating at 780 nm (a) and 852 nm (b). Both the total reflection and the balancing efficiency of the circular grating chip are higher than that of the checkboard chip, which could be attribute to narrow gaps existing in the checkboard grating causing light loss.

We also checked the polarization of the 1st order diffraction beams using a rotating polarizer and a power meter, and plotted the transmitted power over the orientation of the polarizer (Fig. 2.21). We evaluate the polarization by defining the degree of linear polarization ($DOLP$), which is the contrast between the max and the min power in this measurement:

$$DOLP = \frac{P_{max} - P_{max}}{P_{max} + P_{max}} \quad \text{Eq. (2.4)}$$

For linearly polarized light, max power is measured when the polarizer aligns with the beam with $P_{max} = P_0$, min power is measured when the polarizer is perpendicular to the beam with $P_{min} = 0$. Thus for a linearly polarized beam $DOLP_{linear} = 1$. For a circularly polarized light, the transmitted power will be constant regardless of the polarizer orientation, i.e., $P_{max} = P_{min} = P_0/2$, therefore $DOLP = 0$. For any other polarization, $DOLP$ lies in the range of $0 \sim 1$. For the diffraction beams measured in Fig. 2.21, we calculated their polarization to be $DOLP_{780nm} \approx 65\%$, $DOLP_{852nm} \approx 48\%$.

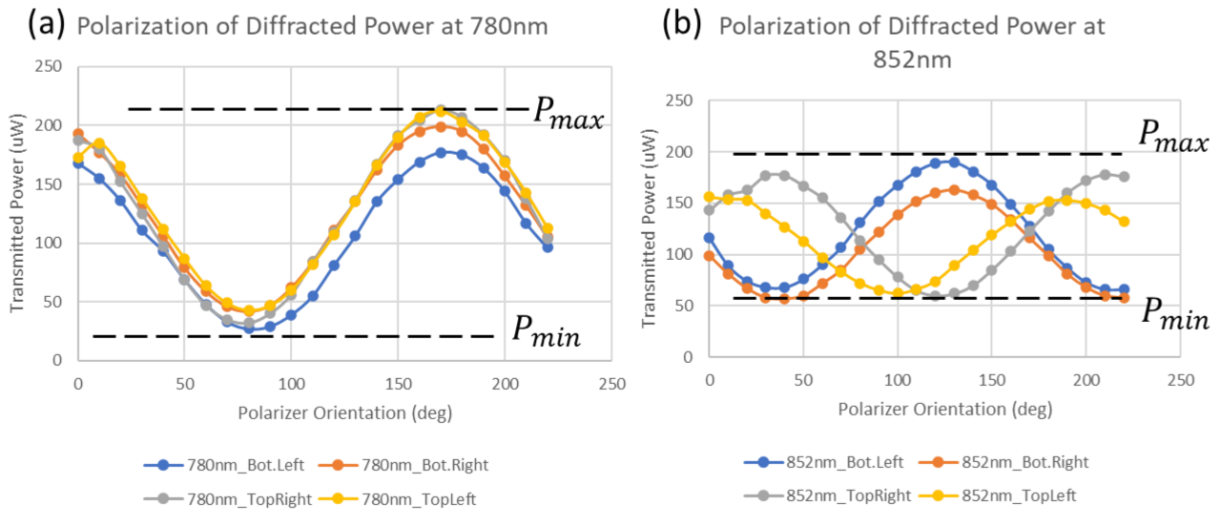

Figure 2.21 The polarization of the diffracted beams from the circular grating chip at two trapping wavelengths. Polarization of a beam is measured by the transmitted power through a rotational polarizer.

We then compared the measured $DOLP$ with the simulated results. We found the polarization of the diffracted beams is very sensitive to the thickness of the oxide layer at $780\,nm$ wavelength [Fig. 2.22(a)]. By using a $20nm$ Al_2O_3 layer

(with $15\,nm$ sidewalls), we were able to match the polarization ellipse at $780\,nm$ wavelength from simulation and from measurement [Fig 2.24(b vs c)]

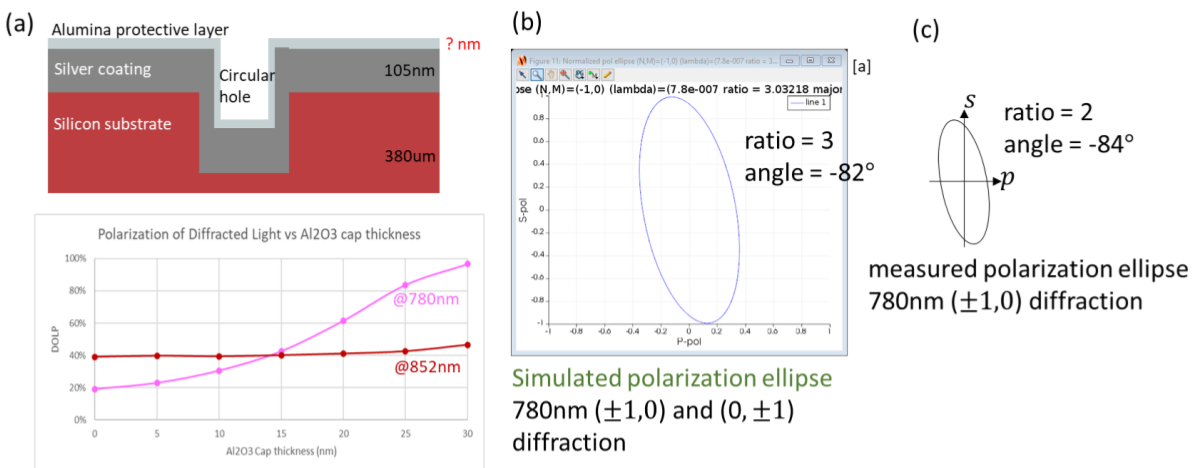

Figure 2.22 (a) The polarization of the diffracted beam of circular grating chips with different thickness of the alumina cap. (b-c) The polarization ellipse of 1st order diffractions at 780nm wavelength from simulation (b) and from measurement (c).

After we fully characterized the circular grating chip, we loaded it into the vacuum chamber and tried to build a grating MOT, again in collaboration with the Saffman lab. However, to date we have not been able to identify a MOT despite sweeping of various parameters and a number of attempts. We are continuing to analyze potential causes for why we are not seeing the MOT, including an attempt from my colleague Sanket Deshpande, who has been building a tool to calculate and visualize the forces in a grating MOT. I am previewing his calculation below.

Calculating force on atoms from calculated or measured optical performance of the gratings

Based on the diffraction power and polarization from FDTD simulations or from measurements, we can calculate the scattering force profile using:

$$\boldsymbol{F} = \frac{\hbar k \Gamma}{2} \sum_{j=1}^{N} \sum_{q=-1,0,1} \frac{\frac{I_{jq}}{I_S}}{1 + \frac{4(\Delta - \delta_q)^2}{\Gamma^2} + \frac{I_T}{I_S}} \hat{k}_j \qquad \text{Eq. (2.5)}$$

where $k = 2\pi/\lambda_{inc}$ is the wavenumber; $\Gamma = 2\pi \cdot 6.07$ MHz is the natural linewidth and $I_s = 3.58\ mW/cm2$ is the average saturation intensity; $\delta q = q\mu_B g_e B/\hbar$ where μ_B is Bohr magneton, g_e is the excited state Lande facto rand B is the magnetic field intensity; j identifies each of the N =6 beams (four 1st orders, one 0th order, one incident beam). $I_{jq} = I_j \left|\varepsilon_j^* . \varepsilon_{Bq}\right|^2$, where ε_j is the beam's polarization vector and ε_{Bq} is the magnetic field polarization vector expressed in the spherical basis; $I_T = \sum_{j,q} I_{jq}$. We set up our simulations with commonly used parameters for achieving a MOT. For example, at 780 nm for a ^{87}Rb MOT: we set detuning $\Delta = -2\Gamma$, intensity $I_{inc} = 3I_s$ incident normally along with $dB/dz = 10\ G/cm$. The results are shown in Fig. 2.23:

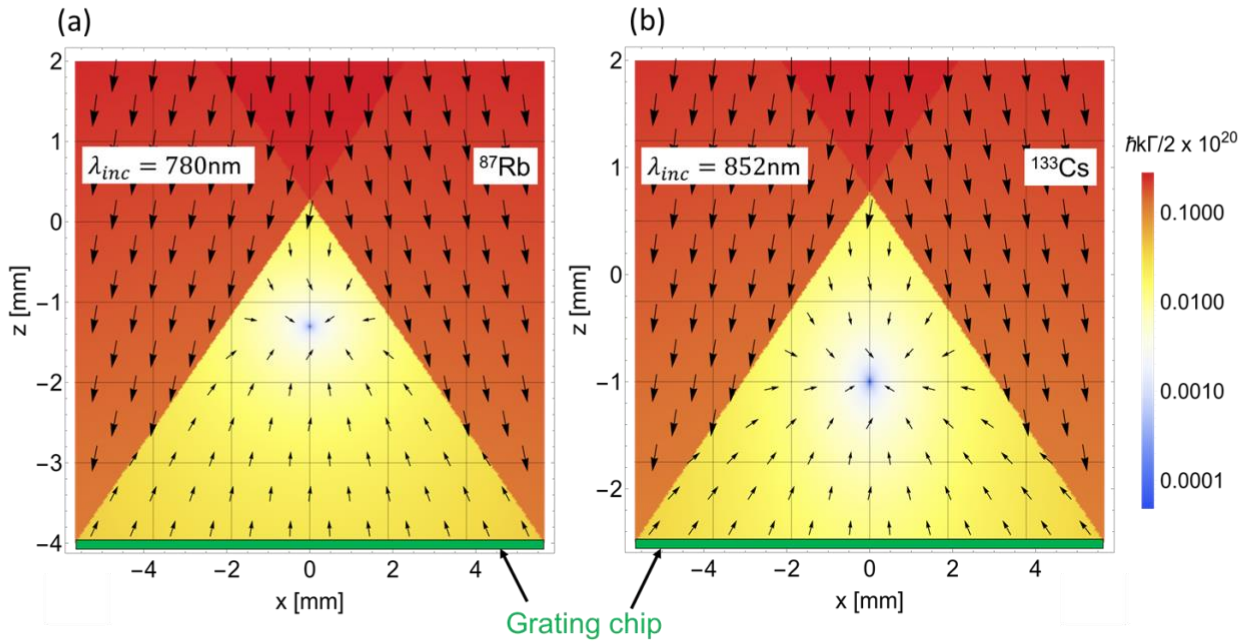

Figure 2.23 calculated scattering force profile at 780 nm (a) and 852 nm (b). The force profile shows that there is a trap center (white/blue region with surrounding arrows pointing to it) at both wavelengths. The calculated trap center is 2~3 mm above the grating surface. [36]

The calculated force profile shows that there is a trap center for both wavelengths (represented by blue dots indicating zero or balanced force in Fig. 2.23), which is 1~2 mm below the magnetic field zero ($z = 0$). This makes sense because the grating chip has loss and the balancing efficiency $\eta_B < 1$, so the atoms are pushed to a lower place. The predicted trap centers are located 2~3 mm above the grating surface. Note that atoms at a mm-scale distance away from a surface has been reported to be problematic due to collision between atoms and the grating surface [73], [74], and induced electric field that lead to Stark shifts [54]. In the future, we plan to increase this distance by fabricating larger gratings, and possibly by using a larger grating period (which result in a higher trapping pyramid as discussed previously in Eq. 2.4).

Conclusion and future work

In conclusion, we investigated diffractive chips for simultaneously trapping Rb and Cs atoms with 780 nm and 852 nm lasers, respectively. We used full-wave simulations to determine the impact of different duty cycles, heights, metal coatings, and fabrication defects on the diffracted power, and thus the balancing efficiency (η_B) of the chip. We also calculated the radiation force profile based on the simulated diffracted power and polarization. We fabricated a 2D grating chip that has optimized geometry for trapping both atom species, and the measured diffracted power and polarization is roughly as expected. Even though our calculation show that the current fabricated grating should be able to generate a trap, we have not yet found a trap with Rb atoms. One potential

cause is the target trap is too close to the grating surface which increases loss of atoms due to their collision with the surface. We are now exploring different methods (including laser lithography and faster e-beam lithography with ZEP resist) to fabricate a bigger grating with 2-cm side instead of 8 mm so that the target trapping center can be further away from the grating surface.

Metasurfaces for efficient generation of optical bottle beams

The introductory material in this Chapter is largely adapted from section 9.5-6 of "Atomic Physics" by C. J. Foot [75]. A large part of the new research in this Chapter has been previously published as Y. Xiao, Z. Yu, et al., "Efficient generation of optical bottle beams," *Nanophotonics* (2021) [76]. The computation work was led by Yuzhe Xiao, with contributions from me. The fabrication work was led by me and has not yet been published outside of this thesis.

Atom trapping with optical bottle beams

In the magneto-optical traps (MOTs) I discussed in Chapter 2, atoms are trapped by the scattering force, in which momentum is transferred to atoms by absorbing then re-emitting photons. On the other hand, at large-frequency detuning ($|\delta| \gg \Gamma$ and $|\delta| \gg \Omega$, where $\delta = \omega - \omega_0$ is the frequency detuning, Γ is the natural linewidth, and Ω is the Rabi frequency), the scattering cross-section is low, but atoms can still be trapped by the dipole force. The dipole force is proportional to the gradient of the light intensity, and pulls the atom towards an intensity maximum/minimum

depending on whether the frequency detuning is negative/positive. The particle analog of the dipole-force trap is known as optical tweezers (2018 Nobel Prize in physics), in which micro- and nanoparticles can be either attracted to a high-intensity focus or repelled from it, depending on whether the refractive index of the particle is higher or lower than that of the ambient media.

The detailed derivation of the scattering and the dipole force can be found in the Appendix. Note that unlike the scattering force, where momentum is transferred from photons to the atom, the dipole force acting on an atom is conservative [Eq. (S.15) in the Appendix], which means a moving atom outside of a dipole-force trap will first accelerate to the trap center and then exit the trap due to the conservation of energy. Therefore, pre-cooling (with MOTs or other techniques) is needed to dissipate energy before carefully loading one or more atoms at the center of the dipole-force trap.

The first dipole-force trap is demonstrated in 1986 by Steven Chu and others using a red-detuned focused Gaussian beam, where estimated 500 sodium atoms were first cooled by the optical molasses technique and then trapped to the high-intensity focus. Since then, red-detuned traps have been widely used in quantum computing [77], rapidly producing Bose-Einstein condensates (BEC) [78], and micromanipulation of neutral atoms [79].

Comparing to red-detuned dipole-force traps which confine atoms at intensity maxima, atoms in a dark center of a blue-detuned dipole trap can have a low scattering and reduced heating (with a scattering rate of $R_{scatt} \propto I_0/\delta^2$, where I_0 is the light intensity of the dark center of the trap) thus

a much longer coherence time [80]. The bottle-beam trap is one type of blue-detuned dipole trap where atoms at the dark center of the trap are confined by the surrounding higher-intensity wall, as if in a bottle. The trapping depth of a bottle-beam trap is determined by the least intensity contrast [with the dipole-force $U_{dipole} \propto (I_{escape} - I_0)/\delta$, where $I_{esacape}$ is the minimum intensity of the bright walls surrounding the trap center, i.e. the "shortest bar of the barrel" as shown by the inset of Fig. 3.1(b)].

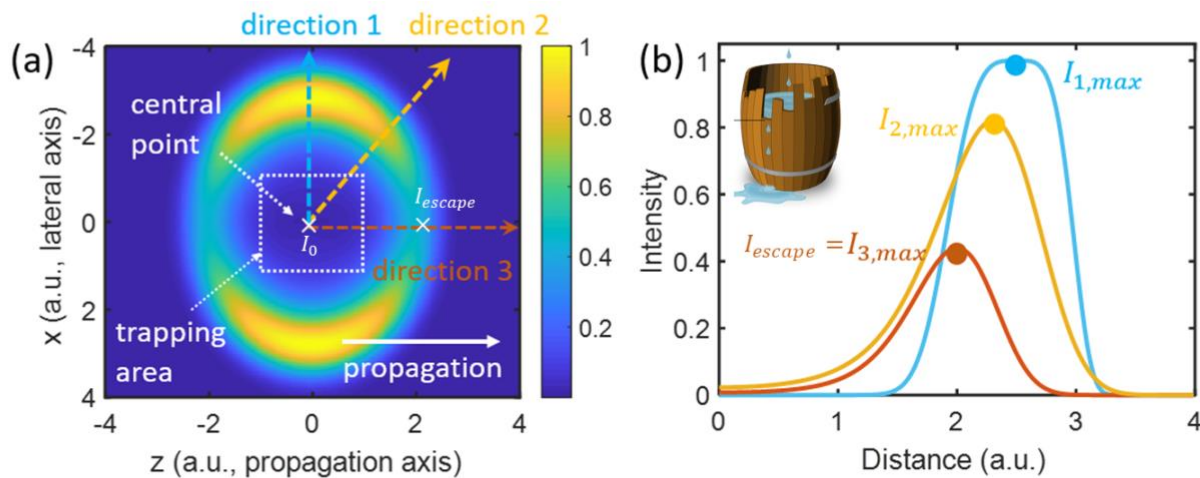

Fig. 3.1 (same as Fig. 1 in *[76]*). An example of an optical bottle beam. (a) Intensity profile of an optical bottle-beam trap in the x-z plane. The beam propagates along the z direction and is rotationally invariant along the z axis. Intensity profiles along three different directions are shown in (b). The inset depicts the wooden barrel theory, where the capacity of the barrel is determined by the shortest bar. Similarly, the escape intensity of the trap is defined by the minimum intensity of the surrounding wall, for the trap in (a) $I_{escape} = I_{3,max}$. Source of the inset in (b): http://www.pvisoftware.com.

Various techniques have been used to create bottle-beam traps, including the interference of two Gaussian beams where destructive interference at the mutual focus of the beams result in an optical bottle [7], vortex beams with a dark hole in the center [81], a single Gaussian beam plus a

computer-generated hologram (CGH) film that records the amplitude of the destructive interference pattern [82], a spatial light modulator that displays the hologram [83], [84], a diffractive optical element (DOE) [85], or a metasurface ring grating [86]. The bottle-beam trap created by a single Gaussian beam illuminating an optical metasurface has the advantage of compact size and a potential for chip-scale trapping [86]. The bottle-beam metasurface in [86] explored phase profile in one dimension (1D) with concentric rings. In this work, we focus on metasurfaces that can provide a two dimensional (2D) arbitrary phase profile using an array of nanocylinders, with the hope that the extra dimension may improve the performance of the bottle-beam traps.

However, as far as we could tell, there is no agreed-upon figure of merit to compare bottle-beam traps, so in [76] we start with designing several such figures of merit. We first notice that one can imagine at least two types of bottle-beam traps depending on the trapping object: point traps for trapping atoms at a particular point, and volume traps for trapping small particles inside a μm^3-scale volume. Note that traps with a μm^3-scale dark region may also be useful for Rydberg atoms, which can have large electron wavefunctions.

For a point bottle-beam trap, we only worry about the minimum intensity at a particular point, while for a volume trap the average intensity over the trapping volume needs to be minimized. We then define the figure of merit (FoM, or η) of a bottle-beam trap as the trapping depth the trap can provide (measured by the intensity contrast $I_{escape} - I_0$) with a given incident power (P):

$$\eta = \frac{I_{escape} - I_0}{P} \cdot (10^{-9}\, m^2), \qquad \text{Eq. (3.1)}$$

where I_0 is the intensity of the dark center for point traps or the averaged intensity over the trapping volume for volume traps, $10^{-9}\, m^2$ is a coefficient to make η unitless with the scale ~100 for a couple-μm^3 trapping volume.

Take the bottle-beam trap demonstrated previously demonstrated by Saffman et al in 2009 [7], for example. The bottle beam is formed by two Gaussian beams which destructively interfere at the mutual focal point, as shown in Fig. 3.2. The two Gaussian beams have different beam waists and a π relative phase at the focus, and are combined by a beam splitter. The resulting bottle beam [Fig. 3.2 (b)] is rotationally symmetric along the propagation axis (z) and mirror-symmetric across the focal plane ($z = z_0$). The radial extent of the dark trap is close to the smaller beam waist, and the longitudinal extent depends on the relative Guoy phase.

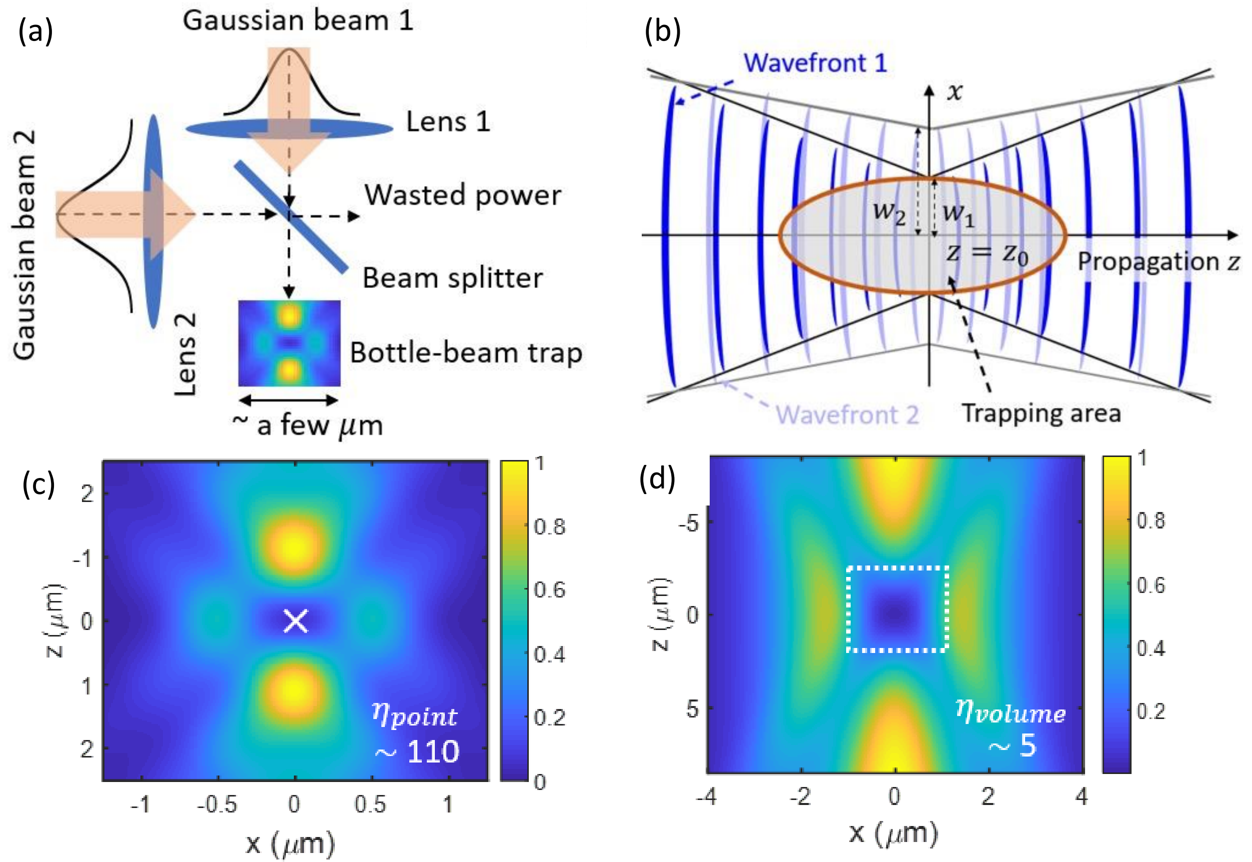

Figure 3.2 (Same as Fig. 2(c, a) and Fig. 3 (d,a) in *[76]*) Optical bottle beams formed by the destructive interference of two Gaussian beams. (a) Experimental setup: two Gaussian beams are combined after a beam splitter and forming a bottle beam. (b) Cartoon showing the light field near the trap center. The two Gaussian beams have different waists and a π phase shift at the mutual focus. The radial extent (e.g., along the x axis) of the low-intensity region (trapping volume) is roughly equal to the waist of the smaller beam, and the extent along the propagation direction (z axis) is determined by the difference in the waist-dependent Gouy phase. (c-d) The best bottle-beam point trap (c) and volume trap (d) achieved after running parametric sweep optimization over different combinations of w_1, w_2, and the relative amplitude A_2/A_1.

To calculate the FoM of the bottle-beam trap, we denote the waist of two incident Gaussian beams as $w_{1,2}$ where $w_1 < w_2$. The electric field of a Gaussian beam with an amplitude A and a waist w_0 at a spatial point with radial position r and longitudinal distance z can be written as:

$$E(A, w, r, z) = A \frac{w_0}{w(z)} \exp - \frac{r^2}{w(z)^2} \exp[-i\left(kz + k \frac{r^2}{2R(Z)}\right) - \psi(z)], \qquad \text{Eq. (3.2)}$$

where wave vector $k = 2\pi/\lambda$, beam radius $w(z) = w_0\sqrt{1 + (z/z_R)^2}$, Rayleigh range $z_R = \pi w_0^2/\lambda$, radius of curvature for the wavefront $R(z) = z[1 + (z_R/z)^2]$, and Gouy phase $\psi(z) = \arctan(z/z_R)$. So, the electric field of the two incident Gaussian beams are:

$$E_1(A_1, w_1, r, z) = A_1 \cdot E_1(1, w_1, r, z),$$

$$\text{and } E_2(A_2, w_2) = A_1 \cdot E_2\left(\frac{A_2}{A_1}, w_2, r, z\right). \qquad \text{Eq. (3.3)}$$

Note that the global amplitude factor A_1 will be canceled out when calculating the FoM:

$$\eta = \frac{\Delta I}{P} = \frac{[(\Delta\tilde{I})A_1^2]}{[(\tilde{P})A_1^2]}, \qquad \text{Eq. (3.4)}$$

so there are only three independent parameters (relative amplitude A_2/A_1, and beam waists w_1 and w_2) which influence the superimposed bottle-beam field:

$$E(r, z) = E_1(1, w_1, r, z) - E_2\left(\frac{A_2}{A_1}, w_2, r, z\right). \qquad \text{Eq. (3.5)}$$

We ran a parameter sweep optimization with different combinations of $(A_2/A_1, w_1, w_2)$ to increase FoM in Eq. (3.4), and found the best point and volume bottle-beam traps created with this two-Gaussian method shown in Fig. 3.2 (c-d). The bottle beams we optimized use a wavelength of $\lambda = 770\ nm$ (blue detuned from ^{87}Rb resonance, for example for single-photon sources [87]). For volume traps we pick a trapping volume of $\pi \times (2\mu m)^2 \times 2\mu m$. For point traps, we observed that the FoM increases with the numerical aperture due to a wider range of radial wavevector (k_r), and we pick a numerical aperture (NA) of $\sin(45°) = 0.7$, which is considered feasible for future imaging systems to adjust the position and scale of the bottle-beam trap. Note that due to the destructive interference of two Gaussian beams, a significant amount power is wasted on the alternative path of the beam splitter [shown in dashed arrow pointing to the right in Figure 3.2(a)].

Designing bottle-beam metasurfaces

To improve on the figure of merit as well as to reduce the space and complexity of the optical setup for generating bottle beams, we decided to use optical metasurfaces. Briefly, optical metasurfaces are planer optical components comprising nano resonators which have spacing smaller than the operational wavelength, and can imprint an arbitrary phase modulation profile on an incident wavefront [9], [10].

Our scheme is to have a single Gaussian beam of light incident on a metasurface, where we engineer the phase profile across the surface to convert the Gaussian beam into a desired bottle beam [Fig. 3.3(a)].

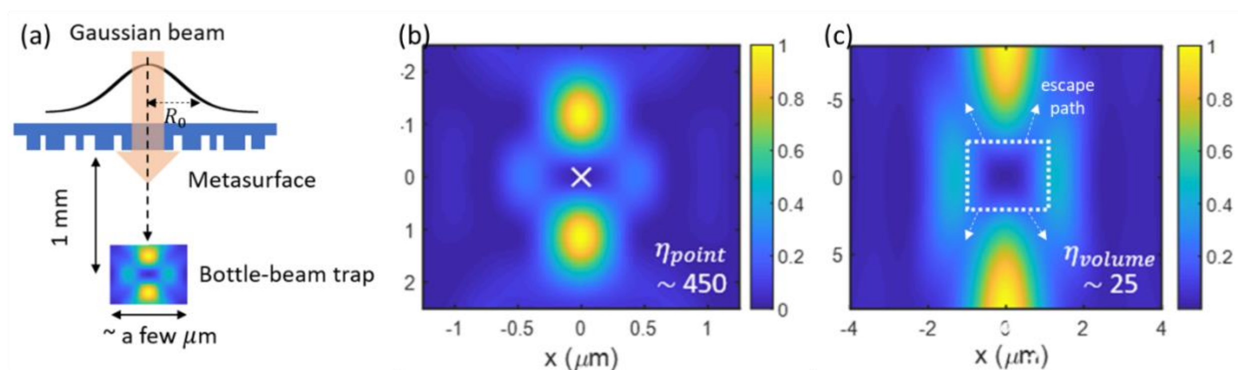

Figure 3.3 (Same as Fig. 2(d) and Fig. 3 (e, b) in [2]) Optical bottle beams formed by a single Gaussian beam passing through a metasurface with an appropriate phase profile (a) Schematic of a setup: the illuminating Gaussian beam has a beam waist R_0, after transmitting through the metasurface with designed phase profile, a bottle beam is formed 1 mm away from the metasurface. (b-c) The best bottle-beam point trap (b) and volume trap (c) achieved after running

parametric sweep optimization over different combinations of w_1, w_2, the relative amplitude A_2/A_1, and R_0 on the phase profile derived from destructive interference of two Gaussian beams.

To calculate the phase that the metasurface needs to impart, we performed a calculation using Fresnel diffraction [88] to derive the desired field profile on the metasurface plane [$E(r, z = z_m)$] from the field profile in the focus plane [$E(r', z = z_0)$]:

$$E(r,\ z_m) = \frac{e^{-ik\Delta z}}{i\lambda\Delta z} \cdot 2\pi e^{-\frac{ikr^2}{2\Delta z}} \cdot \int_0^{\infty} r' E(r', z_0) e^{-ik\frac{r'^2}{2\Delta z}} J_0(-2\pi r' r) dr', \quad \text{Eq. (3.6)}$$

where $\Delta z = z_m - z_0$ is the longitudinal distance from the trap center to the metasurface, r is the radial position the metasurface plane, r' is the radial position in the focus plane, the field profile at the focus plane is the destructive interference of two Gaussian beams given by Eq. (3.5), and $J_0(x) = \frac{1}{2\pi}\int_0^{2\pi} e^{ixcos(\theta)} d\theta$ is the zero-order Bessel function of the first kind. The phase modulation of the metasurface equals to the phase difference between the desired field [$E(r, z_m)$ in Eq. (3.6)] and the illuminating Gaussian field:

$$\Delta\phi(r) = arg[E(r, z = z_m)] - arg[E(1,\ R_0,\ r, z = z_m)] \quad \text{Eq. (3.7)}$$

Similar to the two-Gaussian method above, we ran a parameter sweep optimization using different combinations of (A_2/A_1, w_1, w_2, R_0). To keep a 0.7 NA, we set the radius of the metasurface to 1 mm (a size straightforward to manufacture using e-beam lithography within a reasonable amount of time) and the trap is formed $\Delta z = 1\ mm$ away from the metasurface. The best bottle-beam traps achieved [Figure 3.3(b-c)] have much higher FoM compared to those created with the two-Gaussian method due to a more efficient use of power compared to the combination of two Gaussian beams using a beam splitter.

We then took another approach to design the bottle-beam metasurface, using a transmission-phase profile derived from a self-curved beam (also called an accelerating beam [89]) enclosing a dark ellipsoid for trapping. Such concept has been demonstrated with acoustic waves in [90], [91], and we take the same approach using light waves.

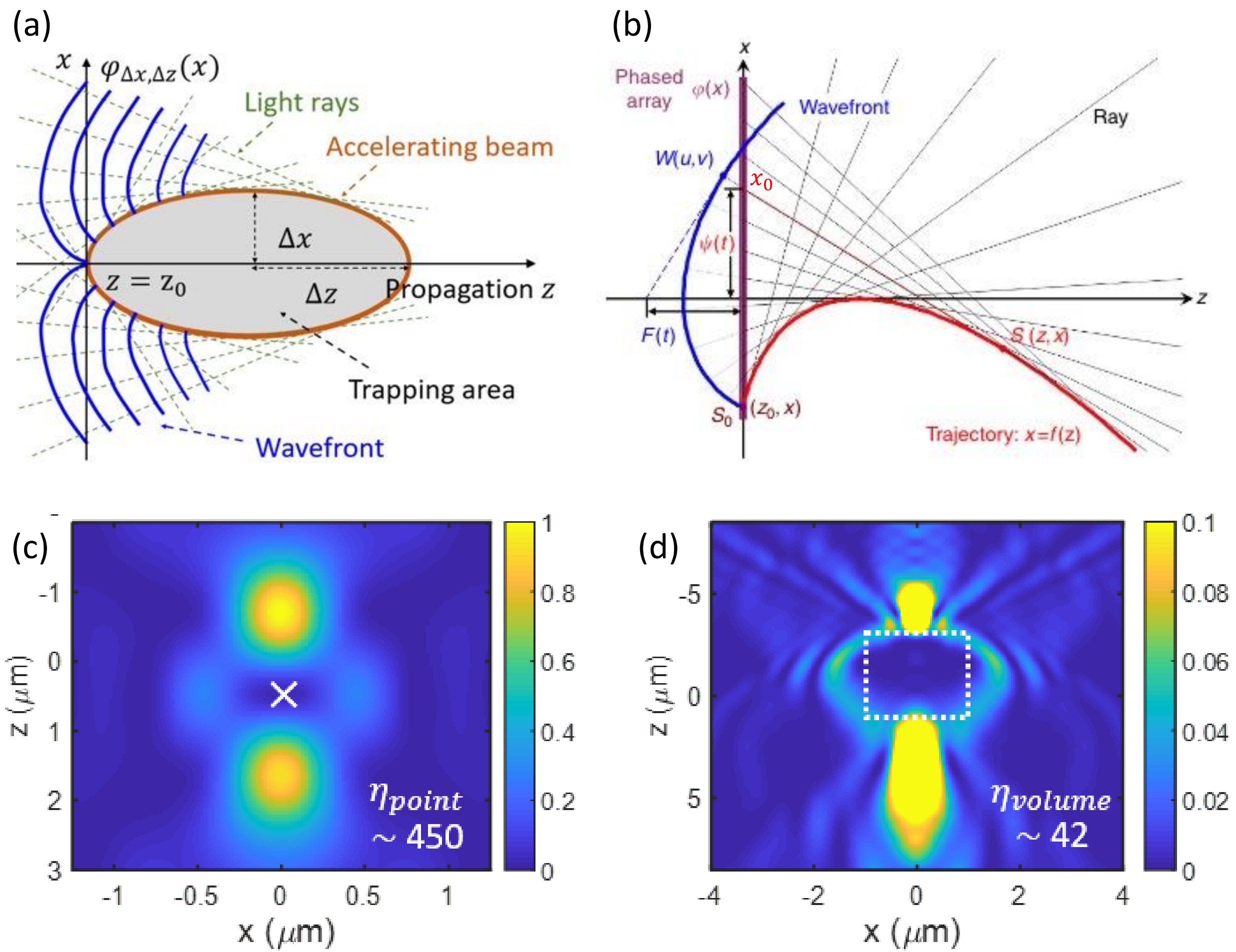

Figure 3.4. Optical bottle beams formed by a single Gaussian beam passing through a metasurface with a phase profile derived from an accelerating beam. The schematic of the setup is same as Fig. 3.3 (a). (a) An optical bottle beam with a curved envelop (solid orange ellipse with two axes being Δz, Δx), which can be constructed using multiple asymptotic tangential rays (shown in dashed

green, with the wavefront marked in solid blue). (b) Legendre transformation from a self-bending trajectory $x = f(z)$ (shown in solid red) to the mapping between the slope (t) and the intercept (ψ) of the tangential lines. (c-d) The best bottle-beam point trap (c) and volume trap (d) achieved after running parametric sweep optimization over different combinations of Δz, Δx, R_0 (the width of the illuminating Gaussian beam), and r_0 (the width of an approximate Gaussian intensity profile at the plane $z = z_0$). (a, c, d) are the same with Fig 2(b) and Fig. 3(f, c) of ref [76], (b) is adapted from Fig. (6) of ref [90].

As illustrated in Fig. 3.4 (a-b), a field with a bent envelope [red curve labeled $x = f(z)$ in Fig. 3.4(b)] can be decomposed into rays which are tangential to the envelope [shown as black dotted lines in Fig. 3.4 (b)]. To reconstruct these tangential rays, we need to calculate the phase retardation of the tangential rays while traveling from the source plane [the $z = 0$ plane marked purple in Fig 3.4(b)] to the envelope. Such calculation can be done using a Legendre transformation, which mathematically can convert a spatial trajectory $x = f(z)$ to the mapping from the slope (denoted as $t = dx/dz$) to the intercept (denoted as $\psi = x - zt$) of the tangential lines:

$$x = f(z) \rightarrow \psi = F(t) \qquad \text{Eq. (3.8)}$$

After the $\psi = F(t)$ is obtained, the tangential line can be written as $x = tz + \psi$. For any point on the source plane (with x coordinate being x_0), we can find its corresponding tangential point using simultaneous equations of the curve $x = f(z)$ and of the tangent line $x = F^{-1}(x_0) \cdot z + x_0$. If we denote the solution as (z_s, x_s), then the phase retardation at x_0 is:

$$\varphi(x_0) = k \cdot \sqrt{z_s^2 + (x_s - x_0)^2} \qquad \text{Eq. (3.9)}$$

Since the field is rotationally symmetric along propagation axis (z), Eq. 3.9 can be generalized to three dimensional using radial position r':

$$\varphi(r') = k \cdot \sqrt{z_s^2 + (x_s - r')^2} \qquad \text{Eq. (3.10)}$$

where the tangent lines with the desired envelope can be reconstructed using a source with the calculated phase profile $\varphi(r')$ on the source plane.

The envelope of the bottle beam [shown with solid orange line in Fig. 3.4(a)] is an ellipse with the curve function $x = f(z)$ being:

$$\left(\frac{x}{\Delta x}\right)^2 + \left(\frac{z}{\Delta z}\right)^2 = 1 \qquad \text{Eq. (3.11)}$$

Comparing to the bent envelope in Fig. 3.4(b), the closed envelope of the bottle beam has a phase-mapping ambiguity during the Legendre transformation. This is because the tangential asymptotic lines of the upper half of the trajectory will intersect with those from the lower half at the source plane. Therefore, besides phase modulation, a bottle-beam metasurface can also benefit from a deliberately designed amplitude profile which encodes the interference field amplitude between two intersecting tangential rays. An example of the calculated amplitude profile can be found in Fig. 8(c) of [90], which has a distribution like Newton's rings. We use a Gaussian intensity with an adjustable width r_0 to approximate the amplitude profile. As a result, the electric field on a nearby plane ($z = z_0$) to the trap center ($z = 0$) is:

$$E(r', z = z_0) = \exp(-\frac{r'^2}{r_0^2}) \cdot \varphi(r') \qquad \text{Eq. (3.12)}$$

Using Eq. (3.6) and Eq. (3.7), we can calculate the desired phase profile of the metasurface illuminated by a Gaussian beam with a waist R_0.

Similar to the other two previously described design processes which use different approaches to generate bottle-beam traps, we perform a parameter sweep optimization over different combinations of $(\Delta x, \Delta z, r_0, R_0)$, and the best bottle-beam traps achieved are shown in Fig 3.4 (c-d). We found that the best point bottle-beam trap achieved with a phase profile derived from either a curved beam [Fig. 3.3(b)] or a destructive interference pattern [Fig. 3.4(c)] has the same FoM and almost identical field profile. The fact that we converge to a similar result from two different approaches of designing metasurfaces may suggest that the achieved point bottle-beam trap is close to the global optimum with a high FoM. For volume traps, we found that using the metasurface with a phase profile derived from a curved beam [Fig. 3.4 (d)] yields a higher FoM than using the metasurface with a phase profile derived from the destructive-interference pattern [Fig. 3.3(c)]; this can be attributed to a couple of differences in the field profile of the achieved volume bottle-beam trap: (1) the confining higher-intensity wall of the volume trap created from a destructive interference pattern is not isotropic. As the result, the trap has four leaking paths marked as dashed arrows in Fig 3.3(c); (2) the intensity background in the trapping region ($I_0 \neq 0$) of the volume trap created from a destructive-interference pattern. Since the optimized average intensity ($I_{ave} = A/\pi w^2$) is not equal for two Gaussian beams ($I_{ave,1}/I_{ave,2} > 7$), the field cancelation in the destructive interference is imperfect; (3) the volume trap created from a curved beam has a thinner higher-intensity wall than the trap from a destructive interference pattern. Note that even though the trap with a thinner wall (occupying less area) yields a higher FoM based on Eq. (3.1), whether or not this means a better trap depends on the details of the application. In fact, traps with a gentle intensity slope [such as the trap in Fig. 3.3(c)] may be preferrable when loading an atomic cluster that spans over a volume, whereas traps with a thinner and steeper wall [such as the trap in Fig.

3.4(d)] may be more suitable for confining particles or Rydberg atoms with a size slightly smaller than the trapping region.

We chose to implement our bottle-beam metasurface using the concept of transmissive dielectric metasurfaces, of which there have been many recent examples in the literature [92]–[94], including silicon-based metasurfaces operating in both visible [95], [96] and near infrared wavelength range [97]. As a proof of concept, we initially designed a small volume bottle-beam metasurface with a radius of 10 micron. Our design considers crystalline-silicon nano cylinders on a fused-silica substrate, as shown in Fig. 3.5(b). At the wavelength of 770 nm, crystalline silicon has low loss and silica is transparent, so the transmission of the metasurface can be close to unity. Nano Si cylinders are small local resonators where light is confined with a phase delay before it emerges to free space.

The full-wave simulation of the demo bottle-beam metasurface can be found in Fig. 3.5. We first explored different combinations of the cylinder height, diameter, and the metasurface period. With the refractive index contrast between crystalline silicon ($n_{Si} = 3.7$) and fused silica ($n_{SiO2} = 1.5$), we found the minimum height of $360\ nm$ to cover a full 2π phase delay using pillar diameters ranging from $115{\sim}200\ nm$ and a metasurface period of $330\ nm$. The modulation of the transmitted field by the nanocylinders are shown in [Fig. 3.5 (a)], with the transmitted field larger than $1\ V/m$ due to the refractive index mismatch between the transmitted field media ($n_{air} = 1$) and the simulated light source media ($n_{SiO2} = 1.5$).

The phase profile of the volume bottle-beam metasurface is calculated from a curved beam and then optimized with parametric sweeps, same procedure as what has generated the trap in Fig. 3.4(d). As previously discussed, due to the large memory requirement of full-wave simulations, the radius of the demo metasurface has been reduced from 1 mm to 10 μm, which leads to FoM to drop by ~30% [from 42 in Fig. 3.4(d) to 29 in Fig. 3.5(d)]. The volume trap forms $\sim 15\ \mu m$ away from the demo metasurface, when illuminating with a Gaussian beam which has a 5 μm width.

We also verified our Fresnel diffraction calculation [using Eq. (3.6)] of the field profile [Fig. 3.5 (d)] by comparing to the FDTD results [Fig. 3.5 (c)], and found them to be quite similar. It is expected that the trap calculated with diffraction theory has a slightly higher FoM, since this method assumes zero loss of the metasurface. Based on this demonstration, we assume that the diffraction calculation can be used for analyzing mm-scale metasurfaces.

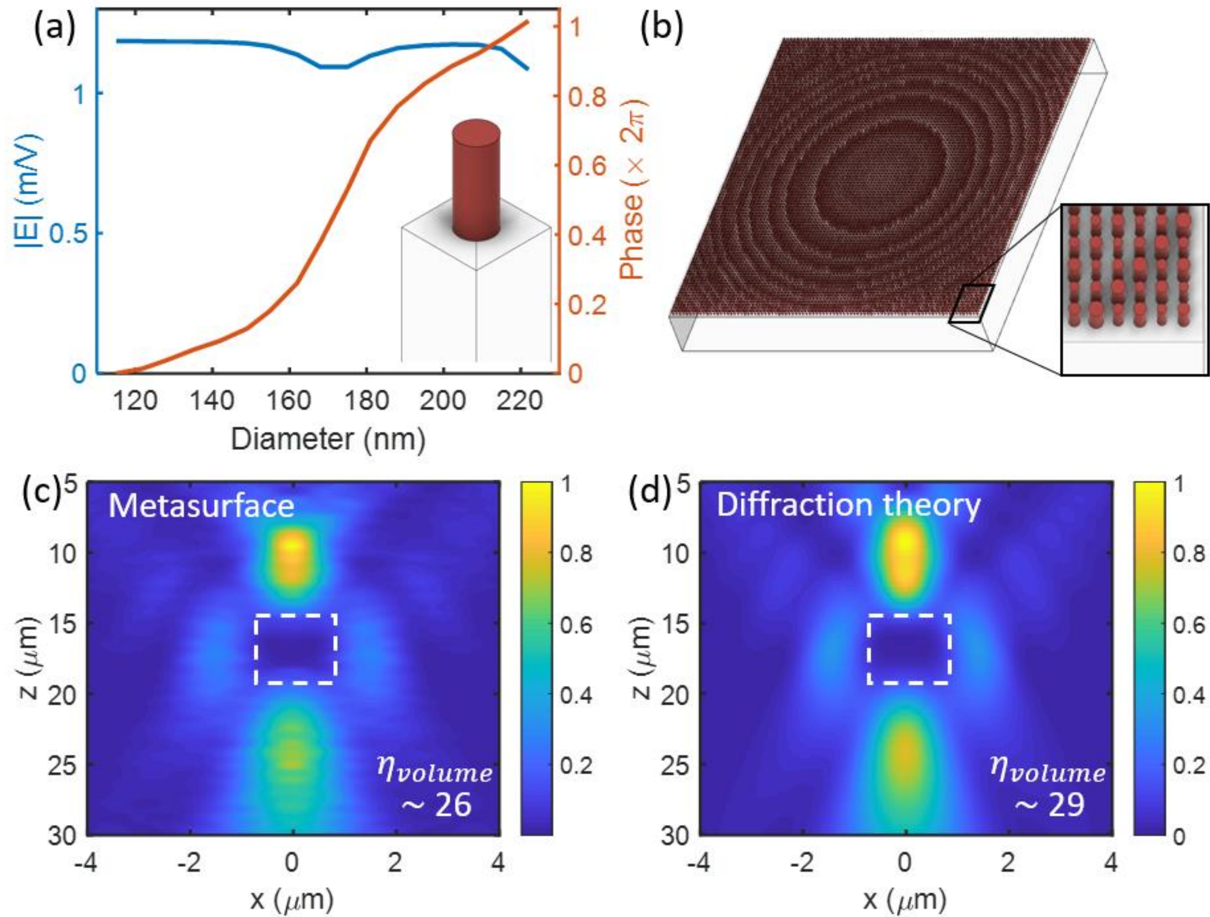

Figure 3.5 (same as Fig. 6 in [76]) Demonstration of a volume bottle-beam trap using a crystalline silicon metasurface. (a) Transmitted field amplitude and phase as a function of the silicon cylinder diameter. The height of the cylinder is 360 nm, with a period of 330 nm, sitting on top of a fused-silica substrate. The source is a plane wave at a free-space wavelength of 770 nm launched from inside the silica substrate. (b) Simulated silicon metasurface. The dimension of the metasurface is 20 µm × 20 µm and the design is radially symmetric. The inset is a portion of the metasurface near its edge. (c) Simulated bottle-beam trap profile using the metasurface in (b) via full 3D FDTD simulation. The metasurface was located at z =0µm and was illuminated with a Gaussian beam of width of 5 µm. The figure of merit (η_{volume}) of the generated bottle-beam trap is 26. (d) Calculated bottle-beam trap using diffraction theory. The incident field at z =0µm is the product of the

transmission phase of the metasurface in (b) and a Gaussian beam of 5 μm wide. This bottle-beam trap has a η_{volume} of 29.

Fabricating bottle-beam metasurfaces

As discussed briefly above, a transmissive dielectric metasurface is composed of (at least) two low-loss materials: a high-index material for making small resonators that impose a phase delay on the transmitting light, and a low-index material as the substrate that not only mechanically supports small resonators, but also forms an index-mismatch interface to confine light in the resonators. A variety of high-index materials have been used to make dielectric metasurfaces have including Si (with refractive index $n \approx 3.7$) [93], [95], [96], TiO_2 ($n \approx 2.5$) [95], [98], GaN ($n \approx 2.4$) [99], [100], and Si_3N_4 ($n \approx 2$) [101], [102]. We picked Si as the high-index material not only because of its index is much higher than others but also due to the fact that silicon has well-established processing recipes (etching, lithography, etc.) given its broad use not only in semiconductor electronics but also on-chip photonics.

Many dielectric metasurfaces have been demonstrate demonstrated on quartz [98], [101], [102] or fused silica ($n \approx 1.5$) substrates [93], [95], and some on sapphire ($n \approx 1.8$) [100]. Comparing to SiO_2 (quartz, fused silica), using Al_2O_3 (sapphire) substrate leads to a slightly worse index contrast, but sapphire is more inert during the etching process.

The selection of different material combinations mentioned above can also affect the fabrication process, such as film growth, etching, charging during e-beam exposure, etc. During my PhD, I explored a number of material combinations and approaches to find at least one that works. Here I will discuss several approaches that we tried but ultimately did not pursue, and also two approaches that are promising and will be used in the future in the group to fabricate completed metasurfaces.

First, we optimized lithography and etching of just a Si wafer without a substrate underneath, since bulky silicon is easy to work with and faster to debug. The results are shown in Fig. 3.6. The silicon substrate is first ultrasonic-cleaned in acetone, IPA, and DI water sequentially, then spin coated with 495K A4 PMMA resist with four test thicknesses range from $150\,nm$ to $260\,nm$. The samples are baked under 180 ℃ for 1 min right after spin coating. The thickness of the resist depends on the spin speed and the amount of solvent. As shown in Fig. 3.6 (a), Si wafers with different resist thickness will have different color due to thin film interference. After spin coating, the resist is exposed with a $30\,\mu m \times 30\mu m$ test pattern [similar to but larger than the one in Fig. 3.5(b)] using electron-beam lithography, here with a dose of $800\,\mu C/cm^2$. The exposed resist is developed in the mixture of MIBK:IPA under room temperature, then baked under 100℃ for 1 min. SEM of the developed resist pattern is shown in Fig. 3.6 (b). The nanocylinder pattern is transferred from the resist to the Si substrate using reactive ion etching (RIE). We have tested four Si-etching recipes included in the 790 etcher at the Wisconsin Centers for Nanoscale Technology (WCNT). All four recipe use a mixture of SF_6 (the etchant) and O_2 (for cleaning) but differ in

mixing ratio, power ($15W$, $25W$, $30W$, $100W$), and chamber pressure. We found the recipe with $67\ sccm$ SF_6, $5\ sccm$ O_2, $100W$ power, and a $15\ mT$ chamber pressure gives a clean etch [Fig 3.6(c) shows the etched Si with the resist mask], while the other three either damage the resist or has contamination over the etched area.

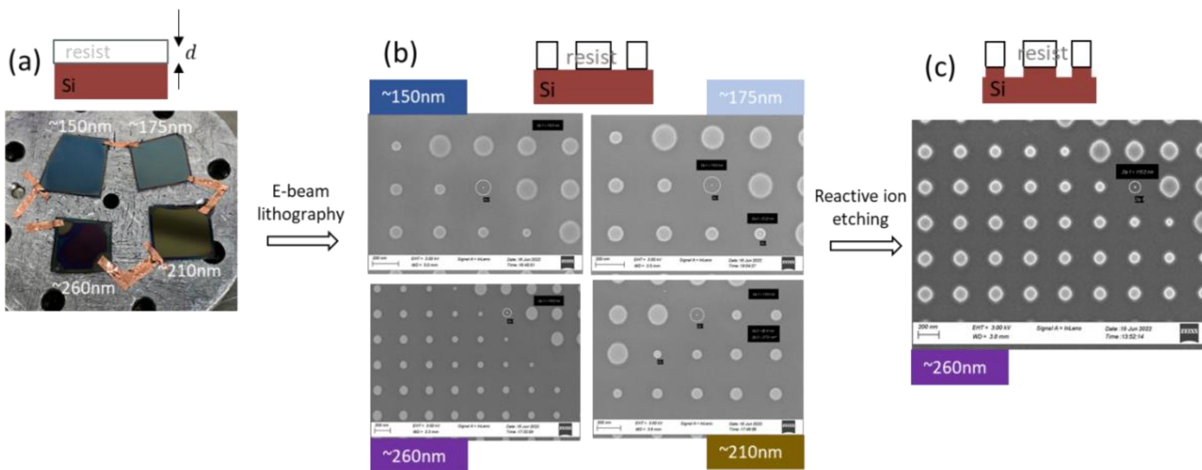

Figure 3.6 Prototyping bottle-beam metasurfaces using bulk silicon substrates. (a) Spin coated PMMA with different thickness on Si substrate. Si samples are coated with PMMA 495K A4 resist under different spin speed of 4000 rpm (150-nm resist), 3000 rpm (175-nm resist), 2000 rpm (210-nm resist), and 1500 rpm (260-nm resist). (b) SEM of four samples in (a) after e-beam expose with a dose of 800 $\mu C/cm$^2. (c) SEM of one sample in (b) after reactive ion etching with a mixture of SF6 and O2 gas under 100W. Nanocylinders are patterned into Si substrate.

Now that the process works on bulk Si, we need to get our Si film or membrane on a transparent substrate like quartz or sapphire, and repeat the fabrication process. The approach we explored first was directly depositing silicon using low-pressure chemical vapor deposition (LPCVD). We were hoping it would be polycrystalline with a small grain size and a low optical loss. During the

LPCVD process, silicon is slowly grown by the reaction of gaseous compounds in high temperature (625 °C) in a low-pressure chamber:

$$SiH_4\ (Silane) \rightarrow\ Si\ +\ 2\ H_2 \qquad \text{Re. (3.13)}$$

We successfully used LPCVD to grow a polycrystalline silicon film on a trial single-crystalline silicon wafer [Fig. 3.7(a)], but unfortunately determined that the films were not of sufficient quality for our application. We imaged the sample with electron microscopy (SEM) and atomic force microscopy (AFM), and found that the grain size is ~200 nm as shown in Fig. 3.7(c). This grain size is right around the size of our nanocylinders, so it is very difficult to etch these films to make high-quality nanocylinders. Our understanding is that both smaller grains and larger grains would likely have worked better.

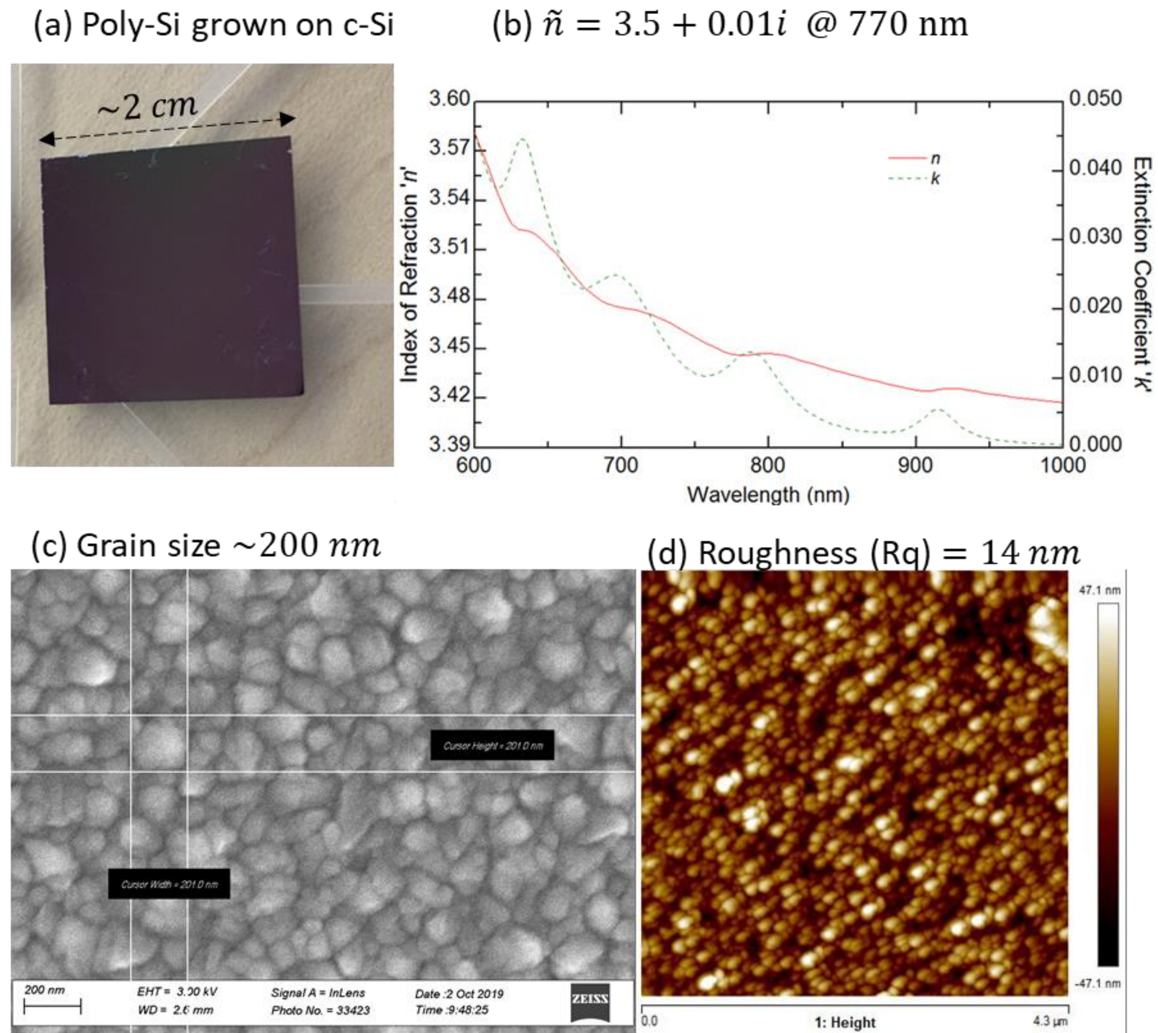

Figure 3.7 The poly-crystalline silicon film grown by LPCVD. (a) The film was grown on a $2\ cm \times 2\ cm$ single-crystalline silicon substrate. Characterization of (a) is shown in (b-d). (b) the refractive index measured by ellipsometry. $\tilde{n} = 3.5 + 0.01i$ at wavelength $\lambda = 770\ nm$, corresponding to a transmission loss of 6% over a $360\ nm$ thick film. (a) An SEM image showing the grain size is around $200\ nm$. (b) An AFM image showing the roughness is $14\ nm$.

Next, we decided to try membrane transfer of single-crystal silicon onto quartz (or any other substrate), which we learned from Prof. Jack Ma's group and from Prof. Victor Brar's group [103],

[104]. During the membrane transfer process, a single-crystalline silicon membrane is stripped off from a silicon-on-insulator (SOI) wafer by etching the middle oxide layer using HF or buffered oxide etchant (BOE). Depends on the size of the membrane to be stripped off, if it is larger than a couple millimeters by side, some small openings need to be patterned on the membrane to assist etching [shown in Fig. 3.8(b)].

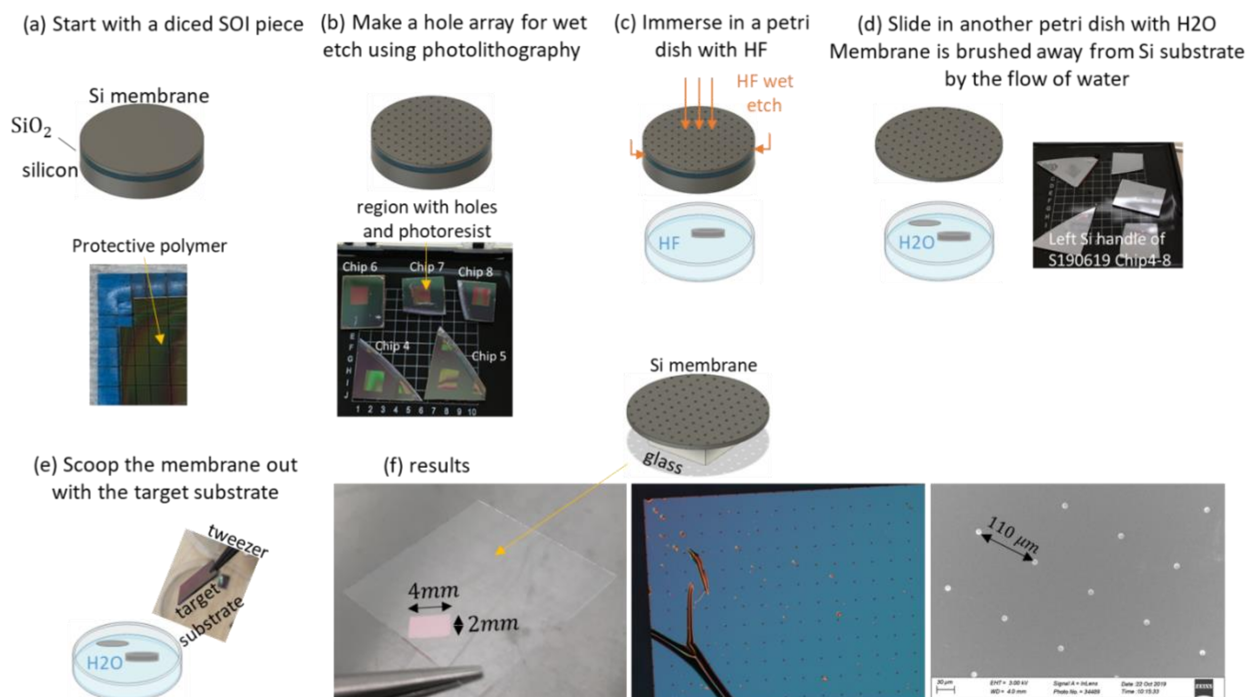

Figure 3.8 Membrane transfer with etching-assisting openings. (a-e) The flow of the membrane transfer process. (f) The transferred membrane sitting on a cover glass. (a) Start with a diced silicon-on-insulator (SOI) wafer piece. (b) Pattern etch-assisting hole openings using photolithography. The holes are separated by $\sim 110\ \mu m$ apart. (c) Immerse the piece in 49% straight HF, which etches most of the $3\mu m$-thick oxide layer within 3min15sec. (d) Gently pick up the etched piece with the loosely attached membrane using a pair of tweezers, then slide the piece into DI water, where the membrane is brushed loose from the Si handle and floats on water surface. (e) Use a pair of tweezers to hold the glass substrate at a corner, then scoop out the

membrane. (f) The scooped-out membrane sits on the glass substrate. Right after the transfer, the membrane-on-substrate sample goes through a spin dry as well as a short baking to enhance adhesion. The microscope and SEM pictures show there is a flat region to work with.

Since now we have a Si membrane on a transparent substrate, we can add e-beam lithography (shown in Fig. 3.9). Note that due to the glass substrate is insulating, a charge dissipation layer is needed before e-beam exposure. We first tried using a silver film, but found the PMMA resist damaged by silver etchant which contains nitric acid. We then switched to using Cr films and found the PMMA resist intact after multiple times of Cr etching. Prior to this fabrication, we have tested 5 nm and 10 nm Cr films on a Si-on-diamond sample for work described in Chapter 4. We found that the sample with 5 nm Cr was still charging up under the electron beam (the sample looked bright and fuzzy under SEM mode), but the sample with 10 nm Cr resolved sub 100 nm features. With the concern that 5 nm may be too thin to form a continuous film, we used 10 nm Cr as the discharging layer for this fabrication as well [such as the 10 nm-thick Cr layer used in Fig. 3.9(a)]. The resist mask after e-beam lithography is shown in Fig. 3.9 (b, d), where the nanocylinders are well defined in the resist. The future fabrication steps for sample in Fig. 3.9 are RIE then removal of the remaining resist using acetone or another solvent-based resist remover.

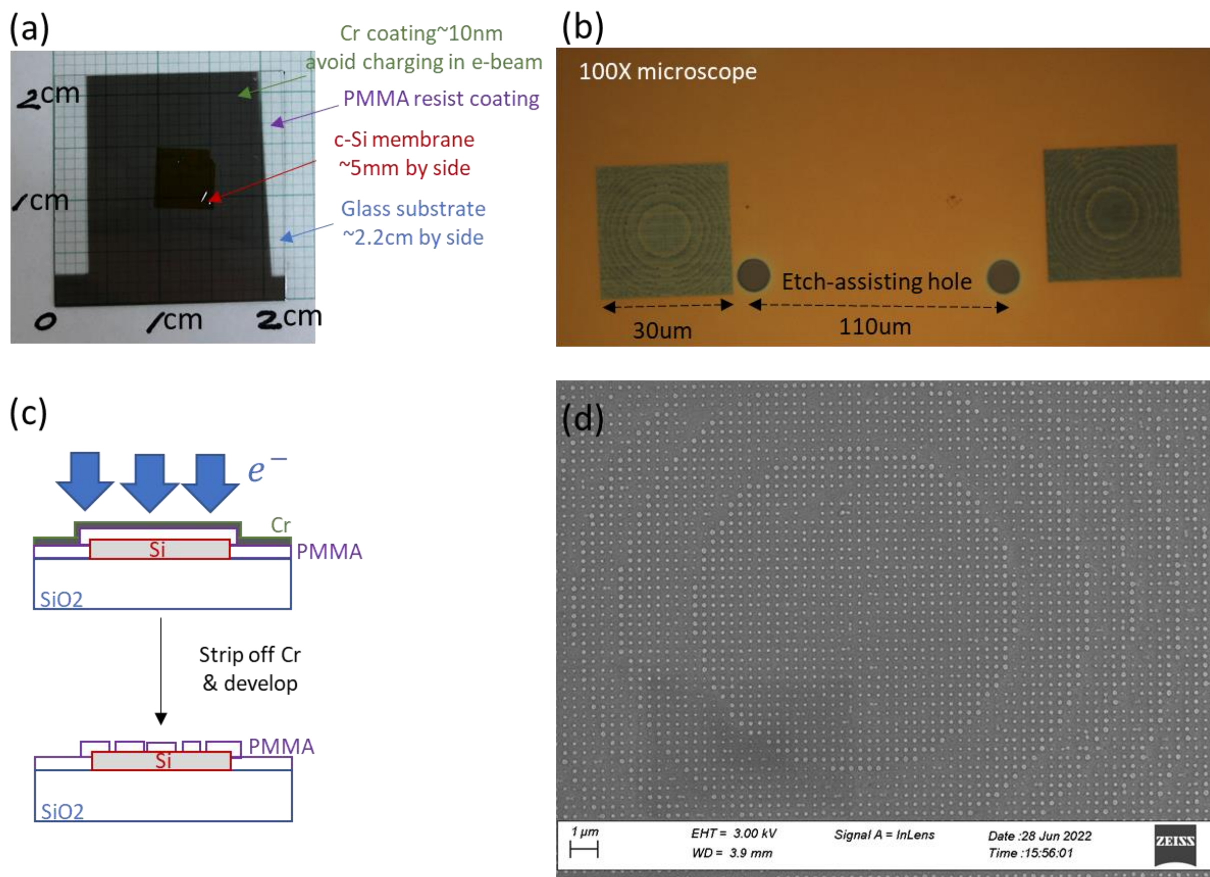

Figure 3.9 E-beam lithography on a transferred Si membrane on glass substrate. (a) Si membrane before e-beam expose is covered by PMMA resist (transparent) and Cr charge dissipation layer (dark gray). Layer structure of (a) is shown in (c), top figure. (b, d) Microscope (b) and SEM image (d) of exposed resist mask. Layer structure of (b, d) is shown in (c), bottom figure.

Besides transferring silicon membrane by ourselves, we recently found a commercial product from Roditi Co. of Si membrane on sapphire substrate. We have characterized this Si membrane using SEM [Fig. 3.11(a)] and an ellipsometer, getting results of a smooth surface and a low-loss refractive index $n = 3.7 + 0.006i$ (Fig. 3.10), which verifies the membrane is single crystalline.

We then proceed with e-beam lithography and etching of this sample, whose SEM images are shown in Fig. 3.11(b) and (d), correspondingly. We found that the nanocylinders are well defined in the resist, whereas they are damaged during the etching. We are now working on debugging the etching process.

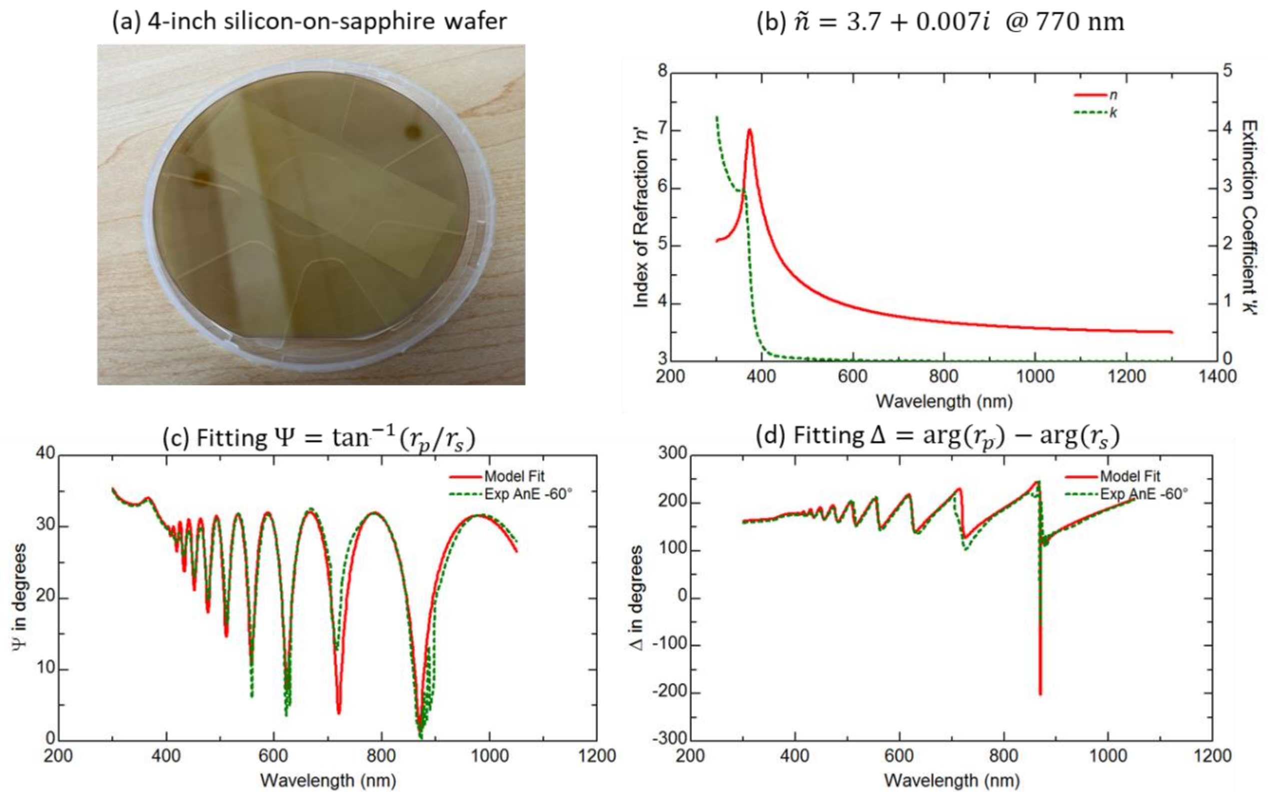

Figure 3.10 Ellipsometry fitting of the refractive index ($\tilde{n}$) of the silicon-on-sapphire wafer. (a) A picture of the wafer. The thickness of the silicon membrane is fitted to be 491 nm (near the center of the wafer) ~ 498 nm (at the edge of the wafer). (b) The fitted refractive index $\tilde{n} = n + ik$. In the wavelength range of 770~797 nm, n drops from 3.71 to 3.68, k drops from 0.0066 to 0.0052. (c-d) Fitted $\Psi = \tan^{-1}(r_p/r_s)$ and $\Delta = \arg(r_p) - \arg(r_s)$, where $r_{p,s}$ is the complex reflective coefficient of p- or s-polarized light [105].

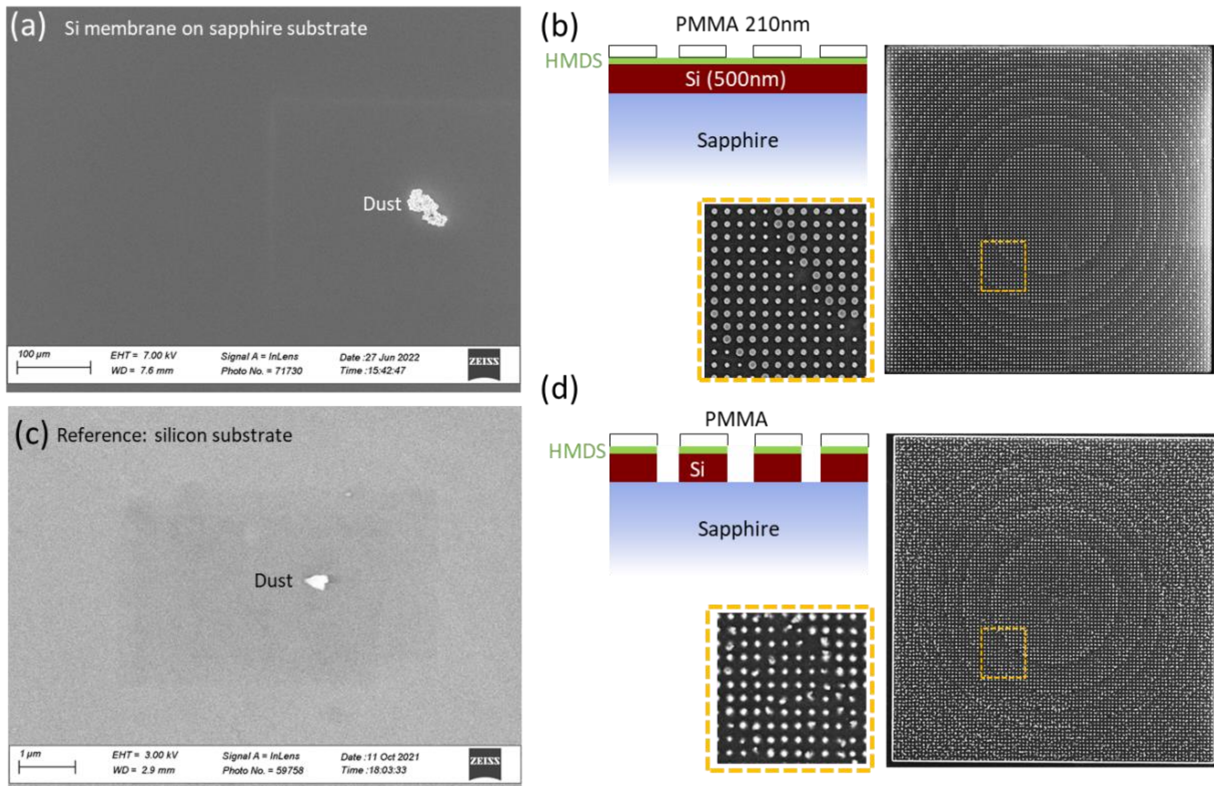

Figure 3.11 E-beam lithography and etching of a Si membrane on a sapphire substrate (SOS). (a) SEM of the smooth surface of the Si membrane, similar to the surface SEM of a Si substrate in (c). We have characterized the Si membrane in (a) using an ellipsometer, and the fitted refractive index is n=3.7+0.006i. (b) SEM of the resist mask after e-beam lithography. Nanocylinders are well defined in the resist. (d) SEM of the patterned silicon membrane with resist mask after reactive ion etching. Nanocylinders in (d) are damaged, an issue we are working on now.

Summary and future work

In conclusion, we discussed optical metasurfaces for efficiently generating bottle-beam traps. We introduced figures of merit to evaluate the performance of optical bottle beams for trapping atoms and small particles. The FoM describes the trapping efficiency with a given incident power. We designed dielectric metasurfaces that create bottle-beam traps when illuminated by a Gaussian beam. Our design is based on silicon nanocylinders on a transparent low-index substrate and is optimized to power-efficient compared to other methods of generating bottle beams. We are now in the process of fabricating the designed bottle-beam metasurfaces. We have explored multiple material combinations and fabrication approaches, and have zeroed in on two promising candidates using transferred Si membranes on glass substrates or commercial Si membranes on sapphire substrate. After we find a good etching recipe that can transfer nanocylinder patterns from the resist to the silicon membrane, we will be ready for optical measurement of the generated bottle-beam trap and subsequent atom trapping experiments.

.

Adjoint-optimized structures for extracting fluorescence from color centers in diamond

The design approach described in this chapter has been previously published as R. A. Wambold, Z. Yu, et. al., “Adjoint-optimized nanoscale light extractor for nitrogen-vacancy centers in diamond,” *Nanophotonics* (2021) [106]. The computation work was led by Ray Wambold, with contributions from me. The fabrication work was led by me, with contributions from Minjeong Kim.

Quantum sensors based on color centers in diamond

Color centers are fluorescent point defects that naturally exist in diamond and can also be created using ion implantation and annealing [107]–[109]. A nitrogen-vacancy (NV) center, for example, is formed by replacing a carbon atom with a nitrogen atom and an empty neighboring spot (i.e., vacancy) in the diamond crystal lattice [Fig. 4.1(a)].

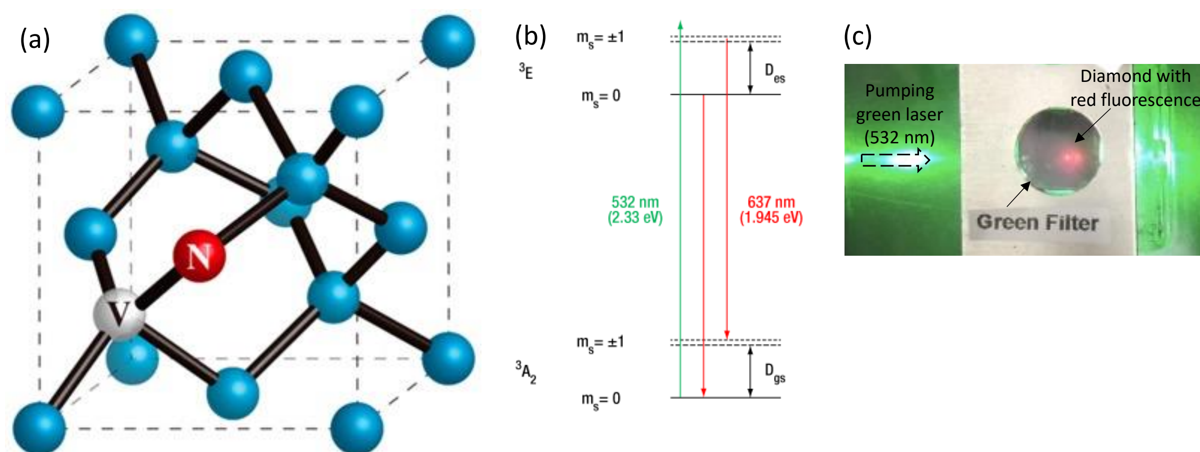

Figure 4.1. Nitrogen-Vacancy (NV) centers in diamond. (a) The ball-and-stick schematic of an NV center in diamond, which consists of a substitutional nitrogen atom (red), a missing atom (i.e., an atomic vacancy, white) in the diamond crystal lattice of carbon atoms (blue). NVs in [100] diamond can be oriented in one of four directions along the ⟨111⟩ crystal axes (black sticks) which is 54.7° with respect to the surface normal. (b) The energy level diagram of a NV^- center in zero magnetic field. The NV^- can be pumped from the ground state ($^3A_2$) to excited (^3E) state by an off-resonance excitation (e.g., using a 532-nm green laser). The energy difference between the two states is 1.945 eV (or 637 nm, red arrows). (c) A picture of a bulk diamond (transparent) illuminated by a 532-nm green laser, which emits red fluorescence. A green filter is inserted on top of the diamond to block the green background for a better observation of the fluorescence. Source: (a) [110], (b) thorlabs.com.

NV centers are atom-like quantum systems which have atom-scale size, different spin states, and different charge states. Negative charged NV centers (NV^-) are exploited in most studies due to their observed optical and spin resonances [111], [112], which had been elusive for their neutral counterpart (NV^0) because of strain broadening [113]. NV^0 can be converted to NV^- by applying an electric voltage [114], [115], oxidation [116], [117], or surface termination [118].

The energy level diagram of NV^- is shown in Fig. 4.1(b). The NV^- color centers can be excited using off-resonance light (e.g., a 532-nm green light) and emit red fluorescence [Fig. 4.1(c)]. Note that although the optical transition for NV^- (zero phonon line, or ZPL) is at $637\ nm$, at room temperature the fluorescence emission is broadened by vibrational side bands in the diamond with width $> 150nm$. In this work we consider the $635 \sim 800\ nm$ range to cover both the ZPL and phonon sidebands [Fig. 4.4(b)].

Compared to neutral atoms which need to be cooled and trapped, color centers can operate at room temperature and are mechanically fixed inside the diamond lattice. Along with neutral atoms, trapped ions, Josephson junctions, and others, NV centers are considered to be a major research platform for quantum technologies such as quantum computing [119] and quantum communication [120] [121]. Furthermore, due to the sensitivity of the quantum states of NVs to their environment, they can be used as nano sensors for magnetic fields [122], [123], electric fields [124], temperature [125], [126], and the presence of chemical/biological molecules [127], [128].

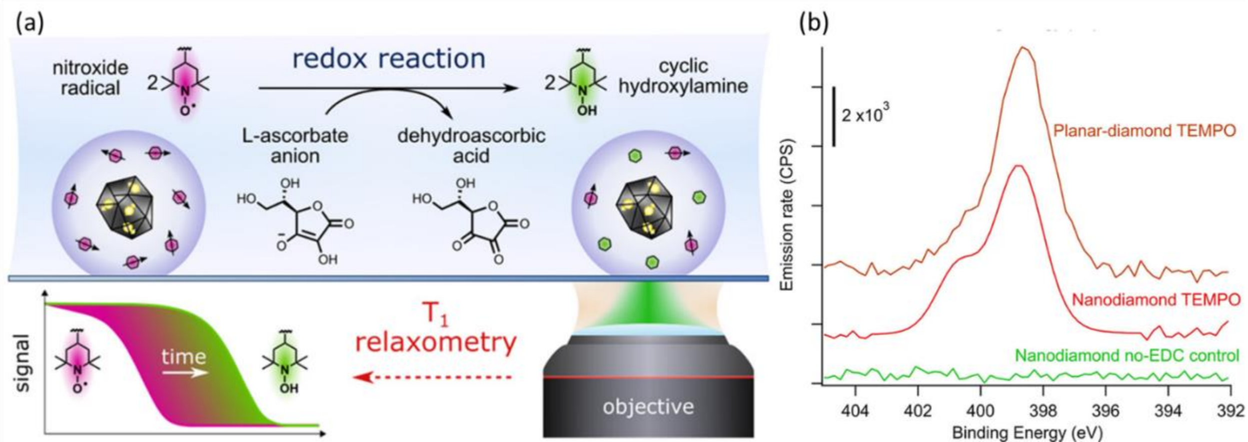

Figure 4.2. Chemical sensing using NV centers in diamond. (a) Sensing the reduction of nitroxide radicals with nanodiamonds. The nitroxide radicals are attached to TEMPO-based spin probes coated around the nanodiamonds. During the process of redox reaction, the number of attached nitroxide radicals decreases, causing the measured T_1 spin relaxation time of the NV centers to increase. The TEMPO-based spin probes used in (a) can also be grafted to bulk diamond, which is more reproducible, easier to process, and of higher quality [127]. A recent study [129] has shown that TEMPO probes grafted to bulk diamond have a higher density than those to nanodiamonds, as indicated by the higher N(1s) peak in XPS analysis in (b). Source: (a) [128], (b) [129].

However, it is challenging to read out the fluorescence signal from diamond due to large reflection and total internal reflection beyond the critical angle caused by diamond's high refractive index (~2.4), as illustrated in Fig. 4.3(a). Previous efforts to enhance light extraction from bulk diamond usually include etching into the diamond (which degrades quantum properties such as spin coherence time) [130]–[132], or require oil immersion for a high numerical aperture (NA) collecting objective (which can be detrimental to live-cell sensing applications) [133], [134]. The next section describes our effort of enhancing fluorescence extraction from NV centers in diamond by adding a silicon nanoscale structure on top of the un-etched flat diamond surface, as illustrated by Fig. 4.3(b). Broadband simulations show that by adding such a silicon nano light extractor, the collected fluorescence can be enhanced by up 35 times and directed into a 60° collecting cone for easy measurement with low-NA optics. Although the effect of the presence of the nano light extractor to the spin characteristics (coherence) of the NV is unknown (also difficult to predict and

needs future experimental investigation), it is likely to be less invasive than etching into the diamond which inevitably introduce defects and damage.

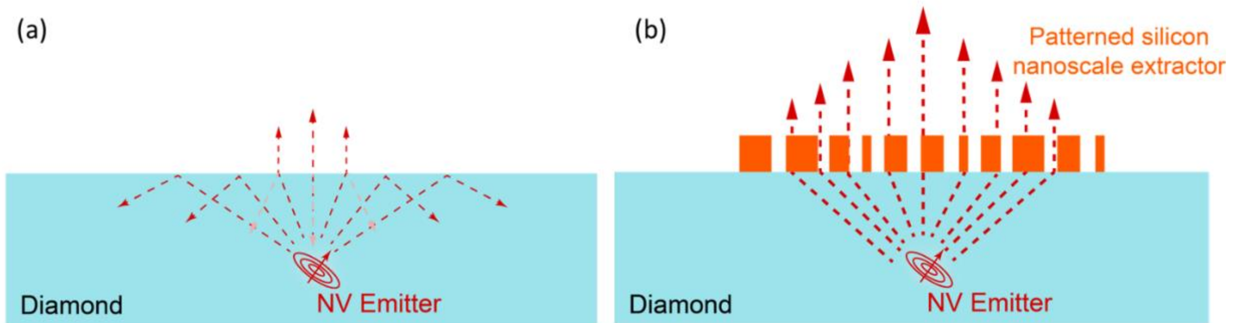

Figure 4.3. Cartoons showing (a) high reflection of NV emission at the diamond-air interface, and (b) enhanced transmission of NV emission to free space after adding the silicon nano light extractor.

Designing silicon nano light extractors using adjoint optimization

To evaluate the performance of a nano light extractor extract (NLE), we define its figure of merit (FoM) to be the spectrum-averaged extraction efficiency, as shown in Fig. 4.4:

$$FoM = \frac{\int I_{NV}(\lambda) \cdot \eta(\lambda)\, d\lambda}{\int I_{NV}(\lambda)\, d\lambda}, \quad \text{Eq. (4.1)}$$

where λ is the wavelength, $I_{NV}(\lambda)$ is the broadband emission spectrum of NV^- taken from [135], $\eta(\lambda)$ is the extraction efficiency as the number of photons emitted into free space in the presence of a nano light extractor (NLE) dived by the number of photons emitted by the same light source with no NLE. This FoM is defined for enhancing broadband fluorescence, which is particularly useful for sensing applications using shallow NVs, but the design approach can be applied to different figures of merit for narrower wavelength range or just a single wavelength (e.g., around the ZPL).

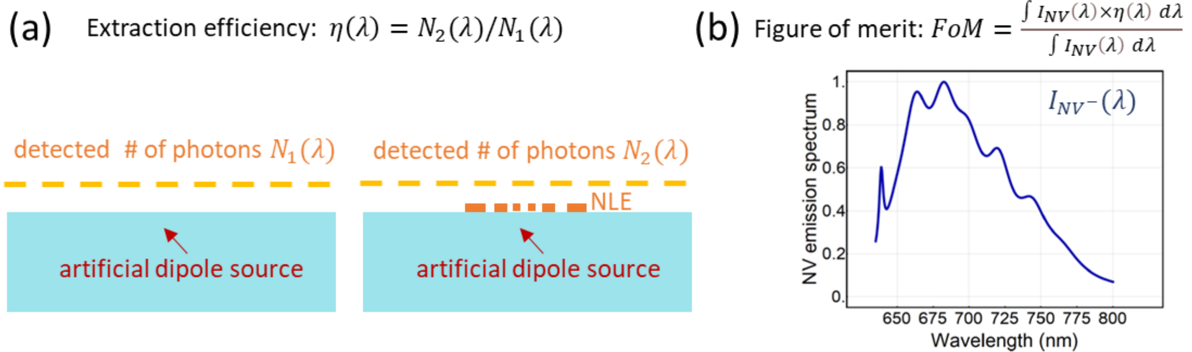

Figure 4.4. Figure of merit (FoM) for broadband NV emission extraction. (a) The extraction efficiency (η) for a single wavelength (λ) is defined as the number of photons emitted into free space in the presence of a nano light extractor (NLE) dived by the number of photons emitted by the same monochromatic light source with no NLE. (b) The broadband emission spectrum of NV^- taken from [135]. With a broadband light source, the FoM is defined as the weighted average of the extraction efficiency $\eta(\lambda)$ by the emission spectrum $I(\lambda)$.

To optimize the performance of the nano light extractor, we used the adjoint-optimization method [136], [137]. This method can be used to improve any design to a local optimum step by step, where at each optimization step two electromagnetic simulations are performed, and the result is used to determine how to change the structure to increase the FoM. One simulation, called the "forward simulation", calculates the emission field from an NV center [$E_{fwd}(\boldsymbol{r},\lambda)$], where $\boldsymbol{r}$ is the position vector of a point inside the nano light extractor [Fig. 4.5(a)]. Another simulation, called the "adjoint simulation", calculates the back propagation of the desired emission field toward the nano light extractor structure; in this work, we set the adjoint source to be a Gaussian beam with a 30° diffraction angle [$E_{adj}(\boldsymbol{r},\lambda)$ in Fig. 4.5(b)]. If the nano light extractor is described by its position-dependent refractive index profile [$n(\boldsymbol{r},\lambda)$], then the adjoint-optimization method tells us that the FoM will be improved by increasing the refractive index [$n(\boldsymbol{r},\lambda)$] at points where the overlap between the forward field and the adjoint field is positive (i.e., $Re\big[E_{fwd}(\boldsymbol{r},\lambda)\cdot$

$E_{adj}(\boldsymbol{r},\lambda)\big] > 0$) [138]. In other words, the figure-of-merit gradient $G(\boldsymbol{r},\lambda)$ satisfies:

$$G(\boldsymbol{r},\lambda) \propto n(\boldsymbol{r},\lambda) \cdot Re\big[E_{fwd}(\boldsymbol{r},\lambda) \cdot E_{adj}(\boldsymbol{r},\lambda)\big] \qquad \text{Eq. (4.2)}$$

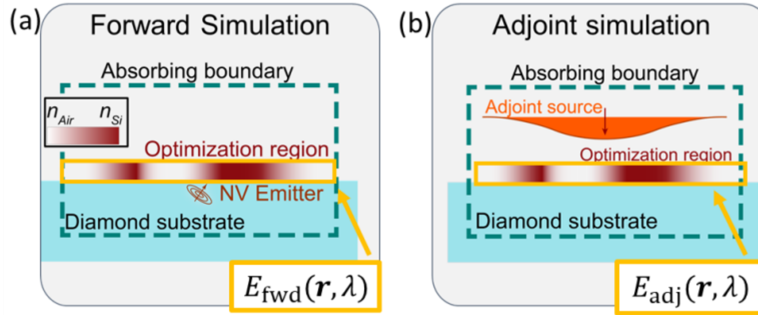

Figure 4.5. Schematics showing the forward and adjoint simulations for improving the extraction efficiency using the adjoint-optimization method. (a) A forward simulation calculates emitted field from an NV center inside the NLE [$E_{fwd}(\boldsymbol{r},\lambda)$, where $\boldsymbol{r}$ is the position vector]. (b) An adjoint simulation calculates the back propagation of the desired emission field, which we set to be a Gaussian beam with a 30° diffraction angle, into the nano light extractor [$E_{adj}(\boldsymbol{r},\lambda)$]. Based on ref. [138], the gradient of the FoM is $G(\boldsymbol{r},\lambda) \propto n(\boldsymbol{r},\lambda) \cdot Re\big[E_{fwd}(\boldsymbol{r},\lambda) \cdot E_{adj}(\boldsymbol{r},\lambda)\big]$.

When setting up forward simulations, one technical subtlety is to decide the orientation of the dipole source to mimic NV emitters. Since for shallow NVs in diamond at room temperature, the emission comes from dipoles on the plane perpendicular to the NV axis and is unpolarized [139], [140], we can pick any two orthogonal dipoles and average over them incoherently. We picked one dipole parallel to the surface [pointing out of the screen in Fig. 4.6(b)], and another angled 35.3° with the normal vector of the surface [in screen in Fig. 4.6(c)]. Then we took the average of the figure-of-merit gradient calculated from simulations with these two dipoles:

$$G(\boldsymbol{r},\ \lambda) = \frac{[G_{pair\ 1}(\boldsymbol{r},\lambda)+G_{pair\ 2}(\boldsymbol{r},\lambda)]}{2}, \qquad \text{Eq. (4.3)}$$

The gradient in Eq. 4.3 is further averaged over the NV emission spectrum:

$$G(\boldsymbol{r}) = \frac{1}{\Delta\lambda}\int I_{NV}(\lambda) \cdot G(\boldsymbol{r},\lambda)\, d\lambda \qquad \text{Eq. (4.4)}$$

Note that because only one NV orientation out of the four orientations in [100] diamond is considered, here in practice prior characterization of a sample with NVs is needed to align the NLE properly during the fabrication process. Such characterization has been demonstrated in [141]. Furthermore, because the phase delay that the NLE imparts does not affect its performance, we have simulated multiple adjoint sources with different phases of 0~2π in step of π/2 and only kept the simulation which yields the highest FoM.

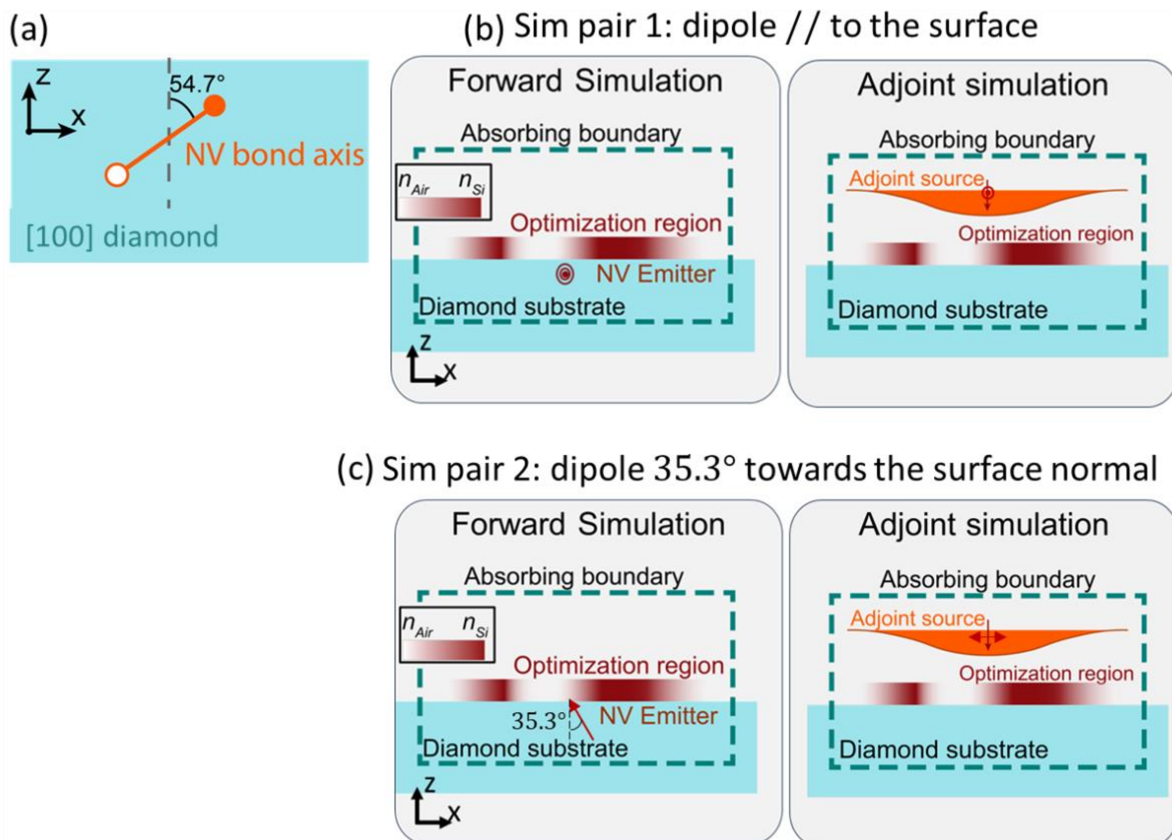

Figure 4.6. Orientation of dipole sources to mimic NV centers in [100] diamond. (a) NV bond axis is 54.7° towards the surface normal [the 3D structure can be found in Fig. 4.1(a)]. Because NV emission is incoherent and unpolarized at room temperature, we can pick any two orthogonal dipole orientations [140]. We used two pairs of forward/adjoint simulations for these two

orientations: (b) shows the dipole orientation parallel to the surface (along the y axis), with emission field also polarized in y, indicated in the adjoint Gaussian source; (c) shows the dipole oriented in the xz plane $35.3°$ towards z, with the adjoint Gaussian source polarized in x.

Another technical subtlety worth mentioning is when treating the refractive index profile $n(\boldsymbol{r}, \lambda)$. Although the physical structure is binary with either $n = n_{Si}$ or $n = n_{air}$ at a point $\boldsymbol{r}$, for optimization we need to implement an artificial intermediate material whose index can change continuously. Therefore, we used a mixing function $p(\boldsymbol{r})$ which varies from $0 \sim 1$, and the continuous refractive index is:

$$n(\boldsymbol{r}, \lambda) = p(\boldsymbol{r}) \times n_{Si}(\lambda) + [1 - p(\boldsymbol{r})] \times n_{air}(\lambda), \quad \text{Eq. (4.5)}$$

where $p = 1$ means silicon, $p = 0$ means air. The mixing function $p(\boldsymbol{r})$ is gradually binarized during the optimization process by performing a binary push repetitively (with the binarization method used in [142], [143]), and the optimization only stops until a binary structure that can be fabricated is achieved.

We also implemented several additional steps that yield a structure that can be fabricated. For example, in simple lithography processes, we can only make vertically invariant structures, which here we enforce by setting the index in a single column along z axis to be constant: $n(\boldsymbol{r}, \lambda) = n(x, y, \lambda)$. This is equivalent to setting the mixing function $p(\boldsymbol{r}) = p(x, y)$. The gradient function also needs to be averaged along z by:

$$G(x, y) = \frac{1}{\Delta z} \int G(\boldsymbol{r}) dz \quad \text{Eq. (4.6)}$$

We also implemented a step that limits the resolution of the resulting structure, because lithography

processes have limited resolution. This was done by applying a blurring function (proposed in [142]) to the refractive index profile, so that the index at each point [at position (x, y)] is adjusted based on the index of the neighboring points [at position (x', y')]:

$$p_{\text{blur}}(x, y) = \frac{\iint w(x, y, x', y') \cdot p(x'y')\, dx'dy'}{\iint w(x, y, x', y')\, dx'dy'} \qquad \text{Eq. (4.7)}$$

$$w(x, y, x', y') = \begin{cases} 0, & d > R \\ R - d, & d \le R \end{cases} \qquad \text{Eq. (4.8))}$$

where $w(x, y, x', y')$ is a linear weight function that becomes larger with a closer distance $d = \sqrt{(x - x')^2 + (y - y')^2}$, and we picked the proximity threshold to be $R = 40\, nm$, which is a resolution achievable using conventional electron beam lithography.

The third fabrication limitation is the sample-to-sample variation of the optimal dose, which can lead to pattern dilation or erosion (from, for example, the underdose or overdose of a positive resist, correspondingly). The pattern dilation (or erosion) can be implemented during the binary push process discussed previously, by setting a higher (or lower) threshold for a mixing factor to be pushed to air ($p = 0$). Note that since our NLE is designed for broadband extraction enhancement with $> 150\, nm$ wavelength span, thus it is inherently less sensitive to a slightly dilated /eroded structure compared to those designed for a narrower bandwidth or a single wavelength. The correspondence between broadband performance and shape robustness can be understood by considering scale invariance of Maxwell's equations with a fixed l/λ, where l is the structure length. Shape robustness has been observed in broadband photonic structures such as those in [144], [145]. Therefore, we did not include the test of a diluted or eroded NLE in the repetitive

optimization process, instead we only tested such fabrication error for the final optimized structure [Fig. 4.10].

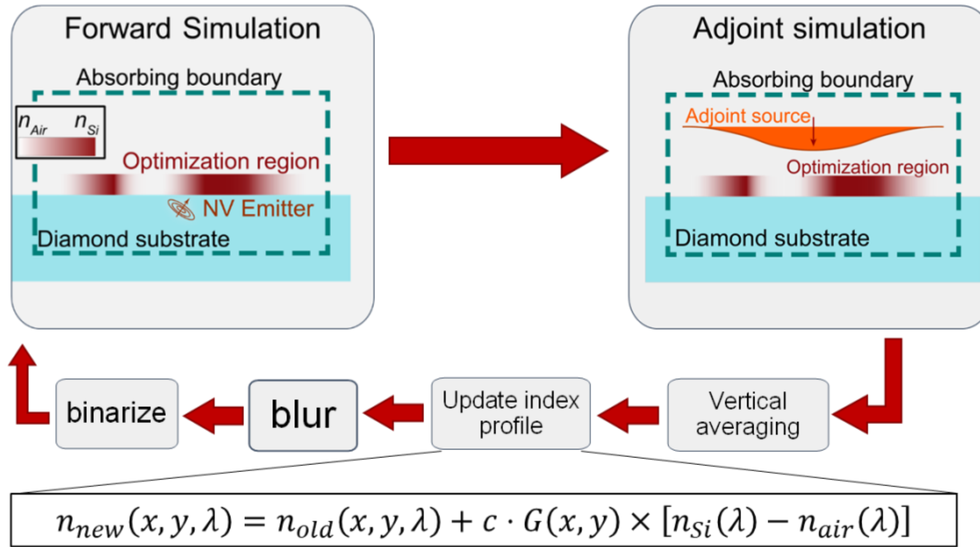

Figure 4.7. Flow of the adjoint optimization. The figure of merit (FoM) of the NLE is improved by evolving the index profile of the NLE (n) in the direction of the gradient (G), which is calculated by Eq. 4.2 using the electric field from both forward and adjoint simulation sets. c is a normalization factor. Besides updating the index profile, several fabrication constraints are applied, including vertical invariance [$n(\boldsymbol{r}, \lambda) = n(x, y, \lambda)$, Eq. 4.6], finite-resolution blurring (Eq. 4.7-8), and binarization.

The fabrication constraints are integrated into the optimization flow as shown in Fig. 4.7, where the index profile is updated based on the figure-of-merit gradient:

$$n_{new}(x, y, \lambda) = n_{old}(x, y, \lambda) + c \cdot G(x, y) \times [n_{Si}(\lambda) - n_{air}(\lambda)], \qquad \text{Eq. (4.9))}$$

where c is a normalization factor, gradient G is calculated based on Eq. 4.2-4, using the electric field in both forward and adjoint simulation. The light field is simulated used the finite-difference time-domain (FDTD) method, implemented in commercial software Lumerical FDTD, with

absorbing boundary conditions.

We first ran a couple of optimizations for various structure thicknesses using two-dimensional (2D) FDTD simulations, which can be done much faster compared to three-dimensional (3D) simulations. In the 2D simulations, we have translational invariance along one axis (e.g., the y axis in Fig. 4.6), so the dipole source is actually a line source. Nevertheless, the 2D simulations can tell us some useful information about what type of NLE will be successful in the 3D case. The structure thickness ranges from $50\ nm$ to $600\ nm$ in steps of $50\ nm$. Simulations of different structure thickness use the same NVs with $10\ nm$ depth and two dipole orientations, and is optimized five times with different initial random structures. The averaged FoM is shown in Fig. 4.8, which has a Fabry-Perot-like dependence over the structure thickness (i.e., the FoM oscillates with increasing thickness of the NLE). We picked the thickness which yields the highest FoM $(300\ nm)$ and ran a further optimization with 3D simulations.

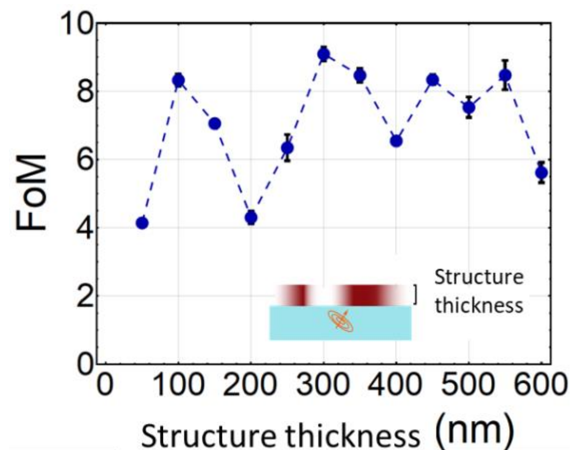

Figure 4.8. Optimized FoM with different structure thicknesses, simulated using 2D FDTD.

The evolution of FoM during the 3D optimization process is shown in Fig. 4.9(a), reaching a final $FoM = 35$ with the NLE structure shown in Fig. 4.9(b). Note that the FoM includes both Purcell enhancement (~3) and collection improvement (~12). The extraction efficiency [$\eta(\lambda)$] is shown in Fig. 4.9(c), as well as the efficiency with different NV depths. Although the NLE is optimized for $10\ nm$ deep NV, shallower NVs yield higher FoM, presumably due to increased coupling with the NLE, which leads to a larger Purcell enhancement [146]. The FoM will drop to half for a $40\ nm$ deep NV, and further to $FoM{\sim}3$ for a $300\ nm$ deep NV [106]. The far field radiation and near field profile at $\lambda = 675\,nm$ are shown in Fig. 4.9 (d-e). Similar field properties (intensity/profile) are observed for other wavelengths (shown in the supplementary of [106]). The near field profile [Fig. 4.9 (e)] shows the NLE shapes the dipole emission pattern of the NV into a Gaussian beam which propagates into a $\pm 30°$ cone in the far field [Fig. 4.9(d)] and can be collected with low-numerical-aperture optics.

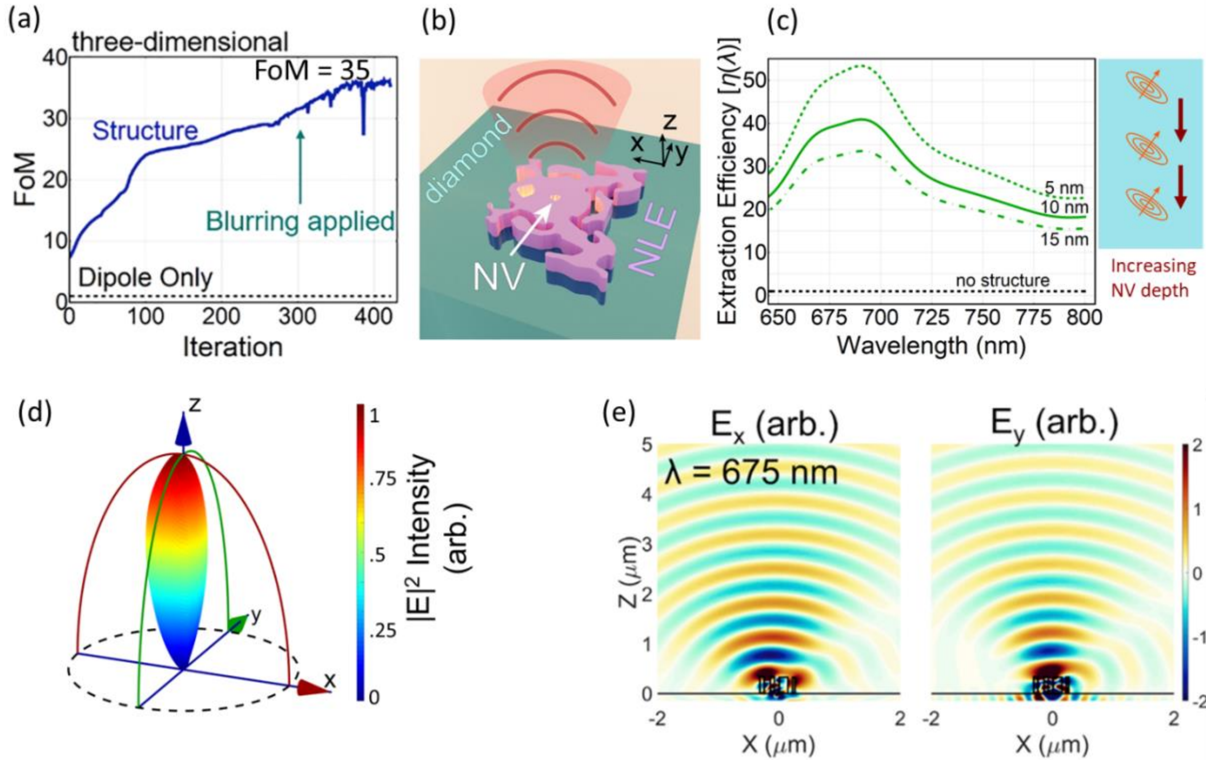

Figure 4.9. An adjoint-optimized silicon-based nano light extractor (NLE). (a) The improvement of FoM during the optimization process, reaching the final $FoM = 35$. (b) The 3D rendering of the optimized NLE, whose extraction efficiency is shown in (c). Although the NLE is optimized for a $10\ nm$ deep NV, a shallower NV gives a higher extraction efficiency for the NLE due to a stronger Purcell enhancement [146]. The extracted field in free space has a far field radiation and near field profile shown in (d-e) for $\lambda = 675\ nm$. Source: (a) Fig. 2(c), (b) Fig. 1, (c-e) Fig. 3(b-d) of [106].

We have also tested the robustness of the optimized NLE over fabrication or alignment error, which is shown in Fig. 4.10. We found that FoM remains similar for an NLE (1) diluted/eroded by $\pm 20\ nm$ from the optimized structure, (2) offset from NV center by $\pm 30\ nm$ in x or $\pm 40\ nm$ in y, or (3) misaligned by $\pm 20°$.

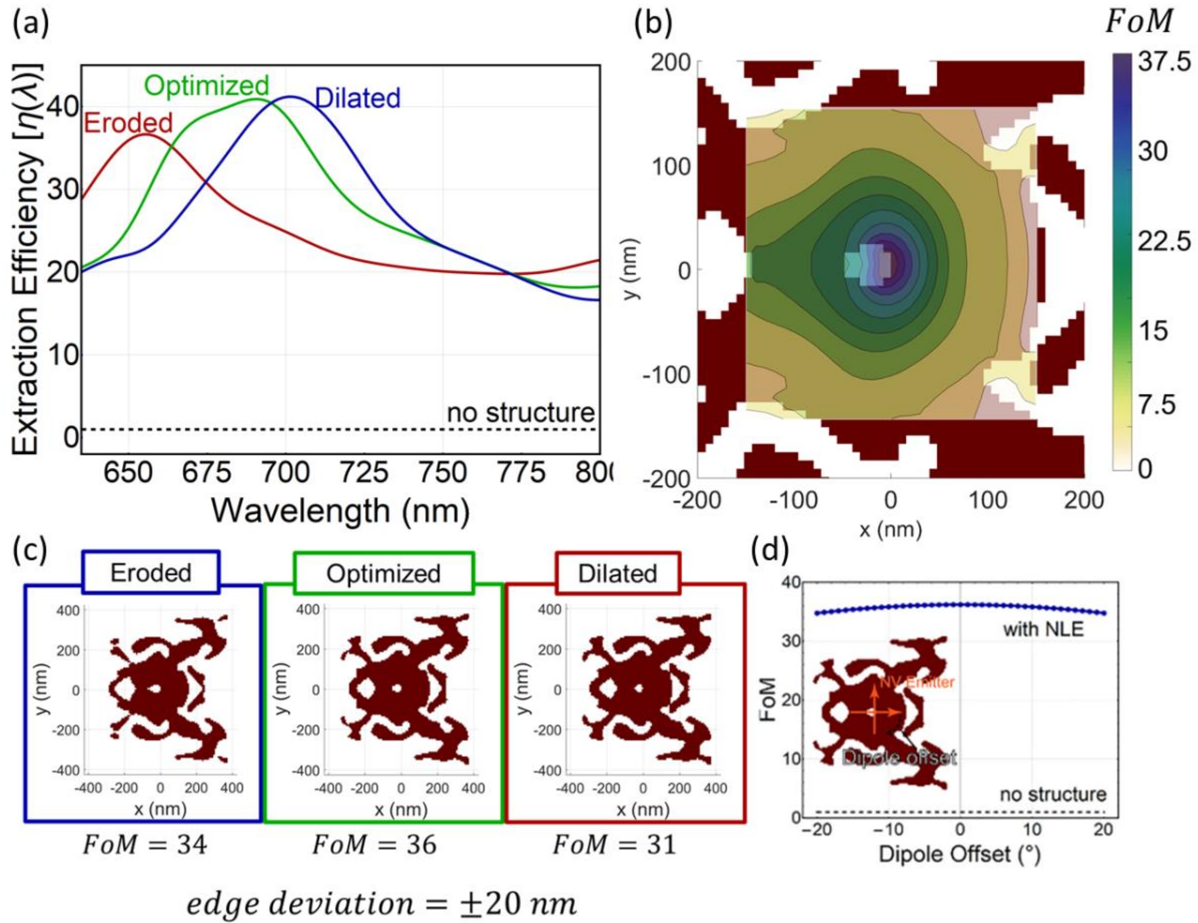

Figure 4.10. Robustness of the optimized NLE over fabrication or alignment errors. (a) Demonstration of the fabrication robustness of the optimized device for an NV depth of 10 nm. Eroded and dilated structures [shown as left and right figure in (c)] are based on the optimized structure with edge deviation of ±20 nm. (b, d) FoM of a misplaced (b) or misaligned (d) NLE in reference to the NV center. (b) Tolerance of the NLE to lateral offsets of the NV center. The FoM remains above 25 for x offsets of ±30 nm and y offsets of ±40 nm. (d) FoM dependence on the NV emitter angle emulating angular alignment errors of the NLE. Source: adapted from Fig. 4 in [106].

Fabricating silicon nano light extractors on diamond

Without focusing on details at first, our fabrication process for NLEs on diamond involves transferring a silicon membrane onto a polished bulk diamond with shallow NV centers, electron-beam lithography to define the structure, and etching of the silicon with a selective etch recipe that

does not etch into the diamond (Fig. 4.11). As we will see later in this section, this process requires several improvements to fabricate an NLE with sufficient quality.

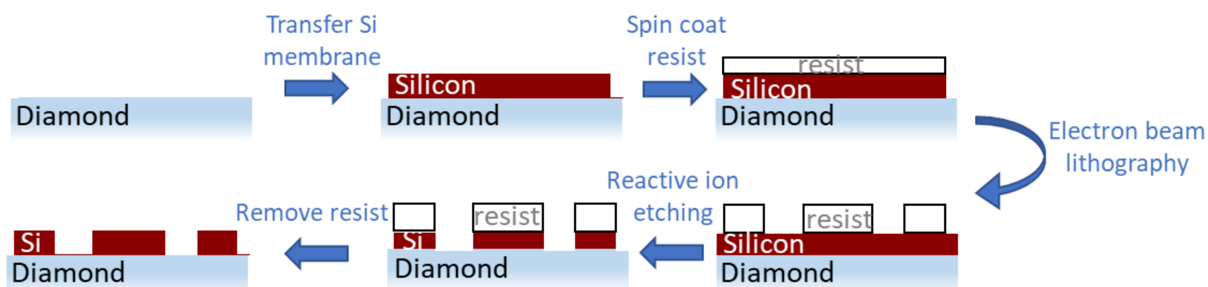

Fig. 4.11 The flow of the fabrication. A silicon membrane is first transferred to the diamond substrate. Then a resist layer is spin coated on top. The pattern is defined on the resist by e-beam lithography. Then the pattern is transferred to the silicon membrane by directional etching. Finally, the resist layer is stripped off.

We first need to transfer a silicon membrane to diamond substrate (with a technique used in [103], [104]). Due to material availability, we purchased a silicon-on-insulator (SOI) wafer whose device layer is $220\ nm$ [Fig. 4.12(a)], and re-designed the NLE with the new structure thickness [the new NLE is shown in Fig. 4.12(b)]. 220 nm is a standard SOI thickness due to its use in silicon photonics [147]–[150]. The new $220\ nm$ thick NLE has a lower $FoM{\sim}10$ compared to the 300-nm-thick NLE. The extraction efficiency of the new NLE with different NV depth is shown in Fig. 4.12(c). Nevertheless, this is still significant improvement over the case with no structure and, once we demonstrate that this approach works, we can consider ordering custom 300-nm-thick SOI wafers and repeat the process with those.

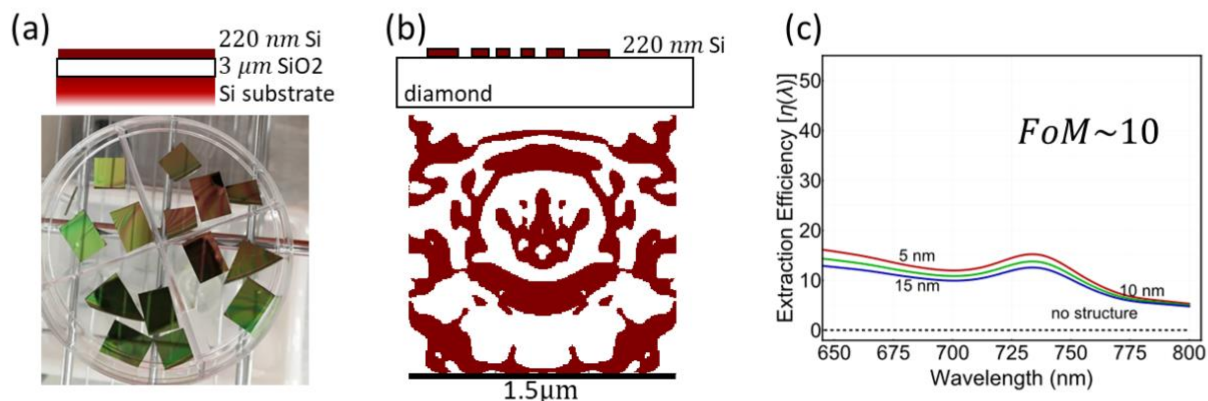

Figure 4.12 Nano light extractor with $220\ nm$ thickness. (a) Diced SOI wafer pieces which have a $220\ nm$ silicon membrane. The layer structure is shown on top. (b) Index profile of the redesigned $220\ nm$ thick NLE, with red representing n_{Si} and white representing n_{air}. Top figure shows the side view. (c) The extraction efficiency of the $220\ nm$ thick NLE, which has a $FOM{\sim}10$.

We first prototyped the e-beam lithography and etching process using a single-crystalline Si wafer, because this results in the most-favorable conditions for the fabrication process (no charging during electron-beam lithography, pristine silicon surface, etc.). The fabrication was all done at the Wisconsin Centers for Nanoscale Technology (WCNT). We used a 100 keV electron-beam lithography system (Elionix) and poly(methyl methacrylate) (PMMA) resist, which is a conventional positive-tone e-beam resist. Following a dose test to determine the optimal e-beam dose, we performed a silicon etch test using reactive ion etching (RIE).

There are many RIE etching recipes to etch silicon, but we needed to select a process that will not damage the diamond once all of the silicon is etched away. In principle, we could use an etch stop layer between the diamond and the silicon, but we decided to look for a recipe that does not require the etch stop so that spin probes can be grafted directly on the diamond surface for sensing applications [Fig. 4.2]. Therefore, a silicon etchant that does not react with diamond is preferred. We selected pure CF4 recipes since it is reported to either not etch diamond [46], or etch at a very

slow rate (0.01 μm/hr, [47]).

During our initial fabrication tests with this recipe, we saw repeated defects on the resulting sample [Fig. 4.13 (a)]. To try to diagnose this, I tried to use other Si etching recipes in the same etcher, and the defects persisted in all of these. Ultimately, I determined that the defects were a result of a process called "micromasking" [151], [152], where contamination in the etching chamber masks the etching at random points, resulting in rough features. The contamination ended up being Al particles that resulted from ion bombardment of the Al holder (cathode) in the tool. Finally, after switching to graphite cathode, we were able to achieve a etch [Fig. 4.13 (b-c)].

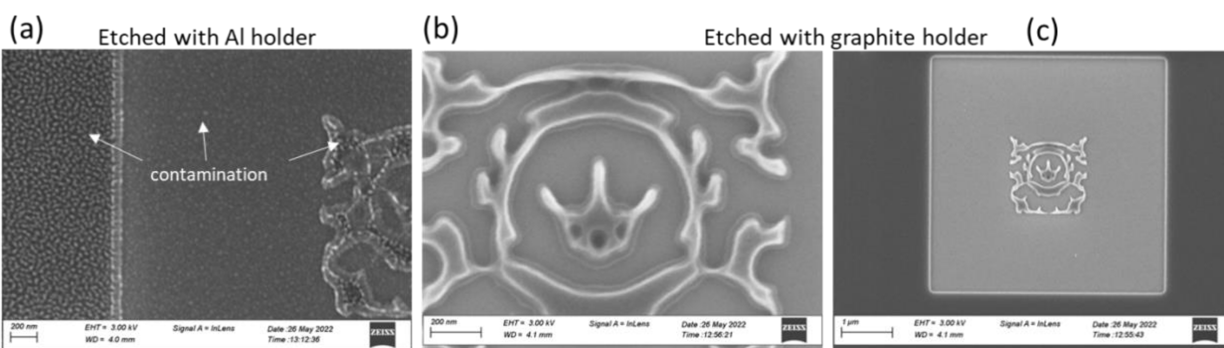

Figure 4.13 Contamination issue during reactive ion etching with an aluminum holder. Two samples in (a-c) have a PMMA resist mask from the same e-beam lithography process. The sample in (a) is etched while placed on top of an Al holder, while the sample in (b-c) on a graphite holder. Both samples went through the same RIE recipe in pure CF_4 under 100W power. Contamination only happens when using Al holder, probably due to "micromasking", where Al particles are throwed everywhere from ion bombardment.

In Fig. 4.13 (b-c), the etch depth was <100 nm, which is not sufficient to get through our 220 nm Si. Unfortunately, simply increasing the etch time did not result in a successful device, because the CF_4 etch has very poor selectivity against 495K A4 PMMA resist mask we used (selectivity worse than 1:3, i.e., pure CF_4 etches PMMA 3~4 times faster than Si, which I determined by

etching large areas half-covered with resist, stripping the resist, and then using a contact profilometer to measure the resulting etch depth). At the lowest spin speed in the recommended range of the spin curve ($1500\,rpm$), the PMMA thickness is $\sim 250\,nm$. Therefore, we either needed thicker resist (which may reduce the lithography resolution or otherwise change the process), or use a hard mask in between PMMA and Si. We decided on the latter approach.

Our hard-mask process with 20 nm of Cr is shown in Fig. Fig. 4.14. In addition to serving as a hard mask, the Cr also provides a conductive layer for charges deposited during e-beam lithography. We characterized the selectivity of the etch to Si vs Cr to be >9:1, by first sputtering Cr on a Si wafer partially covered with Kapton tape, peeling off, etching, and then using the contact profilometer to measure the resulting step. We did not determine the selectivity precisely, but know that it is more than sufficient for our process.

To create the Cr hard mask, we need to deposit Cr everywhere on our sample, spin PMMA, write the pattern with e-beam lithography, and then etch the Cr. Therefore, we need a Cr-etching recipe with which PMMA mask can survive until Cr is fully etched. The selectivity of Cr against PMMA can be increased by using more Cl_2 and less O_2 during the etching. We adapted an ICP-RIE recipe that we found no the website of the UCSB nanofabrication facility, with 26 sccm Cl_2, 4 sccm O_2, 10 mTorr pressure, 400W ICP power, 50W RIE power. We further optimized the Cr etching time, which is a tradeoff between the under etch of small openings and the over etch of the big openings, as illustrated in Fig. 4.14.

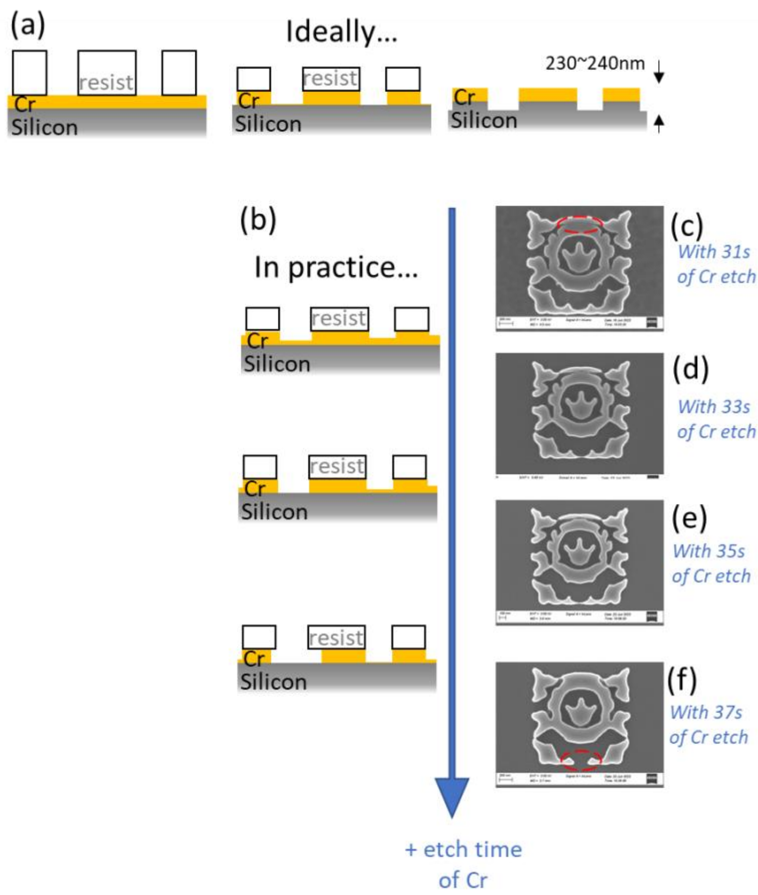

Figure 4.14 Optimizing the Cr etching time. (a) shows the ideal etching process, where all openings are well etched. (b) showing the practical etching process, where the smaller openings are etched slower than the bigger openings, and we need to tradeoff between the under etch of the small openings [such as the defect in the red circle of (c)] and the over etch of the big openings [such as the defect in the red circle of (f)]. (c-f) SEM of samples with increasing Cr etching times. We picked the optimized Cr etching time of 35s [as used in (e)].

After optimizing the Cr etch time, we summarized the fabrication flow in Fig. 4. 14. The sample was first evaporated with Cr of 20-nm thick as a hard mask. Then PMMA 495K A4 was spin coated on top under the speed of 4000 rpm for 1 min. Resist was baked at 180C for 1 min. The resist thickness will be around 145nm measured using thin film reflectometer for a larger test sample coated with the same recipe. Then the resist was exposed under 100kV voltage and 1nA current using Elionix G-100. The SEM resolution under this writing condition is 20 nm of a gold

reference. After exposing, the sample was developed in a mixed developer with 1 volume of MIBK and 3 volumes of IPA for 1 min under room temperature. Then we baked it under 100℃ for 1 min.

After e-beam lithography, the pattern was transferred from PMMA resist to Cr hard mask by dry etching Cr with Plasma-Therm ICP-RIE metal etcher for 35s. The pattern was then transferred to silicon membrane by reactive ion etching with pure CF4 recipe, 100W power and 10 mTorr pressure. The sample was etched for 20min during which Cr hard mask has survived but PMMA on top was fully etched away. The Cr hard mask was then stripped off by wet etching.

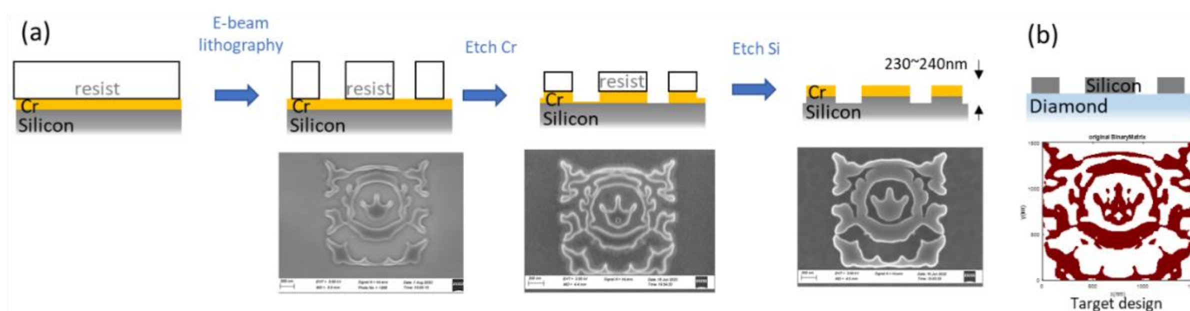

Figure 4.15 Fabrication process flow using a silicon wafer for prototyping. (a) Schematic showing each step during the e-beam and etching process, with the underneath SEMs taken of a sample in that step. The last step of stripping off Cr is omitted. (b) As a reference, showing the target structure: a patterned silicon membrane on a diamond substrate.

After developed recipes on silicon substrates, we moved on to fabricate on diamond. The first step is to transfer a single-crystal silicon membrane to the diamond substrate, a technique we learned from Jack Ma's group and Victor Brar's group. The transfer process is shown in Fig. 4.16. The silicon membrane was stripped off from a Si-on-insulator (SOI) wafer. We first diced the SOI wafer into pieces with both length and width less than 2 mm to ensure fit on a 3 mm-side square diamond chip. Then an SOI piece was immersed in a mixed etchant with 1 volume of HF and 1 volume of 20:1 buffered oxide etchant (BOE). After 17 hours, the detached membrane was

scooped out and moved to 6:1 BOE. The second etching was terminated after 3.5 hours by scooping out the membrane and moved to deionized water. The membrane was further moved to IPA for transferring. By holding and slightly tilting the diamond chip with a pair of tweezers, the membrane was gently scooped out on top of diamond with a puddle of IPA. Then we laid diamond on a cleanroom wipe which soaked some IPA out, we further blow dried the sample with N2 gun. Right after that, the sample was baked on a hot plate under 90℃ for 10 min to enhance adhesion. Then we did rapid thermal annealing (RTA) ramping up to 350℃ and stayed for 5 min with the hope that the adhesion will be further improved.

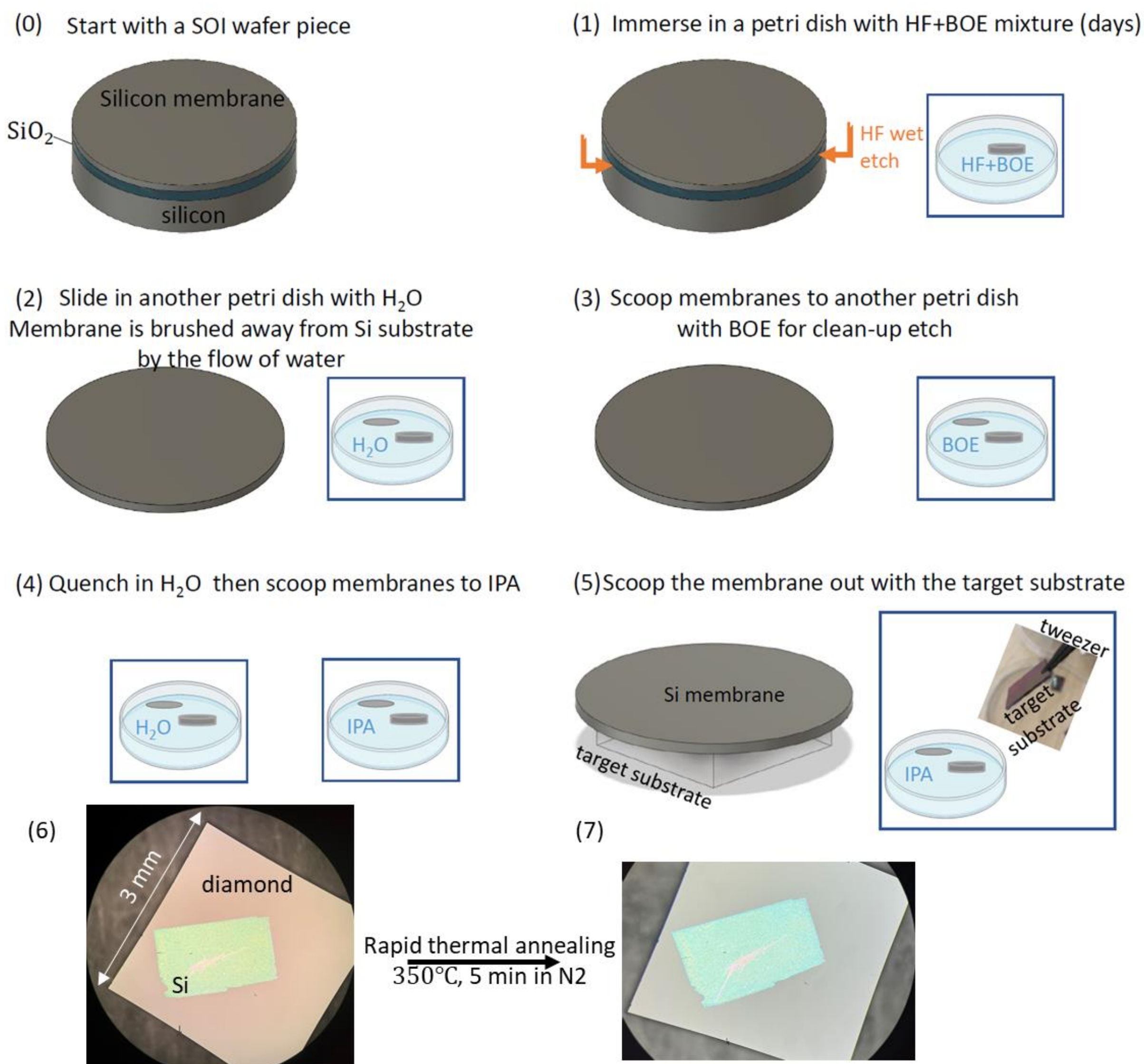

Figure 4.16 The membrane transfer process. (0) start with an SOI wafer with the desired membrane thickness. (1) immerse the SOI piece in HF + BOE mixture, where the oxide layer is mostly etched. (2) slide the etched SOI piece into water, where the loosely attached membrane is brushed away by liquid. (3) Use a spoon to scoop out the membrane and move to a weaker etchant for cleanup. (4) Terminate the cleanup etch by moving the membrane to water then to IPA. (5) Use a pair of tweezers to hold the diamond substrate, then scoop the membrane on top of diamond. (6) microscope of the transferred silicon membrane on diamond substrate after gently blow dry. (7) Rapid thermal annealed sample to enhance the adhesion between the membrane and the diamond.

With a transferred silicon membrane on a diamond substrate, we repeated the e-beam lithography and etching process which we optimized on Si substrate (Fig. 4.14-15), and finally obtained the

silicon nano light extractor on diamond, as shown in Fig. 4.17(b-c).

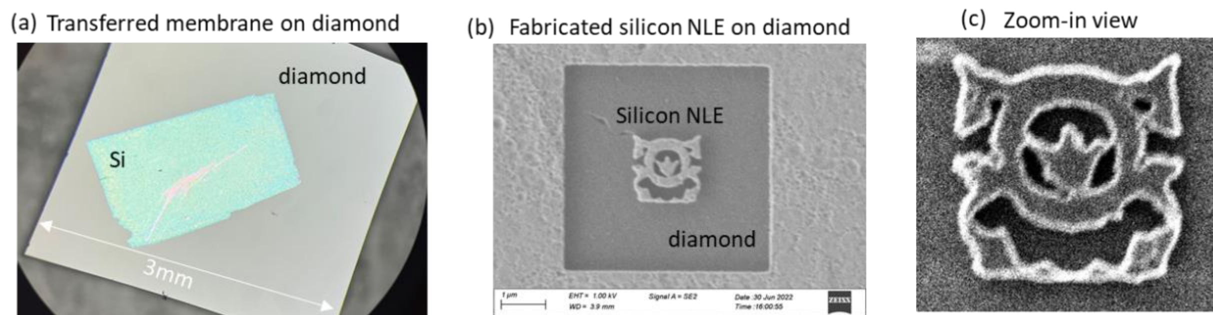

Figure 4.17 Fabricated silicon nano light extractor on diamond. (a) The silicon membrane under microscope before e-beam lithography and etching. (b-c) SEMs of the fabricated silicon nano light extractor (NLE) on diamond. The fabrication process is the same as shown in Fig. 4.14~4.15 using silicon substrate. The resolution of the fabricated NLE on diamond is $\sim 50\ nm$, which we are currently working on improving with cold developing.

The process was successful in transferring the pattern into a Si membrane on diamond, though the final resolution shown in (c) not ideal. At the same time, the diamond appears to be untouched by the etching, which was a significant goal of this fabrication process. Some future work will be needed to optimize the resolution of the fabricated NLE (currently no better than 50 nm) and then perform the outcoupling experiments with NV centers described earlier in this chapter. We have already identified a route to improving the resolution, successfully replicating features down to 10 nm using a process known as cold development, where the development of the e-beam resist is performed at temperatures around 10 degrees C using a weaker developer (7 volumes of IPA : 3 volumes of water) inside a week sonicator bath [153]–[155] (Fig. 4.18). This work will be carried on by others in the group after my departure.

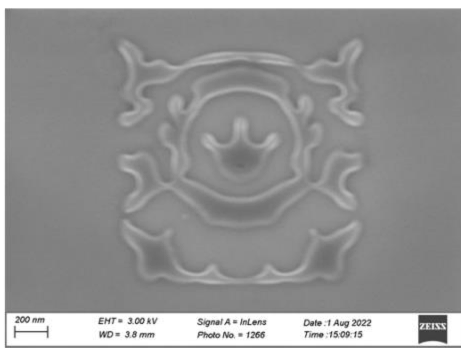

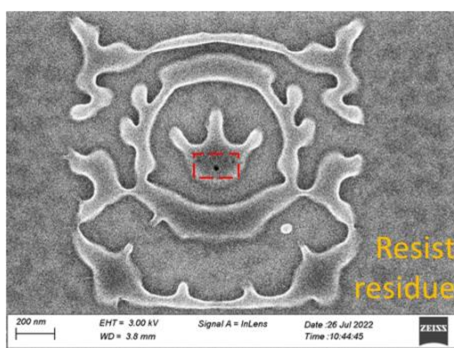

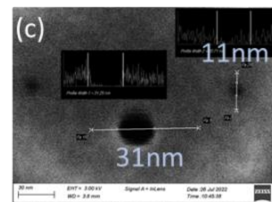

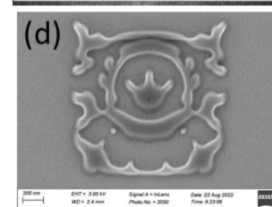

Figure 4.18: Resolution improvement with cold development. (a-d): patterned PMMA on Si substrate. (a): PMMA developed under room temperature (~18℃) with a mixture of MIBK:IPA = 1:3 for 1min has a resolution of ~30nm. (b-d): PMMA developed under reduced temperature with a weaker resist (a mixture of IPA:H_2O = 7:3) and inside a weak sonicator bath. Pattern in (b) was developed around 0℃ for 2min, the resolution drops to ~10nm as shown in the zoom-in image of the red boxed region in (c). (b) is underdeveloped with resist residue in the exposed region shown as dark speckles around the pattern. The residue can be cleaned using longer development time and/or higher development temperature as shown in (d), which was developed at 9℃ for 3min, and has comparable resolution with (b).

Appendices

FDTD simulation results of checkboard gratings with gold coating

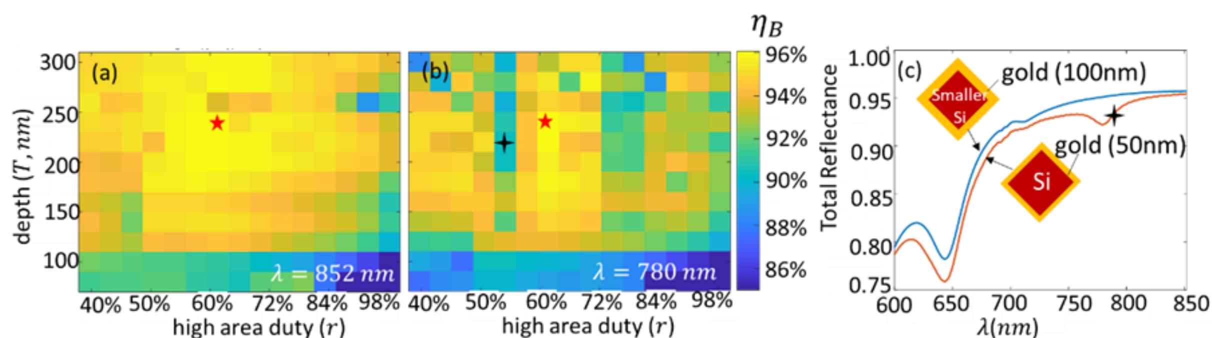

Figure A1.1 (a, b) Finite-difference time-domain (FDTD) simulations of the balancing efficiency η_B for gold-coated 2D checkboard grating chips. The incident beam is modeled as a plane wave with a wavelength of (a) 852 nm and (b) 780 nm. One unit cell is simulated, with periodic boundary conditions. The structure is a patterned silicon substrate (pitch d =978 nm, depth T =250nm)

coated with gold that has thickness of 50 nm. η_B is calculated using Eqn. (1). (c) Comparison of the total reflectance of a simulated structure in (b, black cross) and the structure with the same duty cycle but a thicker gold layer (100 nm). The dip in reflectance at λ near 780 nm disappears for the larger gold thickness, which indicates that the feature is due to coupling to a surface-plasmon polariton (SPP) at the gold-silicon interface.

Measured and simulated diffraction efficiencies for circular grating chips

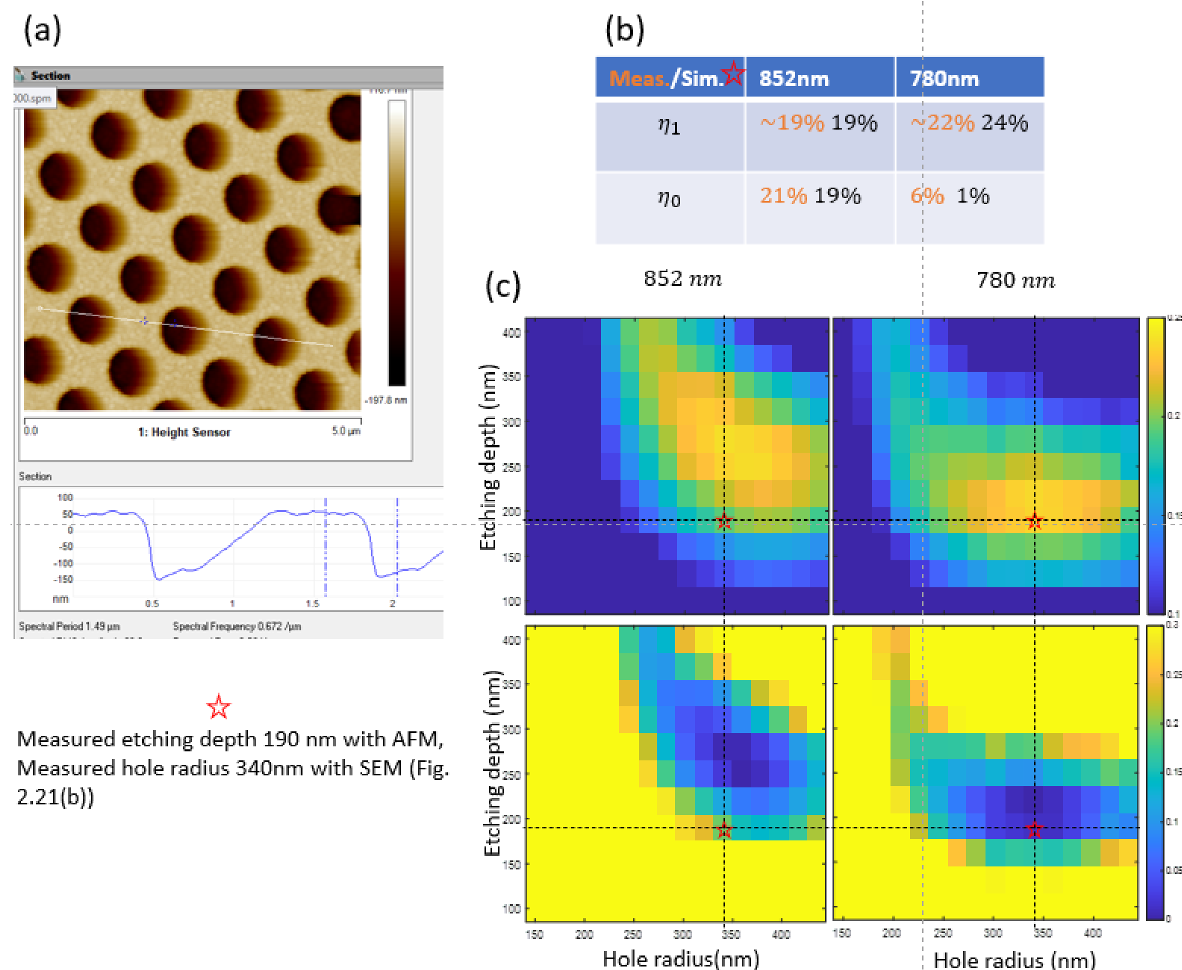

Meas./Sim.☆	852nm	780nm
η_1	~19% 19%	~22% 24%
η_0	21% 19%	6% 1%

Fig. A2.1 (a) AFM of the fabricated circular grating, which shows a patterning depth of 190 nm. (b) The comparison of the measured and the simulated diffraction efficiency of the 1st order (η_1) and the 0th order (η_0). The simulated structure is represented as red star in (c), with a patterning depth of 190nm and a hole radius of 340nm. (c) Simulated diffraction efficiencies for different circular gratings at two trapping wavelengths.

Derivation of the dipole force and the scattering force

Let us derive both the dipole force and the scattering force on an atom in a radiation field. An external electric field $\vec{E}$ induces a shift of the electric cloud of an atom $\vec{r}$. The induced dipole moment $\vec{p}$ is given by

$$\vec{p} = -e\vec{r} = \epsilon_0 \kappa_a \vec{E}, \quad \text{Eq. (A3.1)}$$

where $\epsilon_0 \kappa_a$ is the polarizability of the atom. The interaction energy between the dipole and the electric field is given by

$$U = -\frac{1}{2}\vec{p} \cdot \vec{E} = -\frac{1}{2}\epsilon_0 \kappa_a E^2 \quad \text{Eq. (A3.2)}$$

The z-component of force is given by

$$F_z = -\frac{\partial U}{\partial z} = -\frac{1}{2}\vec{p} \cdot \vec{E} = \epsilon_0 \kappa_a E \frac{\partial E}{\partial z}, \quad \text{Eq. (A3.3)}$$

and similar for F_x, F_y. Without loss of generality, let us assume a radiation field (light) with angular frequency ω propagates along z and is polarized along x, then the electric field can be written as:

$$\vec{E} = E_0 \cos(\omega t - kz)\, \widehat{e_x}, \quad \text{Eq. (A3.4)}$$

By substituting $\vec{E}$ in Eq. (A3.3), and replacing the term $\epsilon_0 \kappa_a E$ with the induced dipole (in x direction) as $-ex$ based on Eq. (A3.1), we obtain the force along light-propagation direction:

$$F_z = -ex[\frac{\partial E_0}{\partial z} \cdot \cos(\omega t - kz) + kE_0 \sin(\omega t - kz)] \quad \text{Eq. (A3.5)}$$

Based on Chap. 7 of ref [75], the atom with its electron e^- undergoes a harmonic oscillation in an oscillating electric field, with displacement x can be decomposed into two components: one in phase with the external field (denoted as u), and the other $\frac{\pi}{2}$ phase shifted from the external field

(denoted as v). Using classical mechanics (corrected result using quantum mechanics will be discussed later), the displacement can be written as:

$$x \triangleq u \cdot \cos(\omega t - kz) - v \cdot \sin(\omega t - kz),$$

$$u = \frac{-\delta}{\delta^2 + \frac{\beta^2}{4}} \cdot \frac{F}{2m\omega}, \;\; v = \frac{-\beta/2}{\delta^2 + \frac{\beta^2}{4}} \cdot \frac{F}{2m\omega}, \qquad \text{Eq. (A3.6)}$$

where Coulomb force $F = -eE_0$ and $\beta = \Gamma(1 + 2\Omega^2/\Gamma^2)$ is the broadened linewidth due to radiation power.

By substituting x in Eq. (A3.5), we have

$$F_z = -e[u \cdot \frac{\partial E_0}{\partial z} \cdot \cos^2(\omega t - kz) - v \cdot kE_0 \sin^2(\omega t - kz) + (uE_0 k - v\frac{\partial E_0}{\partial z}) \cdot \cos(\omega t - kz)\sin(\omega t - kz)] \qquad \text{Eq. (A3.7)}$$

The time averaged force over many oscillation periods is

$$< F_z > = -\frac{e}{2}\left(u \cdot \frac{\partial E_0}{\partial z} - v \cdot kE_0\right) \qquad \text{Eq. (A3.8)}$$

Expand u, v using Eq. (A3.6), and replace the electric field E with the light intensity I using $I = \frac{1}{2}\epsilon_0 c E_0^2$, where c is the light speed in vacuum and ϵ_0 is vacuum permittivity. Eq. (A3.8) becomes:

$$< F_z >= \frac{e^2}{2\epsilon_0 m\omega}(-\frac{\delta}{\delta^2 + \frac{\beta^2}{4}} \cdot \frac{1}{\omega} \cdot \frac{\partial I}{\partial z} + \frac{\beta/2}{\delta^2 + \frac{\beta^2}{4}} \cdot \frac{k}{\omega} \cdot I) \qquad \text{Eq. (A3.9)}$$

By adding $< F_x >, < F_y >$ which follow a similar form with Eq. (A3.9), we obtain the vector form of the force:

$$< \vec{F} > = \frac{e^2}{2\epsilon_0 m\omega}\left(-\frac{\delta}{\delta^2+\frac{\beta^2}{4}}\cdot\frac{1}{\omega}\cdot\nabla I+\frac{\frac{\beta}{2}}{\delta^2+\frac{\beta^2}{4}}\cdot\frac{\vec{k}}{\omega}\cdot I\right)$$

$$= < \vec{F}_{dipole} > + < \vec{F}_{scatt.} >,$$

Eq. (A3.10)

where the dipole force $< \vec{F}_{dipole} >$ is along the intensity gradient ∇I, and points to darker (or brighter) field if the frequency detuning δ is positive (or negative); and the scattering force $< \vec{F}_{scatt} >$ points along the light-propagation direction $\vec{k}$. Note that the momentum $(\hbar\vec{k})$ can be transferred from photons to the atom through scattering force.

The results using classical mechanics [Eq. (A3.6)~Eq. (A3.10)] can only be used for qualitative analysis of the radiation force dependence on the light frequency [75], with the precise solution given by quantum mechanics, where u, v are Bloch vectors, and the displacement physical property x needs to be replaced with the corresponding operator on probability waves $X_{12} =< 1|x|2 >$. Therefore, Eq. (A3.8) becomes

$$F_z = -\frac{eX_{12}}{2}\left(u\cdot\frac{\partial E_0}{\partial z} - v\cdot kE_0\right) = F_{dipole} + F_{scatt.}$$

Eq. (A3.11)

Note that the dipole force comes from the in-phase component of the dipole (u) and the scattering force comes from the quadrature component of the dipole (v). Based on Eq. 7.68 of ref.[75], the corrected form of Eq. (A3.6) is

$$\binom{u}{v} = \frac{1}{\delta^2+\frac{\Omega^2}{2}+\frac{\Gamma^2}{4}}\binom{\Omega\delta}{\frac{1}{2}\Omega\Gamma},$$

Eq. (A3.12)

where $\Omega = eX_{12}E_0/\hbar$ is the Rabi frequency. Substitute u, v into Eq. (A3.11), we obtain the corrected form of Eq. (A3.10):

$$F_{dipole} = -\frac{\hbar\delta}{2}\frac{\Omega}{\delta^2 + \frac{\Omega^2}{2} + \frac{\Gamma^2}{4}}\frac{\partial\Omega}{\partial z},$$

$$F_{scatt.} = \hbar k\frac{\Gamma}{2}\frac{\Omega^2/2}{\delta^2+\frac{\Omega^2}{2}+\frac{\Gamma^2}{4}} = \hbar k\frac{\Gamma}{2}\frac{I/I_{sat}}{1+I/I_{sat}+\frac{\delta^2}{4\Gamma^2}},$$

Eq. (A3.13)

where the saturation intensity I_{sat} is defined by $\frac{I}{I_{sat}} = \frac{2\Omega^2}{\Gamma^2}$ {Eq. (7.86) of [75].

We further discuss the dipole force in Eq. (A3.13) under two circumstances:

1. At the resonant frequency ($\delta = 0$), $F_{dipole} = 0$
2. At large detuned frequency ($|\delta| \gg \Gamma$) with an intensity that $|\delta| \gg \Omega$:

$$F_{dipole} \cong = -\frac{\hbar}{2}\frac{\Omega}{\delta}\frac{\partial\Omega}{\partial z} = -\frac{\partial}{\partial z}\left(\frac{\hbar\Omega^2}{4\delta}\right) = -\frac{\partial}{\partial z}(\hbar\omega_{a.c.Stark}),$$

Eq. (A3.14)

where $\omega_{a.c.Stark} = \Omega^2/4\delta$ is the energy level shift of an atom in an oscillating electric field {Eq. (7.93) of [75]. By adding the component in x, y, the vector form of the dipole force becomes

$$\vec{F}_{dipoe} = -\nabla(\hbar\omega_{a.c.Stark}),$$

Eq. (A3.15)

which indicates the dipole force is a conservative force since it can be written as the negative gradient of a potential energy:

$$U_{dipole} = \hbar\omega_{a.c.Stark}$$

Eq. (A3.16)

Thus, the a.c. Stark shift for an atom in the ground state acts as a potential energy which the atom moves to minimize. Based on $\frac{I}{I_{sat}} = \frac{2\Omega^2}{\Gamma^2}$ {Eq. (7.86) of [75]}, the dipole potential can also be written as:

$$U_{dipole} = \frac{\hbar\Omega^2}{4\delta} = \frac{\hbar\Gamma^2}{8} \cdot \frac{1}{\delta} \cdot \frac{I}{I_{sat}}$$ Eq. (A3.17)

For largely red detuned light ($\delta < 0$), $U_{dipole} < 0$, the interaction between light and the atom is attractive, and the atom is pulled to brighter region; for largely blue detuned light ($\delta > 0$), $U_{dipole} > 0$, the interaction between light and the atom is repulsive, and the atom is pushed towards darker region.

References

[1] J. L. O'Brien, G. J. Pryde, A. G. White, T. C. Ralph, and D. Branning, "Demonstration of an all-optical quantum controlled-NOT gate," *Nature*, vol. 426, no. 6964, Art. no. 6964, Nov. 2003, doi: 10.1038/nature02054.

[2] L.-M. Duan, M. D. Lukin, J. I. Cirac, and P. Zoller, "Long-distance quantum communication with atomic ensembles and linear optics," *Nature*, vol. 414, no. 6862, Art. no. 6862, Nov. 2001, doi: 10.1038/35106500.

[3] S. Pirandola, B. R. Bardhan, T. Gehring, C. Weedbrook, and S. Lloyd, "Advances in photonic quantum sensing," *Nature Photon*, vol. 12, no. 12, Art. no. 12, Dec. 2018, doi: 10.1038/s41566-018-0301-6.

[4] E. Urban *et al.*, "Observation of Rydberg blockade between two atoms," *Nature Phys*, vol. 5, no. 2, Art. no. 2, Feb. 2009, doi: 10.1038/nphys1178.

[5] T. F. Watson *et al.*, "A programmable two-qubit quantum processor in silicon," *Nature*, vol. 555, no. 7698, Art. no. 7698, Mar. 2018, doi: 10.1038/nature25766.

[6] J. A. Rushton, M. Aldous, and M. D. Himsworth, "Contributed Review: The feasibility of a fully miniaturized magneto-optical trap for portable ultracold quantum technology," *Review of Scientific Instruments*, vol. 85, no. 12, p. 121501, Dec. 2014, doi: 10.1063/1.4904066.

[7] L. Isenhower, W. Williams, A. Dally, and M. Saffman, "Atom trapping in an interferometrically generated bottle beam trap," *Opt. Lett.*, vol. 34, no. 8, p. 1159, Apr. 2009, doi: 10.1364/OL.34.001159.

[8] G. F. Quinteiro and T. Kuhn, "Light-hole transitions in quantum dots: Realizing full control by highly focused optical-vortex beams," *Phys. Rev. B*, vol. 90, no. 11, p. 115401, Sep. 2014, doi: 10.1103/PhysRevB.90.115401.

[9] N. Yu *et al.*, "Light Propagation with Phase Discontinuities: Generalized Laws of Reflection and Refraction," *Science*, vol. 334, no. 6054, pp. 333–337, Oct. 2011, doi: 10.1126/science.1210713.

[10] N. Yu and F. Capasso, "Flat optics with designer metasurfaces," *Nature Mater*, vol. 13, no. 2, Art. no. 2, Feb. 2014, doi: 10.1038/nmat3839.

[11] Q. Wang *et al.*, “A Broadband Metasurface-Based Terahertz Flat-Lens Array,” *Advanced Optical Materials*, vol. 3, no. 6, pp. 779–785, 2015, doi: 10.1002/adom.201400557.

[12] N. Yu, F. Aieta, P. Genevet, M. A. Kats, Z. Gaburro, and F. Capasso, “A Broadband, Background-Free Quarter-Wave Plate Based on Plasmonic Metasurfaces,” *Nano Lett.*, vol. 12, no. 12, pp. 6328–6333, Dec. 2012, doi: 10.1021/nl303445u.

[13] N. Li *et al.*, “Large-area metasurface on CMOS-compatible fabrication platform: driving flat optics from lab to fab,” *Nanophotonics*, vol. 9, no. 10, pp. 3071–3087, Sep. 2020, doi: 10.1515/nanoph-2020-0063.

[14] Z. Yu *et al.*, “Optical components based on multi-refractive-index metamaterials,” *J. Phys. D: Appl. Phys.*, vol. 53, no. 1, p. 015108, Oct. 2019, doi: 10.1088/1361-6463/ab4843.

[15] A. Poddubny, I. Iorsh, P. Belov, and Y. Kivshar, “Hyperbolic metamaterials,” *Nature Photonics*, vol. 7, no. 12, pp. 958–967, 2013, doi: 10.1038/nphoton.2013.243.

[16] J. Valentine *et al.*, “Three-dimensional optical metamaterial with a negative refractive index,” *Nature*, vol. 455, no. 7211, pp. 376–379, 2008, doi: 10.1038/nature07247.

[17] N. I. Landy, S. Sajuyigbe, J. J. Mock, D. R. Smith, and W. J. Padilla, “Perfect metamaterial absorber,” *Physical Review Letters*, vol. 100, no. 20, p. 207402, 2008, doi: 10.1103/PhysRevLett.100.207402.

[18] S. M. Rytov, “Electromagnetic properties of a finely stratified medium,” *Soviet Physics JETP*, vol. 2, no. 3, pp. 446–475, 1956.

[19] A. A. Orlov, P. M. Voroshilov, P. A. Belov, and Y. S. Kivshar, “Engineered optical nonlocality in nanostructured metamaterials,” *Physical Review B - Condensed Matter and Materials Physics*, vol. 84, no. 4, pp. 1–4, 2011, doi: 10.1103/PhysRevB.84.045424.

[20] A. Cabuz, D. Felbacq, and D. Cassagne, “Spatial dispersion in negative-index composite metamaterials,” no. January, pp. 1–11, 2008, doi: 10.1103/PhysRevA.77.013807.

[21] A. V. Chebykin, A. A. Orlov, A. V. Vozianova, S. I. Maslovski, Yu. S. Kivshar, and P. A. Belov, “Nonlocal effective medium model for multilayered metal-dielectric metamaterials,” *Physical Review B*, vol. 84, no. 11, pp. 1–9, 2011, doi: 10.1103/PhysRevB.84.115438.

[22] A. F. Mota, A. Martins, J. Weiner, F. L. Teixeira, and B. V Borges, “Constitutive parameter retrieval for uniaxial metamaterials with spatial dispersion,” vol. 115410, pp. 1–9, 2016, doi: 10.1103/PhysRevB.94.115410.

[23] A. A. Orlov, A. K. Krylova, S. V. Zhukovsky, V. E. Babicheva, and P. A. Belov, “Multiperiodicity in plasmonic multilayers: General description and diversity of topologies,” *Physical Review A*, vol. 90, no. 1, p. 013812, 2014, doi: 10.1103/PhysRevA.90.013812.

[24] D. Woolf, M. Loncar, and F. Capasso, “The forces from coupled surface plasmon polaritons in planar waveguides,” *Optics Express*, vol. 17, no. 22, p. 19996, 2009, doi: 10.1364/OE.17.019996.

[25] J. A. Dionne, L. A. Sweatlock, H. A. Atwater, and A. Polman, “Plasmon slot waveguides: Towards chip-scale propagation with subwavelength-scale localization,” *Physical Review B*, vol. 73, no. 3, p. 035407, 2006, doi: 10.1103/PhysRevB.73.035407.

[26] E. D. Palik, “Handbook of Optical Constants of Solids.” 1997.

[27] E. Hecht, *Optics, Global Edition*. Pearson Education Limited, 2016.

[28] Y. Li, “Focal shifts in diffracted converging spherical waves,” *Optics Communications*, vol. 41, no. 3, pp. 145–148, 1982, doi: 10.1016/0030-4018(82)90059-1.

[29] A. Yariv, “Coupled-Mode theory for guided-wave optics,” *IEEE Journal of Quantum Electronics*, vol. 9, no. 9, pp. 919–933, 1973, doi: 10.1109/JQE.1973.1077767.

[30] J. B. Khurgin, “How to deal with the loss in plasmonics and metamaterials,” *Nature Nanotechnology*, vol. 10, no. 1, pp. 2–6, 2015, doi: 10.1038/nnano.2014.310.

[31] R. Waele, S. P. Burgos, A. Polman, and H. A. Atwater, “Plasmon dispersion in coaxial waveguides from single-cavity optical transmission measurements,” *Nano Letters*, vol. 9, no. 8, pp. 2832–2837, 2009, doi: 10.1021/nl900597z.

[32] B. Rizal, J. M. Merlo, M. J. Burns, T. C. Chiles, and M. J. Naughton, “Nanocoaxes for optical and electronic devices,” *The Analyst*, vol. 140, no. 1, pp. 39–58, 2015, doi: 10.1039/c4an01447b.

[33] Z. Yu, G. Hickman, M. Saffman, M. A. Kats, M. A. Kats, and M. A. Kats, “Diffractive chips for magneto-optical trapping of two atomic species,” in *Conference on Lasers and Electro-Optics (2020), paper STh4G.7*, May 2020, p. STh4G.7. doi: 10.1364/CLEO_SI.2020.STh4G.7.

[34] Z. Yu, “Diffractive chips for magneto-optical trapping of two atomic species.” https://www.spiedigitallibrary.org/conference-proceedings-of-spie/11471/114710O/Diffractive-chips-for-magneto-optical-trapping-of-two-atomic-species/10.1117/12.2570647.full?SSO=1 (accessed Jul. 27, 2022).

[35] G. Hickman *et al.*, “A fully-integrated single-photon source based on single Rb atoms,” *50th Annual Meeting of the APS Division of Atomic, Molecular and Optical Physics APS Meeting*, May 2019, Accessed: Aug. 31, 2022. [Online]. Available: https://par.nsf.gov/biblio/10097631-fully-integrated-single-photon-source-based-single-rb-atoms

[36] S. Deshpande *et al.*, “Multiphysics Modeling of Grating Chips for Magneto-Optical Trapping of Atoms,” in *Conference on Lasers and Electro-Optics (2022), paper JTu3A.8*, May 2022, p. JTu3A.8. Accessed: Aug. 16, 2022. [Online]. Available: https://opg.optica.org/abstract.cfm?uri=CLEO_AT-2022-JTu3A.8

[37] J. Zhang, “An optical chip for a single atom single photon source,” in *Bulletin of the American Physical Society*, Jun. 2021, vol. Volume 66, Number 6. Accessed: Jul. 27, 2022. [Online]. Available: https://meetings.aps.org/Meeting/DAMOP21/Session/V01.68

[38] T. Bothwell *et al.*, “Resolving the gravitational redshift across a millimetre-scale atomic sample,” *Nature*, vol. 602, no. 7897, Art. no. 7897, Feb. 2022, doi: 10.1038/s41586-021-04349-7.

[39] “Observation of Bose-Einstein Condensation in a Dilute Atomic Vapor | Science.” https://www.science.org/doi/abs/10.1126/science.269.5221.198 (accessed Sep. 16, 2022).

[40] R. Brierley, Y. Li, and L. Benini, “Ultracold quantum technologies,” *Nat. Phys.*, vol. 17, no. 12, Art. no. 12, Dec. 2021, doi: 10.1038/s41567-021-01461-3.

[41] T. M. Graham *et al.*, “Multi-qubit entanglement and algorithms on a neutral-atom quantum computer,” *Nature*, vol. 604, no. 7906, Art. no. 7906, Apr. 2022, doi: 10.1038/s41586-022-04603-6.

[42] H. P. Specht *et al.*, “A single-atom quantum memory,” *Nature*, vol. 473, no. 7346, Art. no. 7346, May 2011, doi: 10.1038/nature09997.

[43] D. Schrader, I. Dotsenko, M. Khudaverdyan, Y. Miroshnychenko, A. Rauschenbeutel, and D. Meschede, “Neutral Atom Quantum Register,” *Phys. Rev. Lett.*, vol. 93, no. 15, p. 150501, Oct. 2004, doi: 10.1103/PhysRevLett.93.150501.

[44] F. Schäfer, T. Fukuhara, S. Sugawa, Y. Takasu, and Y. Takahashi, “Tools for quantum simulation with ultracold atoms in optical lattices,” *Nat Rev Phys*, vol. 2, no. 8, Art. no. 8, Aug. 2020, doi: 10.1038/s42254-020-0195-3.

[45] I. Buluta and F. Nori, "Quantum Simulators," *Science*, vol. 326, no. 5949, pp. 108–111, Oct. 2009, doi: 10.1126/science.1177838.
[46] K. Bongs *et al.*, "Taking atom interferometric quantum sensors from the laboratory to real-world applications," *Nat Rev Phys*, vol. 1, no. 12, Art. no. 12, Dec. 2019, doi: 10.1038/s42254-019-0117-4.
[47] B. B. Blinov, D. L. Moehring, L.-M. Duan, and C. Monroe, "Observation of entanglement between a single trapped atom and a single photon," *Nature*, vol. 428, no. 6979, Art. no. 6979, Mar. 2004, doi: 10.1038/nature02377.
[48] M. Karski *et al.*, "Quantum Walk in Position Space with Single Optically Trapped Atoms," *Science*, vol. 325, no. 5937, pp. 174–177, Jul. 2009, doi: 10.1126/science.1174436.
[49] E. L. Raab, M. Prentiss, A. Cable, S. Chu, and D. E. Pritchard, "Trapping of Neutral Sodium Atoms with Radiation Pressure," *Phys. Rev. Lett.*, vol. 59, no. 23, pp. 2631–2634, Dec. 1987, doi: 10.1103/PhysRevLett.59.2631.
[50] J. J. McClelland, A. V. Steele, B. Knuffman, K. A. Twedt, A. Schwarzkopf, and T. M. Wilson, "Bright focused ion beam sources based on laser-cooled atoms," *Applied Physics Reviews*, vol. 3, no. 1, p. 011302, Mar. 2016, doi: 10.1063/1.4944491.
[51] K. I. Lee, J. A. Kim, H. R. Noh, and W. Jhe, "Single-beam atom trap in a pyramidal and conical hollow mirror," *Opt. Lett., OL*, vol. 21, no. 15, pp. 1177–1179, Aug. 1996, doi: 10.1364/OL.21.001177.
[52] M. L. Harris, P. Tierney, and S. L. Cornish, "Magnetic trapping of a cold Rb–Cs atomic mixture," *J. Phys. B: At. Mol. Opt. Phys.*, vol. 41, no. 3, p. 035303, Jan. 2008, doi: 10.1088/0953-4075/41/3/035303.
[53] J. J. Arlt, O. Maragò, S. Webster, S. Hopkins, and C. J. Foot, "A pyramidal magneto-optical trap as a source of slow atoms," *Optics Communications*, vol. 157, no. 1, pp. 303–309, Dec. 1998, doi: 10.1016/S0030-4018(98)00499-4.
[54] W. Bowden *et al.*, "A pyramid MOT with integrated optical cavities as a cold atom platform for an optical lattice clock," *Sci Rep*, vol. 9, no. 1, Art. no. 1, Aug. 2019, doi: 10.1038/s41598-019-48168-3.
[55] M. Vangeleyn, P. F. Griffin, E. Riis, and A. S. Arnold, "Laser cooling with a single laser beam and a planar diffractor," *Opt. Lett.*, vol. 35, no. 20, p. 3453, Oct. 2010, doi: 10.1364/OL.35.003453.
[56] C. C. Nshii *et al.*, "A surface-patterned chip as a strong source of ultracold atoms for quantum technologies," *Nature Nanotech*, vol. 8, no. 5, pp. 321–324, May 2013, doi: 10.1038/nnano.2013.47.
[57] J. P. McGilligan, P. F. Griffin, E. Riis, and A. S. Arnold, "Diffraction-grating characterization for cold-atom experiments," *J. Opt. Soc. Am. B, JOSAB*, vol. 33, no. 6, pp. 1271–1277, Jun. 2016, doi: 10.1364/JOSAB.33.001271.
[58] E. Imhof, B. K. Stuhl, B. Kasch, B. Kroese, S. E. Olson, and M. B. Squires, "Two-dimensional grating magneto-optical trap," *Phys. Rev. A*, vol. 96, no. 3, p. 033636, Sep. 2017, doi: 10.1103/PhysRevA.96.033636.
[59] D. S. Barker, E. B. Norrgard, N. N. Klimov, J. A. Fedchak, J. Scherschligt, and S. Eckel, "Single-Beam Zeeman Slower and Magneto-Optical Trap Using a Nanofabricated Grating," *Phys. Rev. Applied*, vol. 11, no. 6, p. 064023, Jun. 2019, doi: 10.1103/PhysRevApplied.11.064023.

[60] S. Bondza, C. Lisdat, S. Kroker, and T. Leopold, “Two-Color Grating Magneto-Optical Trap for Narrow-Line Laser Cooling,” *Phys. Rev. Applied*, vol. 17, no. 4, p. 044002, Apr. 2022, doi: 10.1103/PhysRevApplied.17.044002.

[61] M. Mudrich, S. Kraft, K. Singer, R. Grimm, A. Mosk, and M. Weidemüller, “Sympathetic Cooling with Two Atomic Species in an Optical Trap,” *Phys. Rev. Lett.*, vol. 88, no. 25, p. 253001, Jun. 2002, doi: 10.1103/PhysRevLett.88.253001.

[62] G. Modugno, M. Modugno, F. Riboli, G. Roati, and M. Inguscio, “Two Atomic Species Superfluid,” *Phys. Rev. Lett.*, vol. 89, no. 19, p. 190404, Oct. 2002, doi: 10.1103/PhysRevLett.89.190404.

[63] G. Roati, F. Riboli, G. Modugno, and M. Inguscio, “Fermi-Bose Quantum Degenerate $^{\mathrm{40}}\mathrm{K}\mathrm{\text{\ensuremath{-}}}^{\mathrm{87}}\mathrm{R}\mathrm{b}$ Mixture with Attractive Interaction,” *Phys. Rev. Lett.*, vol. 89, no. 15, p. 150403, Sep. 2002, doi: 10.1103/PhysRevLett.89.150403.

[64] Z. Hadzibabic *et al.*, “Two-Species Mixture of Quantum Degenerate Bose and Fermi Gases,” *Phys. Rev. Lett.*, vol. 88, no. 16, p. 160401, Apr. 2002, doi: 10.1103/PhysRevLett.88.160401.

[65] R. Geiger and M. Trupke, “Proposal for a Quantum Test of the Weak Equivalence Principle with Entangled Atomic Species,” *Phys. Rev. Lett.*, vol. 120, no. 4, p. 043602, Jan. 2018, doi: 10.1103/PhysRevLett.120.043602.

[66] P. Asenbaum, C. Overstreet, M. Kim, J. Curti, and M. A. Kasevich, “Atom-Interferometric Test of the Equivalence Principle at the ${10}^{\ensuremath{-}12}$ Level,” *Phys. Rev. Lett.*, vol. 125, no. 19, p. 191101, Nov. 2020, doi: 10.1103/PhysRevLett.125.191101.

[67] I. I. Beterov and M. Saffman, “Rydberg blockade, F\"orster resonances, and quantum state measurements with different atomic species,” *Phys. Rev. A*, vol. 92, no. 4, p. 042710, Oct. 2015, doi: 10.1103/PhysRevA.92.042710.

[68] D. A. Steck, “Rubidium 87 D Line Data.” 2001. [Online]. Available: https://steck.us/alkalidata/rubidium87numbers.1.6.pdf

[69] V. Gerginov, C. E. Tanner, S. Diddams, A. Bartels, and L. Hollberg, “Optical frequency measurements of $6s\phantom{\rule{0.2em}{0ex}}^{2}S_{1⁄2}--6p\phantom{\rule{0.2em}{0ex}}^{2}P_{3⁄2}$ transition in a $^{133}\mathrm{Cs}$ atomic beam using a femtosecond laser frequency comb,” *Phys. Rev. A*, vol. 70, no. 4, p. 042505, Oct. 2004, doi: 10.1103/PhysRevA.70.042505.

[70] A. A. Darweesh, S. J. Bauman, D. T. Debu, and J. B. Herzog, “The Role of Rayleigh-Wood Anomalies and Surface Plasmons in Optical Enhancement for Nano-Gratings,” *Nanomaterials*, vol. 8, no. 10, Art. no. 10, Oct. 2018, doi: 10.3390/nano8100809.

[71] A. Sommer, “Alloys of Gold with Alkali Metals,” *Nature*, vol. 152, no. 3851, pp. 215–215, Aug. 1943, doi: 10.1038/152215a0.

[72] “Grating projections in FDTD overview,” *Ansys Optics*. https://optics.ansys.com/hc/en-us/articles/360034394354-Grating-projections-in-FDTD-overview (accessed Sep. 15, 2022).

[73] S. Pollock, J. P. Cotter, A. Laliotis, F. Ramirez-Martinez, and E. A. Hinds, “Characteristics of integrated magneto-optical traps for atom chips,” *New J. Phys.*, vol. 13, no. 4, p. 043029, Apr. 2011, doi: 10.1088/1367-2630/13/4/043029.

[74] L. Huet, M. Ammar, E. Morvan, and N. Sarazin, “Magneto-Optical Trapping and Detection of Atoms Through a Transparent Atom Chip,” p. 3, 2011.

[75] C. J. Foot, *Atomic Physics*. OUP Oxford, 2004.

[76] Y. Xiao *et al.*, “Efficient generation of optical bottle beams,” *Nanophotonics*, vol. 10, no. 11, pp. 2893–2901, Sep. 2021, doi: 10.1515/nanoph-2021-0243.

[77] R. Dumke, M. Volk, T. Müther, F. B. J. Buchkremer, G. Birkl, and W. Ertmer, “Micro-optical Realization of Arrays of Selectively Addressable Dipole Traps: A Scalable Configuration for Quantum Computation with Atomic Qubits,” *Phys. Rev. Lett.*, vol. 89, no. 9, p. 097903, Aug. 2002, doi: 10.1103/PhysRevLett.89.097903.

[78] Y.-J. Lin, A. R. Perry, R. L. Compton, I. B. Spielman, and J. V. Porto, “Rapid production of $^{87}\text{R}\text{b}$ Bose-Einstein condensates in a combined magnetic and optical potential,” *Phys. Rev. A*, vol. 79, no. 6, p. 063631, Jun. 2009, doi: 10.1103/PhysRevA.79.063631.

[79] B. T. Wolschrijn, R. A. Cornelussen, R. J. C. Spreeuw, and H. B. van L. van den Heuvell, “Guiding of cold atoms by a red-detuned laser beam of moderate power,” *New J. Phys.*, vol. 4, pp. 69–69, 2002, doi: 10.1088/1367-2630/4/1/369.

[80] N. Davidson, H. Jin Lee, C. S. Adams, M. Kasevich, and S. Chu, “Long Atomic Coherence Times in an Optical Dipole Trap,” *Phys. Rev. Lett.*, vol. 74, no. 8, pp. 1311–1314, Feb. 1995, doi: 10.1103/PhysRevLett.74.1311.

[81] G. Li, S. Zhang, L. Isenhower, K. Maller, and M. Saffman, “Crossed vortex bottle beam trap for single-atom qubits,” *Opt. Lett., OL*, vol. 37, no. 5, pp. 851–853, Mar. 2012, doi: 10.1364/OL.37.000851.

[82] J. Arlt and M. J. Padgett, “Generation of a beam with a dark focus surrounded by regions of higher intensity: the optical bottle beam,” *Opt. Lett., OL*, vol. 25, no. 4, pp. 191–193, Feb. 2000, doi: 10.1364/OL.25.000191.

[83] P. Xu, X. He, J. Wang, and M. Zhan, “Trapping a single atom in a blue detuned optical bottle beam trap,” *Opt. Lett., OL*, vol. 35, no. 13, pp. 2164–2166, Jul. 2010, doi: 10.1364/OL.35.002164.

[84] D. Barredo *et al.*, “Three-Dimensional Trapping of Individual Rydberg Atoms in Ponderomotive Bottle Beam Traps,” *Phys. Rev. Lett.*, vol. 124, no. 2, p. 023201, Jan. 2020, doi: 10.1103/PhysRevLett.124.023201.

[85] V. Pavelyev *et al.*, “Diffractive optical elements for the formation of ‘light bottle’ intensity distributions,” *Appl. Opt., AO*, vol. 51, no. 18, pp. 4215–4218, Jun. 2012, doi: 10.1364/AO.51.004215.

[86] H. Yu *et al.*, “Chip-scale molecule trapping by a blue-detuned metasurface hollow beam,” *J. Opt.*, vol. 22, no. 4, p. 045104, Mar. 2020, doi: 10.1088/2040-8986/ab7aea.

[87] G. Hickman, “A fully-integrated single-photon source based on single Rb atoms,” in *Bulletin of the American Physical Society*, May 2019, vol. Volume 64, Number 4. Accessed: Jul. 27, 2022. [Online]. Available: https://meetings.aps.org/Meeting/DAMOP19/Session/S01.86

[88] J. W. Goodman, *Introduction to Fourier Optics*. Roberts and Company Publishers, 2005.

[89] M. A. Bandres *et al.*, “Accelerating Optical Beams,” *Optics & Photonics News, OPN*, vol. 24, no. 6, pp. 30–37, Jun. 2013, doi: 10.1364/OPN.24.6.000030.

[90] P. Zhang *et al.*, “Generation of acoustic self-bending and bottle beams by phase engineering,” *Nat Commun*, vol. 5, no. 1, Art. no. 1, Jul. 2014, doi: 10.1038/ncomms5316.

[91] D.-C. Chen, X.-F. Zhu, Q. Wei, D.-J. Wu, and X.-J. Liu, “Dynamic generation and modulation of acoustic bottle-beams by metasurfaces,” *Sci Rep*, vol. 8, no. 1, Art. no. 1, Aug. 2018, doi: 10.1038/s41598-018-31066-5.

[92] M. Decker *et al.*, “High-Efficiency Dielectric Huygens’ Surfaces,” *Advanced Optical Materials*, vol. 3, no. 6, pp. 813–820, 2015, doi: 10.1002/adom.201400584.

[93] Y. F. Yu, A. Y. Zhu, R. Paniagua-Domínguez, Y. H. Fu, B. Luk’yanchuk, and A. I. Kuznetsov, “High-transmission dielectric metasurface with 2π phase control at visible

wavelengths," *Laser & Photonics Reviews*, vol. 9, no. 4, pp. 412–418, 2015, doi: 10.1002/lpor.201500041.
[94] S. M. Kamali, E. Arbabi, A. Arbabi, and A. Faraon, "A review of dielectric optical metasurfaces for wavefront control," *Nanophotonics*, vol. 7, no. 6, pp. 1041–1068, Jun. 2018, doi: 10.1515/nanoph-2017-0129.
[95] D. Sell, J. Yang, S. Doshay, K. Zhang, and J. A. Fan, "Visible Light Metasurfaces Based on Single-Crystal Silicon," *ACS Photonics*, vol. 3, no. 10, pp. 1919–1925, Oct. 2016, doi: 10.1021/acsphotonics.6b00436.
[96] Z. Zhou *et al.*, "Efficient Silicon Metasurfaces for Visible Light," *ACS Photonics*, vol. 4, no. 3, pp. 544–551, Mar. 2017, doi: 10.1021/acsphotonics.6b00740.
[97] M. I. Shalaev, J. Sun, A. Tsukernik, A. Pandey, K. Nikolskiy, and N. M. Litchinitser, "High-Efficiency All-Dielectric Metasurfaces for Ultracompact Beam Manipulation in Transmission Mode," *Nano Lett.*, vol. 15, no. 9, pp. 6261–6266, Sep. 2015, doi: 10.1021/acs.nanolett.5b02926.
[98] W. Zhu *et al.*, "Titanium dioxide metasurface manipulating high-efficiency and broadband photonic spin Hall effect in visible regime," *Nanophotonics*, vol. 9, no. 14, pp. 4327–4335, Oct. 2020, doi: 10.1515/nanoph-2020-0290.
[99] N. K. Emani *et al.*, "High-efficiency and low-loss gallium nitride dielectric metasurfaces for nanophotonics at visible wavelengths," *Appl. Phys. Lett.*, vol. 111, no. 22, p. 221101, Nov. 2017, doi: 10.1063/1.5007007.
[100] B. H. Chen *et al.*, "GaN Metalens for Pixel-Level Full-Color Routing at Visible Light," *Nano Lett.*, vol. 17, no. 10, pp. 6345–6352, Oct. 2017, doi: 10.1021/acs.nanolett.7b03135.
[101] J.-H. Yang, V. E. Babicheva, M.-W. Yu, T.-C. Lu, T.-R. Lin, and K.-P. Chen, "Structural Colors Enabled by Lattice Resonance on Silicon Nitride Metasurfaces," *ACS Nano*, vol. 14, no. 5, pp. 5678–5685, May 2020, doi: 10.1021/acsnano.0c00185.
[102] S. Colburn *et al.*, "Broadband transparent and CMOS-compatible flat optics with silicon nitride metasurfaces [Invited]," *Opt. Mater. Express, OME*, vol. 8, no. 8, pp. 2330–2344, Aug. 2018, doi: 10.1364/OME.8.002330.
[103] H. Yang *et al.*, "Transfer-printed stacked nanomembrane lasers on silicon," *Nature Photon*, vol. 6, no. 9, Art. no. 9, Sep. 2012, doi: 10.1038/nphoton.2012.160.
[104] C.-W. Cheng, K.-T. Shiu, N. Li, S.-J. Han, L. Shi, and D. K. Sadana, "Epitaxial lift-off process for gallium arsenide substrate reuse and flexible electronics," *Nat Commun*, vol. 4, no. 1, Art. no. 1, Mar. 2013, doi: 10.1038/ncomms2583.
[105] H. G. Tompkins and J. N. Hilfiker, *Spectroscopic Ellipsometry: Practical Application to Thin Film Characterization*. Momentum Press, 2015.
[106] R. A. Wambold *et al.*, "Adjoint-optimized nanoscale light extractor for nitrogen-vacancy centers in diamond," *Nanophotonics*, vol. 10, no. 1, pp. 393–401, Jan. 2021, doi: 10.1515/nanoph-2020-0387.
[107] Z. Huang *et al.*, "Diamond nitrogen-vacancy centers created by scanning focused helium ion beam and annealing," *Appl. Phys. Lett.*, vol. 103, no. 8, p. 081906, Aug. 2013, doi: 10.1063/1.4819339.
[108] S. B. van Dam *et al.*, "Optical coherence of diamond nitrogen-vacancy centers formed by ion implantation and annealing," *Phys. Rev. B*, vol. 99, no. 16, p. 161203, Apr. 2019, doi: 10.1103/PhysRevB.99.161203.
[109] J. R. Rabeau *et al.*, "Implantation of labelled single nitrogen vacancy centers in diamond using N15," *Appl. Phys. Lett.*, vol. 88, no. 2, p. 023113, Jan. 2006, doi: 10.1063/1.2158700.

[110] S. Ishii, S. Saiki, S. Onoda, Y. Masuyama, H. Abe, and T. Ohshima, “Ensemble Negatively-Charged Nitrogen-Vacancy Centers in Type-Ib Diamond Created by High Fluence Electron Beam Irradiation,” *Quantum Beam Science*, vol. 6, no. 1, Art. no. 1, Mar. 2022, doi: 10.3390/qubs6010002.

[111] M. W. Doherty, N. B. Manson, P. Delaney, F. Jelezko, J. Wrachtrup, and L. C. L. Hollenberg, “The nitrogen-vacancy colour centre in diamond,” *Physics Reports*, vol. 528, no. 1, pp. 1–45, Jul. 2013, doi: 10.1016/j.physrep.2013.02.001.

[112] R. Schirhagl, K. Chang, M. Loretz, and C. L. Degen, “Nitrogen-Vacancy Centers in Diamond: Nanoscale Sensors for Physics and Biology,” *Annu. Rev. Phys. Chem.*, vol. 65, no. 1, pp. 83–105, Apr. 2014, doi: 10.1146/annurev-physchem-040513-103659.

[113] M. S. J. Barson, E. Krausz, N. B. Manson, and M. W. Doherty, “The fine structure of the neutral nitrogen-vacancy center in diamond,” *Nanophotonics*, vol. 8, no. 11, pp. 1985–1991, Nov. 2019, doi: 10.1515/nanoph-2019-0142.

[114] Y. Doi *et al.*, “Deterministic Electrical Charge-State Initialization of Single Nitrogen-Vacancy Center in Diamond,” *Phys. Rev. X*, vol. 4, no. 1, p. 011057, Mar. 2014, doi: 10.1103/PhysRevX.4.011057.

[115] B. Grotz *et al.*, “Charge state manipulation of qubits in diamond,” *Nat Commun*, vol. 3, no. 1, Art. no. 1, Mar. 2012, doi: 10.1038/ncomms1729.

[116] K.-M. C. Fu, C. Santori, P. E. Barclay, and R. G. Beausoleil, “Conversion of neutral nitrogen-vacancy centers to negatively charged nitrogen-vacancy centers through selective oxidation,” *Appl. Phys. Lett.*, vol. 96, no. 12, p. 121907, Mar. 2010, doi: 10.1063/1.3364135.

[117] L. Rondin *et al.*, “Surface-induced charge state conversion of nitrogen-vacancy defects in nanodiamonds,” *Phys. Rev. B*, vol. 82, no. 11, p. 115449, Sep. 2010, doi: 10.1103/PhysRevB.82.115449.

[118] M. V. Hauf *et al.*, “Chemical control of the charge state of nitrogen-vacancy centers in diamond,” *Phys. Rev. B*, vol. 83, no. 8, p. 081304, Feb. 2011, doi: 10.1103/PhysRevB.83.081304.

[119] L. Childress and R. Hanson, “Diamond NV centers for quantum computing and quantum networks,” *MRS Bulletin*, vol. 38, no. 2, pp. 134–138, Feb. 2013, doi: 10.1557/mrs.2013.20.

[120] A. Russo, E. Barnes, and S. E. Economou, “Photonic graph state generation from quantum dots and color centers for quantum communications,” *Phys. Rev. B*, vol. 98, no. 8, p. 085303, Aug. 2018, doi: 10.1103/PhysRevB.98.085303.

[121] M. V. G. Dutt *et al.*, “Quantum Register Based on Individual Electronic and Nuclear Spin Qubits in Diamond,” *Science*, vol. 316, no. 5829, pp. 1312–1316, Jun. 2007, doi: 10.1126/science.1139831.

[122] G. Balasubramanian *et al.*, “Nanoscale imaging magnetometry with diamond spins under ambient conditions,” *Nature*, vol. 455, no. 7213, Art. no. 7213, Oct. 2008, doi: 10.1038/nature07278.

[123] J. R. Maze *et al.*, “Nanoscale magnetic sensing with an individual electronic spin in diamond,” *Nature*, vol. 455, no. 7213, Art. no. 7213, Oct. 2008, doi: 10.1038/nature07279.

[124] F. Dolde *et al.*, “Electric-field sensing using single diamond spins,” *Nature Phys*, vol. 7, no. 6, Art. no. 6, Jun. 2011, doi: 10.1038/nphys1969.

[125] J. Wang *et al.*, “High-sensitivity temperature sensing using an implanted single nitrogen-vacancy center array in diamond,” *Phys. Rev. B*, vol. 91, no. 15, p. 155404, Apr. 2015, doi: 10.1103/PhysRevB.91.155404.

[126] G. Kucsko *et al.*, “Nanometre-scale thermometry in a living cell,” *Nature*, vol. 500, no. 7460, Art. no. 7460, Aug. 2013, doi: 10.1038/nature12373.

[127] T. Zhang *et al.*, “Toward Quantitative Bio-sensing with Nitrogen–Vacancy Center in Diamond,” *ACS Sens.*, vol. 6, no. 6, pp. 2077–2107, Jun. 2021, doi: 10.1021/acssensors.1c00415.

[128] J. Barton *et al.*, “Nanoscale Dynamic Readout of a Chemical Redox Process Using Radicals Coupled with Nitrogen-Vacancy Centers in Nanodiamonds,” *ACS Nano*, vol. 14, no. 10, pp. 12938–12950, Oct. 2020, doi: 10.1021/acsnano.0c04010.

[129] B. F. Bachman *et al.*, “High-Density Covalent Grafting of Spin-Active Molecular Moieties to Diamond Surfaces,” *Langmuir*, vol. 37, no. 30, pp. 9222–9231, Aug. 2021, doi: 10.1021/acs.langmuir.1c01425.

[130] T.-Y. Huang *et al.*, “A monolithic immersion metalens for imaging solid-state quantum emitters,” *Nat Commun*, vol. 10, no. 1, Art. no. 1, Jun. 2019, doi: 10.1038/s41467-019-10238-5.

[131] N. H. Wan *et al.*, “Efficient Extraction of Light from a Nitrogen-Vacancy Center in a Diamond Parabolic Reflector,” *Nano Lett.*, vol. 18, no. 5, pp. 2787–2793, May 2018, doi: 10.1021/acs.nanolett.7b04684.

[132] J. T. Choy *et al.*, “Enhanced single-photon emission from a diamond–silver aperture,” *Nature Photon*, vol. 5, no. 12, pp. 738–743, Dec. 2011, doi: 10.1038/nphoton.2011.249.

[133] L. Li *et al.*, “Efficient Photon Collection from a Nitrogen Vacancy Center in a Circular Bullseye Grating,” *Nano Lett.*, vol. 15, no. 3, pp. 1493–1497, Mar. 2015, doi: 10.1021/nl503451j.

[134] M. Y. Shalaginov *et al.*, “Enhancement of single-photon emission from nitrogen-vacancy centers with TiN/(Al,Sc)N hyperbolic metamaterial,” *Laser & Photonics Reviews*, vol. 9, no. 1, pp. 120–127, 2015, doi: 10.1002/lpor.201400185.

[135] R. Albrecht, A. Bommer, C. Deutsch, J. Reichel, and C. Becher, “Coupling of a Single Nitrogen-Vacancy Center in Diamond to a Fiber-Based Microcavity,” *Phys. Rev. Lett.*, vol. 110, no. 24, p. 243602, Jun. 2013, doi: 10.1103/PhysRevLett.110.243602.

[136] J. s. Jensen and O. Sigmund, “Topology optimization for nano-photonics,” *Laser & Photonics Reviews*, vol. 5, no. 2, pp. 308–321, 2011, doi: 10.1002/lpor.201000014.

[137] D. Sell, J. Yang, S. Doshay, R. Yang, and J. A. Fan, “Large-Angle, Multifunctional Metagratings Based on Freeform Multimode Geometries,” *Nano Lett.*, vol. 17, no. 6, pp. 3752–3757, Jun. 2017, doi: 10.1021/acs.nanolett.7b01082.

[138] C. M. Lalau-Keraly, S. Bhargava, O. D. Miller, and E. Yablonovitch, “Adjoint shape optimization applied to electromagnetic design,” *Opt. Express, OE*, vol. 21, no. 18, pp. 21693–21701, Sep. 2013, doi: 10.1364/OE.21.021693.

[139] M. Zahedian, J. Liu, R. Vidrio, S. Kolkowitz, and J. T. Choy, “Depth dependence of the radiative lifetime of shallow color centers in single crystalline diamond.” arXiv, Jul. 14, 2022. doi: 10.48550/arXiv.2207.07217.

[140] R. J. Epstein, F. M. Mendoza, Y. K. Kato, and D. D. Awschalom, “Anisotropic interactions of a single spin and dark-spin spectroscopy in diamond,” *Nature Phys*, vol. 1, no. 2, Art. no. 2, Nov. 2005, doi: 10.1038/nphys141.

[141] P. R. Dolan, X. Li, J. Storteboom, and M. Gu, “Complete determination of the orientation of NV centers with radially polarized beams,” *Opt. Express, OE*, vol. 22, no. 4, pp. 4379–4387, Feb. 2014, doi: 10.1364/OE.22.004379.

[142] O. Sigmund, “Manufacturing tolerant topology optimization,” *Acta Mech Sin*, vol. 25, no. 2, pp. 227–239, Apr. 2009, doi: 10.1007/s10409-009-0240-z.

[143] E. W. Wang, D. Sell, T. Phan, and J. A. Fan, “Robust design of topology-optimized metasurfaces,” *Opt. Mater. Express, OME*, vol. 9, no. 2, pp. 469–482, Feb. 2019, doi: 10.1364/OME.9.000469.

[144] A. Y. Piggott, J. Lu, K. G. Lagoudakis, J. Petykiewicz, T. M. Babinec, and J. Vučković, “Inverse design and demonstration of a compact and broadband on-chip wavelength demultiplexer,” *Nature Photon*, vol. 9, no. 6, Art. no. 6, Jun. 2015, doi: 10.1038/nphoton.2015.69.

[145] J. Lu and J. Vučković, “Nanophotonic computational design,” *Opt. Express, OE*, vol. 21, no. 11, pp. 13351–13367, Jun. 2013, doi: 10.1364/OE.21.013351.

[146] P. Goy, J. M. Raimond, M. Gross, and S. Haroche, “Observation of Cavity-Enhanced Single-Atom Spontaneous Emission,” *Phys. Rev. Lett.*, vol. 50, no. 24, pp. 1903–1906, Jun. 1983, doi: 10.1103/PhysRevLett.50.1903.

[147] S. Sharma, V. Kumar, P. Rawat, J. Ghosh, and V. Venkataraman, “Nanowaveguide Designs in 220-nm SOI for Ultra-Broadband FWM at Telecom Wavelengths,” *IEEE Journal of Quantum Electronics*, vol. 56, no. 5, pp. 1–8, Oct. 2020, doi: 10.1109/JQE.2020.3004863.

[148] J. Zhang *et al.*, “All-silicon multi-band TM-pass polarizer on a 220 nm SOI enabled by multiplexing grating regimes,” *Opt. Express, OE*, vol. 30, no. 1, pp. 326–335, Jan. 2022, doi: 10.1364/OE.447435.

[149] D. Benedikovic *et al.*, “Subwavelength index engineered surface grating coupler with sub-decibel efficiency for 220-nm silicon-on-insulator waveguides,” *Opt. Express, OE*, vol. 23, no. 17, pp. 22628–22635, Aug. 2015, doi: 10.1364/OE.23.022628.

[150] M. Streshinsky *et al.*, “A compact bi-wavelength polarization splitting grating coupler fabricated in a 220 nm SOI platform,” *Opt. Express, OE*, vol. 21, no. 25, pp. 31019–31028, Dec. 2013, doi: 10.1364/OE.21.031019.

[151] M.-L. Hicks, A. C. Pakpour-Tabrizi, and R. B. Jackman, “Diamond Etching Beyond 10 µm with Near-Zero Micromasking,” *Sci Rep*, vol. 9, no. 1, Art. no. 1, Oct. 2019, doi: 10.1038/s41598-019-51970-8.

[152] K. Racka-Szmidt, B. Stonio, J. Żelazko, M. Filipiak, and M. Sochacki, “A Review: Inductively Coupled Plasma Reactive Ion Etching of Silicon Carbide,” *Materials*, vol. 15, no. 1, Art. no. 1, Jan. 2022, doi: 10.3390/ma15010123.

[153] S. Yasin, D. G. Hasko, and H. Ahmed, “Fabrication of <5 nm width lines in poly(methylmethacrylate) resist using a water:isopropyl alcohol developer and ultrasonically-assisted development,” *Appl. Phys. Lett.*, vol. 78, no. 18, pp. 2760–2762, Apr. 2001, doi: 10.1063/1.1369615.

[154] S. Yasin, D. G. Hasko, and H. Ahmed, “Comparison of MIBK/IPA and water/IPA as PMMA developers for electron beam nanolithography,” *Microelectronic Engineering*, vol. 61–62, pp. 745–753, Jul. 2002, doi: 10.1016/S0167-9317(02)00468-9.

[155] N. Arjmandi, L. Lagae, and G. Borghs, “Enhanced resolution of poly(methyl methacrylate) electron resist by thermal processing,” *Journal of Vacuum Science & Technology B: Microelectronics and Nanometer Structures Processing, Measurement, and Phenomena*, vol. 27, no. 4, pp. 1915–1918, Jul. 2009, doi: 10.1116/1.3167367.